Universität Stuttgart

The Influence of Flow Shear on Drift-Wave Interactions in the Stellarator TJ-K

Von der Fakultät Energie-, Verfahrens- und Biotechnik der Universität Stuttgart zur Erlangung der Würde eines Doktors der Naturwissenschaften (Dr. rer. nat.) genehmigte Abhandlung

vorgelegt von
Til Ullmann
aus Würzburg

Hauptberichter:	Prof. Dr. Günter Tovar
1. Mitberichter:	Prof. Dr. Peter Manz
Prüfungsvorsitzender:	Prof. Dr. Carsten Mehring
Tag der mündlichen Prüfung:	27.07.2021

Institut für Grenzflächenverfahrenstechnik und Plasmatechnologie
2021

“... TILT ...” - Til

Contents

Summary

The investigation of the interaction between shear flows and turbulence in magnetically confined fusion plasmas is motivated by the fact that shear flows can lead to a reduction or even suppression of the turbulent transport to the vessel wall. Thus they can significantly improve the performance of future nuclear fusion power plants. Therefore, in this thesis the influence of stationary background shear and time-dependent zonal flows on the wave interactions was investigated. The turbulence-generated zonal flows not only have the character of a shear flow, but in turn extract energy from the turbulence, while they themselves do not contribute to the transport of particles to the outside.

Due to this special property, the dependence of this energy transfer on the background shearing rate was investigated experimentally. Because of its low-temperature plasmas, the stellarator experiment TJ-K offers the possibility of measuring the dynamics even within the confinement area by invasive diagnostics, such as Langmuir probes. This way, the tilting of turbulent eddy structures could be related to the background shear. The Reynolds stress, as a measure for the tilting, is linearly dependent on the shearing rate. Since the energy transfer between zonal flows and turbulence is composed of the product of the Reynolds stress and the background shear, a quadratic dependence of the energy transfer on the shearing rate was expected and here experimentally confirmed. In addition, the energy transfer between turbulence and zonal flows also led to a redistribution of the spectral power in favor of the zonal flows from $\approx 5\%$ up to $\approx 40\%$ of the total power for increasing shearing rate.

In the picture of drift-wave turbulence, the non-linearity of the dynamics is reflected in three-wave interaction. The drift waves follow resonance conditions in the wavenumber and frequency space, which in turn are linked by the dispersion relation so that not all couplings are allowed. This defined coupling space is also called the resonant manifold. Theoretical considerations by Gürcan assumed that shear flows cause the coupling space of the nonlinear three-wave interaction to contract. Experimentally, this behavior could now be demonstrated on the basis of the shear-character of time-dependent zonal flows using the method of time-resolved wavenumber-frequency bicoherence. Here, it was shown that the effective coupling space actually shrinks with the occurrence of the shear flow and expands again with the decay of the zonal flow.

The results in this thesis show that $E \times B$ background shear flows, as

they occur during the transition from low to highly confined fusion plasmas, can trigger turbulence-driven zonal flows, whose Reynolds stress drive was initiated by a mean tilt of the vortex structure. At the same time, shear flows can restrict the coupling space of drift waves and thus increase the importance of large-scale structures, in particular e.g. zonal flows that do not contribute to turbulent transport, as possible energy sinks. If the shear flows are zonal flows themselves, self-amplification can become effective.

Kurzfassung

Ausschlaggebend für die Untersuchung der Wechselwirkung zwischen Scherströmungen und Turbulenz in magnetisch eingeschlossenen Fusionsplasmen war, dass Scherströmungen zu einer Reduktion bis hin zur Unterdrückung des turbulenten Transports zur Gefäßwand führen können und somit die Leistungsfähigkeit zukünftiger Kernfusionskraftwerke maßgeblich verbessern können. In dieser Arbeit wurden deswegen die Einflüsse stationärer Hintergrundscherströmungen und zeitabhängiger Zonalströmungen auf die Wechselwirkung der Driftwellen untersucht. Die Turbulenz-generierten Zonalströmungen besitzen nicht nur den Charakter einer Scherströmung, sondern entziehen außerdem der Turbulenz Energie, während sie selbst keinen Beitrag zum Teilchentransport nach außen leisten.

Aufgrund dieser besonderen Eigenschaft wurde die Abhängigkeit des Energietransfers von der Hintergrundscherströmung experimentell untersucht. Das Experiment, der Stellarator TJ-K, bietet aufgrund seiner niedrig-Temperatur Plasmen die Möglichkeit durch invasive Diagnostiken, wie Langmuirsonden, die Dynamik auch innerhalb des Einschlussbereichs zu vermessen. Die Verkippung turbulenter Wirbelstrukturen konnte mit der Hintergrundverscherung in Beziehung gesetzt werden. Der Reynolds-Spannungstensor, als Maß für die Verkippung, hängt dabei linear von der Scherrate ab. Da sich der Energietransfer zwischen Zonalströmungen und Turbulenz aus dem Produkt der Reynolds-Spannung und der Hintergrundscherung zusammensetzt, wurde eine quadratische Abhängigkeit des Energietransfers von der Scherrate erwartet und auch hier experimentell bestätigt. Weiterhin wurde gezeigt, dass der Energietransfer zwischen Turbulenz und Zonalströmungen zudem zu einer Umverteilung der spektralen Leistung von $\approx 5\%$ bis $\approx 40\%$ zugunsten der Zonalströmungen führt bei steigender Scherrate.

Im Bild der Turbulenz als Driftwelleninstabilitäten spiegelt die Nicht-Linearität der Dynamik von Dreiwellenwechselwirkungen wider. Die Driftwellen folgen dabei Resonanzbedingungen im Wellenzahl- und Frequenzraum, die wiederum durch die Dispersionsrelation miteinander verknüpft sind, sodass nicht alle Kopplungen erlaubt sind. Dieser definierte Kopplungsraum wird auch als resonante Mannigfaltigkeit bezeichnet. Theoretische Überlegungen durch Gürcan gingen davon aus, dass Scherströmungen den Kopplungsraum der nichtlinearen Dreiwellenwelchselwirkung zusammenziehen lassen. Experimentell konnte dieses Verhalten anhand des Scher-Charakters der zeitabhängigen Zonalströmungen mit Hilfe der Methode einer zeitaufgelösten Wellenzahl-Frequenz-Bikohärenz nun nachgewiesen werden. Es zeigte sich, dass tatsäch-

lich der effektive Kopplungsraum sich mit dem Aufkommen der Scherströmung zusammenzieht und mit dem Abklingen der Zonalströmung wieder ausdehnt.

Die Ergebnisse in dieser Arbeit zeigen, dass $E \times B$ - Hintergrundscherströmungen, wie sie auch beim Übergang von niedrigen zu hocheingeschlossenen Fusionsplasmen auftreten, Turbulenz-getriebene Zonalströmungen auslösen können, deren Reynolds-Spannungs-Antrieb durch eine mittlere Verkippung der Wirbelstruktur initiiert wurde. Gleichzeitig können Scherströmungen den Kopplungsraum von Driftwellen einschränken und somit den relativen Kopplungsanteil groß-skaliger Strukturen, insbesondere z.B. Zonalströmungen, die nicht zum turbulenten Transport beitragen, als mögliche Energiesenken erhöhen. Sind die Scherströmungen selbst Zonalströmungen können sie sich so selbst verstärken.

Chapter 1

Introduction

An IEA[1]/OECD[2] forecast for the year 2040 assumes that global energy consumption will increase by a quarter [1]. At the same time, due to the climate crisis, attempts are being made to phase out more and more fossil fuels [2, 3, 4]. For a given infrastructure renewable energies can replace fossil-fueled power plants, but require a closed meshing and real-time managed power grid [5] as well as large areas [6]. A total conversion of the energy supply to renewable energies may not be possible in all countries for economic and political reasons and raises the question of how to manage the base-load in the power grid. One possibility to satisfy both developments is to make usable the high amount of energy released by nuclear fusion for civil and economic purposes [7].

In such a reactor the energy released by the fusion of deuterium and tritium to helium and fast neutrons will be converted into usable electric energy. Hereby, the probability that two positively charged atomic nuclei will overcome the repulsive Coulomb force due to their high velocity or due to the quantum mechanical tunnel effect is raised by a high density, a high temperature and a high confinement time [8, 9]. In order to confine such an ultra-hot plasma, which exceeds the temperature of the sun's interior by many times [10], the plasma is confined in a magnetic cage. In magnetically confined plasmas turbulence leads to a significant reduction of the confinement time. Thus, the efficiency of a future power plant is lowered [11]. However, an operation mode has already been found in which turbulence is reduced or even suppressed and the plasma is highly confined (H-mode) [12, 13]. Hereby, the H-mode is found in both major toroidal confinement concepts, the tokamak [14] and the stellarator [15, 16, 17]. Even if the origin of this H-mode is not yet fully understood, it is assumed that strong shear flows are responsible for the turbulence reduction [18]. Although turbulence generated

[1] International Energy Agency
[2] Organisation for Economic Co-operation and Development

shear flows such as zonal flows (ZF) can trigger a spontaneous transition to the H-mode [19, 20, 21, 22, 23, 24, 25, 26], it was found that ZFs do not contribute significantly to the background flow in slow transitions as in the intermediate phase (I-phase) [27]. Therefore two general questions crystallize: First, how does the background shear flow influence turbulence? And second, how does the background shear change the relevance of ZFs as a loss channel or as a distributor of energy?

Both questions give the motivational framework for this thesis, namely the investigation of the influence of shear flows on plasma turbulence in the stellarator experiment TJ-K. This stellarator is operated at low temperatures, which makes it possible studying plasma dynamics with invasive diagnostics in more detail than it is possible in a high-temperature fusion experiment [28]. This opportunity makes TJ-K a wind tunnel experiment for plasma turbulence, since the dynamics scale to those in fusion experiments according to dimensionless parameters [29]. The influence of two main types of shear flows is investigated: the impact of stationary background shear flows and of time-varying, turbulence-generated zonal flows. The plasma turbulence occurring in the edge of magnetically confined fusion plasmas and in the stellarator TJ-K can be described in two pictures, in the picture of fluid turbulence and in the picture of wave turbulence which both exhibit nonlinear interaction terms. In both pictures the shear changes the radial propagation of turbulent structures, i.e. their radial wavenumber, which is mathematically described in the so-called shearing coordinates.

In the fluid picture, the background shear flows can tilt turbulent eddies. This tilt can be quantified by the so-called Reynolds stress. Theoretical approaches, including the shearing coordinates, suggest a linear dependency between the shearing rate and the Reynolds stress [30]. The Reynolds stress not only describes the tilting of turbulent vortex structures, but is also part of the non-linear energy transfer term between turbulence and mean flow. The mean flow in this context includes ZFs, as the mean flow is determined by a zonal average. The energy-transfer term or so-called production term - as it “produces” the mean flow - is composed of the Reynolds Stress term and, again, the shearing rate. To summarize these relations the first working hypotheses are formed and experimentally confirmed:

- The tilt of turbulent structures can be quantified by the Reynolds stress. The background shear tilts turbulent vortex structures, which results in a linear dependency between shearing rate and Reynolds stress.
- The linear dependency between Reynolds stress and shearing rate

results in a quadratic dependency between the energy-transfer, i.e. the production term, and the shearing rate.

- As the energy transfer from the turbulence into the ZF rises with the background shearing rate, the spectral power is redistributed such that the power in the ZF rises compared to other modes, i.e. the relative ZF-power rises.

In fluid turbulence the initial instability is not important. After a short growth phase of the initial instability, the nonlinear dynamics takes over. The ratio of nonlinearity to viscous dissipation mainly determines the dynamics. The turbulence in magnetically confined fusion plasma is usually not that strong. The fluctuations are not occurring only as vortices but also propagating as waves. The driving instability leaves dynamic finger-prints. One important wave for plasma turbulence is the drift wave.

In the picture of wave turbulence, the nonlinear, "turbulent" behavior is described by three-wave interaction [31, 32, 33]. Hereby drift-waves can only couple if the three-wave resonance conditions, resolved in wavenumber-frequency space, are satisfied. The dispersion relation describing the wavenumber dependency of the frequency further restricts the set of possible couplings which is referred to as the resonant manifold [34]. This set of possible couplings is reduced under flow shear as theoretically proposed by Gürcan [35]. His theoretical approach is investigated at the stellarator TJ-K and summarized in the working hypothesis

- Under the constraints of the resonance conditions in wavenumber frequency space and the dispersion relation, the zonal flow as time-dependent shear initially reduces the set of possible couplings and leads to a contraction of the resonant manifold.

In order to test the before-mentioned working hypotheses, this work is structured as follows: First, an introduction to the geometry of toroidally confined plasmas (sec. 2.1) and, linked to this, an overview of basic drift velocities is given (sec. 2.2). After short heuristic explanations of turbulence in general (sec. 2.3), as well as stationary shear flows and time-dependent zonal flows (sec. 2.4), the shear coordinates important for the following theoretical considerations are introduced (sec. 2.5). Subsequently, the energy transfer between zonal flows and turbulence, and the hypotheses resulting from the Reynolds averaged Navier-Stokes equations are derived in more detail (sec. 2.6). The drift wave dynamics will be described in the next chapter (sec. 2.7), focusing on the derivation of the three-wave interaction,

as well as investigating the influence of the shear flow on the coupling space of the waves. In the experiment description (sec. 3) an overview of important diagnostics is given and an illustration of how shear flows can be generated by plasma biasing. After a brief description of the analysis methods (sec. 4), in the first experimental part, the background profiles of the plasma parameters are discussed with respect to their possible role in zonal flow amplification (sec. 5). Then the calculation of the shearing rates and their comparison with the growth rates are demonstrated. In the next chapter, the comparison of three different tilt angles with each other and with the Reynolds stress shows that the shearing rate does indeed contribute to a tilt of turbulent vortex structures (sec. 6). Afterwards, the energy transfer between turbulence and zonal flows is discussed. It is found that an increase in shearing rate is accompanied by an increase in power in the zonal flows relative to the power in the turbulence (sec. 7). This chapter essentially follows the publication of [36]. The last chapter (sec. 8) deals with the three-wave interaction in the image of drift waves. It is shown that the main contributions in the kf-bicoherence follow the dispersion relation of drift waves. The influence of time-dependent shear flows is treated. Sec. 8.2 follows the publication of [37] where it can be shown that the expansion of the effective coupling space correlates with the occurrence and decay of zonal flows.

Chapter 2

Theoretical aspects of sheared plasma turbulence

As a basis for the experimental investigations and results of this work, the theoretical aspects of the influence of shear flows on turbulence at the edge of magnetically confined plasmas are introduced in this chapter. The main hypotheses of this work are derived from fundamental physical models like the Navier-Stokes equation and the drift-wave model. First, however, basic concepts and termini of the geometry of toroidally confined plasmas are explained (sec. 2.1). In the second section, the plasma drifts being fundamental for the dynamics within a magnetized plasma are explained (sec. 2.2). After a heuristic introduction to turbulence in general (sec. 2.3), the different types of shear flows are discussed (sec. 2.4) and how to model them in terms of shear coordinates is shown in sec. 2.5. Finally, the influence of shear flows is discussed, first in the picture of fluids (sec. 2.6), then in the picture of drift waves (sec. 2.7), and the main hypotheses are derived on the basis of these two models.

2.1 Geometry

In magnetically confined fusion a toroidally geometry has prevailed. Therefore it is necessary to briefly discuss different coordinate systems and expressions. The coordinate system of a torus is shown in fig. 2.1. The angle θ is the so-called *poloidal* angle, whereas φ is the angle in the *toroidal* direction. The *radial* coordinate r is associated with the small radius of the torus, whereas the major radius R_0 is constant. The field lines of the magnetic field twist in such a way that they form surfaces that are nested radially. Inside such a surface the magnetic flux is constant and therefore is called flux-surface. The idealized scheme is a toroidal shell as indicated by the grid in fig. 2.1. The outermost is the last closed flux surface (LCFS). On a flux-surface, the equilibrium parameters as the density n_e, the temperature T_e, T_i, the

pressure p_e, as well as the plasma potential ϕ_{pl} can be considered constant in a first-order approximation, too. Please note that in a more complex type of magnetic confinement, such as the stellarator, the magnetic cage is not aligned to the torus coordinates and the system has to be adjusted [38].

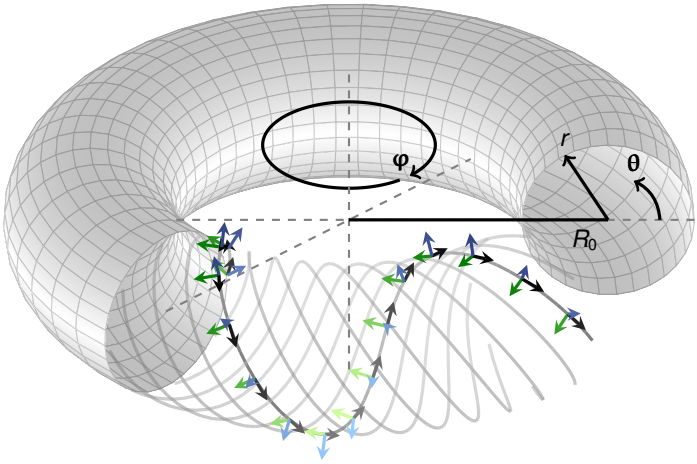

Figure 2.1: Scheme of the torus geometry. Here R_0 is called the major radius, r the radius, θ the poloidal angle, φ the toroidal angle. The blue arrow indicates the normal, the green the geodesic and the black arrow the parallel coordinate in reference to the magnetic field line.

The twisted magnetic field lines, as indicated as grey lines in fig. 2.1, generate the magnetic flux surfaces. The twist of the magnetic field line can be described by its slope in the poloidal and toroidal plane which is referred to the rotational transform ι for stellarators and its inverse, the safety factor, $q = \iota^{-1}$ for tokamaks. Turbulent structures are supposed to follow the twisted magnetic field line in a first approximation and the coordinate system is adjusted to the magnetic cage. The new system is defined by a component normal to the flux surface (blue vectors), a component perpendicular to the normal vector, called the geodesic vector (green), and the magnetic field line direction by the component parallel to the magnetic field line (black vectors).

Since the dynamics parallel to the magnetic field does not lead to any transport, the turbulence responsible for the transport can be considered as two-dimensional, most of the theoretical approaches are done in the

simplified geometry of a slab spanned by x, y-coordinates referring to the plane perpendicular to the magnetic field. Furthermore, the system can also be regarded as an approximation to sufficiently small sections of the magnetic coordinate system.

2.2 Plasma drifts

In a magnetically confined plasma, there are different types of drifts that influence the dynamics within the plasma and a brief overview of these is given in this section (c.f. [39, 40] (eng.) and [41](ger)).

In a homogeneous magnetic field ($\boldsymbol{B}$), the individual charged particles are gyrating due to the Lorentz force. The center of the gyration is called the guiding center and the movement of the guiding center is called drift. Every force acting on the charged particle causes a drift of the guiding center perpendicular to the force and the magnetic field. The drift that is repeatedly referred to in this work is the so-called $E\times B$-drift, which results from the electric Coulomb force

$$\boldsymbol{u}_{E\times B} = \frac{\boldsymbol{E}\times\boldsymbol{B}}{B^2} \ , \tag{2.1}$$

with $\boldsymbol{E}$ as the electric Field. If there are no fluctuations in the magnetic field, the turbulence is called electrostatic turbulence and its dynamics is determined by the fluctuations in the potential. In addition to the $E\times B$-drift, time-varying electric fields cause another drift, which is called polarization drift

$$\boldsymbol{u}_{\mathrm{pol}} = \frac{m}{qB^2}\dot{\boldsymbol{E}}_{\perp} \tag{2.2}$$

depending on the mass m and the charge q. Further, the pressure gradient in the magnetically confined plasma leads to the so-called diamagnetic drift

$$\boldsymbol{u}_{\mathrm{dia}} = -\frac{\boldsymbol{\nabla} p\times\boldsymbol{B}}{qn_eB^2} \ , \tag{2.3}$$

with n_e the plasma density. Since it results from the macroscopic concept of pressure, it exists only in the view of plasma as a fluid. Two other drifts that exist only in the picture of single particles are the gradient (∇B) and

curvature ($\boldsymbol{\kappa}$) drifts, which can be summarized as

$$\boldsymbol{v}_{\nabla B,\kappa} = \left(2W_{\parallel} + W_{\perp}\right) \frac{\boldsymbol{\kappa} \times \boldsymbol{B}}{q\kappa^2 B^2} \ , \tag{2.4}$$

with the parallel $W_{\parallel}$ and the perpendicular $W_{\perp}$ kinetic energy of the particles. The curvature of the magnetic field can lead to destabilization of the waves (cf. sec. 2.7.4). For reasons of completeness, it should be noted that the $E \times B$-drift and the polarisation drift appear in both, the fluid and the particle, picture.

2.3 Turbulence characteristics in magnetized plasmas

A short, heuristic introduction into important properties of turbulence is given in this section. Detailed literature can be found in [42, 30]. In order to illustrate turbulence, a laminar flow from the left to the right is shown in fig. 2.2-*left*. Depending on its velocity (v), density (ρ) or viscosity (μ), the

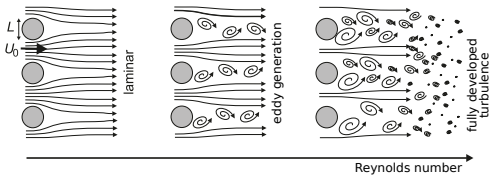

Figure 2.2: Development of turbulence in a neutral fluid caused by obstacles [41].

laminar fluid can develop eddy structures behind obstacles (fig. 2.2-*middle*) that can be classified by the Reynolds number $R_{\mathrm{Re}} \propto \rho v \mu^{-1}$. If the parameters change towards higher Reynolds numbers, the laminar flow changes into a fully developed turbulent state interspersed with eddies (fig. 2.2-*right*). Due to the turbulence, energy is distributed over super-positioned structures of different sizes (s) quantified by the wavenumber $k = s^{-1}$. A typical power distribution for a three dimensional turbulent system is shown in fig. 2.3-*left*. This power spectrum reveals three regions: energy is injected at low wavenumbers, i.e. large turbulent structures (injection region), then transferred to small structures (inertial region) and finally dissipated into heat (dissipation region). The energy is transferred in the so-called direct cascade from small to large wavenumbers. The energy density follows the power law $k^{-5/3}$ in the inertial region as the so-called Kolmogorow (K-41)

theory [43] proposes.

In contrast, energy is transferred from small to large scale structures in the two-dimensional case fig. 2.3-*right* [44]. Here, only two regions are identified, the dual cascade. Due to enstrophy ($0.5(\nabla \times u)^2$) conservation energy follows a k^{-3} power law. Enstrophy is transferred to smaller scales. This transfer is accompanied by an up-scale energy transfer generating large-scale structures. The up-scale energy transfer follows a $k^{-5/3}$ power law.

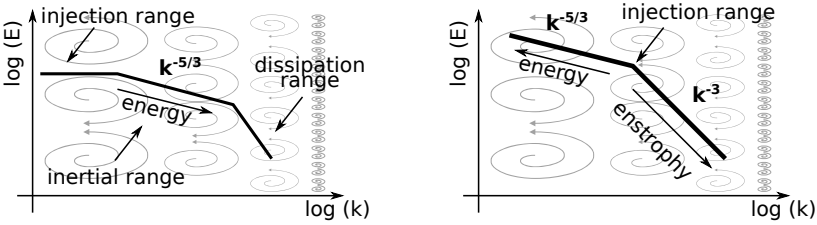

Figure 2.3: Turbulent power laws for the three- *(left)* and two-dimensional *(right)* system. Whereas in the 3D case the turbulence is transferred towards smaller eddy structures [43], in the 2D case the energy is transferred to larger scales [44] (adapted from [11]).

In the context of magnetic confined plasmas, the two-dimensional case, the dual cascade is confirmed for dynamics in drift-wave turbulence [45, 46]. Hence, kinetic energy is transferred from small to large structures. This effect may be enhanced in the presence of a shear flow where turbulent eddies are strained out in the direction of the shear flow [47].

2.4 Background $E\times B$ shear and zonal flows

This work mainly investigates the effect of flow shear on the turbulent fluctuations. In the context of magnetically confined fusion plasmas, it is useful to differentiate between two types of shear, namely the background shear and the so-called zonal flow shear. Both are determined by inhomogeneities in the radial profile of the electric field resulting in a radially changing velocity profile, i.e. in a shear. Further both types show a poloidal and toroidal symmetry. Nevertheless, both originate from different phenomena having consequences on their time-dependence. Thus, the background shear depends on the equilibrium, time-independent potential, a result of the ambipolarity of particle fluxes.

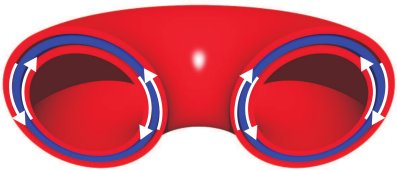

Figure 2.4: Scheme of a zonal flow. Tube-like potential perturbations (blue) result in counter-rotating $E\times B$-flows (white), which can be interpreted as time-dependent shear flows [56].

In contrast, zonal flows (ZF) are time-dependent, low-frequency shear flows, which can be deduced from tube-like potential perturbations, i.e. $k_\theta = k_\varphi = 0$ and $k_r \neq 0$ [48, 49], as schematically shown in fig. 2.4. ZFs are turbulence-generated [50, 51, 32], in the frame of a self-organized process, which will be discussed in sec. 2.6.2. This cycle can be understood as limit cycle oszillations [48, 52] similar to predator-prey dynamics in biology [53]. As ZFs are poloidally symmetric potential perturbations, they are associated with a radial electric field and correspondingly with poloidal velocity fluctuations. They do not contribute to radial transport but limit it as experimentally found in [54]. This unique property has brought zonal flows into focus in the context of transport reduction at the L-H transition. The role of the ZF in the L-H transition is controversial. Whereas ZFs are found to trigger the H-mode [19, 20, 21, 22, 23, 24, 25, 26], it is further found that ZFs do not have a large contribution to the mean-flow in the I-phase [27]. ZFs are subject to damping mechanisms. Those processes can be for example collisional damping or energy transfer into geodesic acoustic modes [48, 49]. The latter are oszillating pressure perturbations caused by the different $E\times B$-velocities of the ZF on the sides of the low- and high-magnetic field. This difference results in accumulation of particles and therefore in a shift of the isobars to the top of a cross-section leading to a $m = 1$ density perturbation in a circular Tokamak [55].The arising diamagnetic currents act against the $E\times B$-drifts and lead to an oszillation of the perturbation.

2.5 Shearing coordinates

A method to include the shear in models of turbulent systems is introducing shearing coordinates. In consequence, there is an effective change of the radial wavenumber fundamental to turbulence in neutral fluids (sec. 2.6)

and the model of drift-wave turbulence (sec. 2.7). In electrostatic plasma turbulence the dynamics is only determined by plasma potential fluctuations. The potential fluctuations can be expressed by a Fourier decomposition, which is chosen for the two-dimensional case as

$$\begin{aligned}\tilde{\phi} &= \phi_0 \exp\left[i\psi\right] = \phi_0 \exp\left[i\left(\boldsymbol{kr} - \omega t\right)\right] \\ &= \phi_0 \exp\left[i\left(k_x x + k_y y - \omega t\right)\right] \ . \end{aligned} \tag{2.5}$$

Here, ω is the angular frequency and ψ the phase. The wave-vector $\boldsymbol{\nabla}\psi = \boldsymbol{k} = (k_x, k_y)$ describes the propagation of the wave-fronts of the superimposed waves with k_x as the radial wavenumber and k_y as the poloidal wavenumber. The electric shear is defined as the radial derivative of the time-independent $E\times B$-velocity and is called the background shear

$$V'_E = \partial_x v_{y,E\times B} = \partial_x \frac{\partial y}{\partial t} \ . \tag{2.6}$$

The consequences of a spatial gradient in the background velocity (V') is

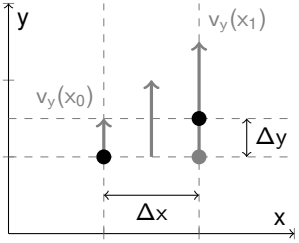

Figure 2.5: Scheme of the poloidal displacement of turbulent structures due to the background shear. The change in the background flow velocity leads to a tilt of a fluid element, indicated as black ellipse, compared to the case without a sheared flow (gray ellipse).

illustrated in fig. 2.5. A gradient in x-direction (gray arrows) leads to a poloidal shift (Δy) in the flow-direction of two radially separated elements (fig. 2.5 circles) within a structure (fig. 2.5 ellipse). The structure experiences a tilt (black ellipse) in contrast to the case without a radially changing velocity field (gray ellipse).

The tilt of the structures implies a change of the wave-fronts in the picture of superimposed waves. The radial wavenumber k_x has to be recalculated

from the gradient of the phase ($k_x = \partial_x \psi$). The change in the velocity is implemented in the phase equation, where the angular frequency consists of the product of the wavevector ($\boldsymbol{k}$) and the phase velocity ($\boldsymbol{v}$)

$$\omega = \boldsymbol{k}\boldsymbol{v} = k_x v_{0,x} + k_y v_{0,y} + k_y V_E' \Delta x \quad . \tag{2.7}$$

Here, the velocity vector is $\delta \boldsymbol{v} = (v_{0,x}, v_{0,y} + V_E' \delta x)$. Therefore the modified radial wavenumber from the gradient of the phase ($\boldsymbol{k'} = \boldsymbol{\nabla} \psi$) is

$$k_x' = \partial_x \psi = \partial_x \left(k_x x\right) - k_y V_E' t \partial_x (\delta x) = k_x - k_y V_E' t \ . \tag{2.8}$$

Eq. 2.8 defines a new radial wavenumber, which can result in strong changes of the dynamics for drift-waves (sec. 2.7.3). The potential is the analogon to the negative stream function in the frame of neutral fluid flows. Hence, the shearing coordinates are later implemented for velocity fluctuations in neutral fluids (sec. 2.6.2.2) in the same way as for the drift-waves.

2.6 Reynolds averaged Navier-Stokes equation

The dynamics of an incompressible fluid at a constant density can be described by the Navier-Stokes equation

$$\frac{\partial \boldsymbol{v}}{\partial t} + (\boldsymbol{v} \cdot \boldsymbol{\nabla} \boldsymbol{v}) = -\boldsymbol{\nabla} p + \mu \Delta \boldsymbol{v} = -\boldsymbol{\nabla} p \tag{2.9}$$

where $\boldsymbol{v}$ is the velocity, μ the dynamic viscosity and p the pressure divided by the density. For simplicity, the viscosity is neglected in the following ($\mu = 0$). In this limits, the Navier-Stokes equation is called the Euler equation. The velocity can be split in a fluctuating part $\tilde{\boldsymbol{u}}$ and in a mean flow $\boldsymbol{U}$

$$\boldsymbol{v} = \tilde{\boldsymbol{u}} + \boldsymbol{U} \tag{2.10}$$

$$= \tilde{\boldsymbol{u}} + \langle \boldsymbol{v} \rangle \ . \tag{2.11}$$

In this so called Reynolds decomposition, the average part $\langle \cdot \rangle$ can be a time-average for a time-independent flow, a spatial average for zonally constant flows or an ensemble average, the ensembles given by sectioned time series. However, the choice of the average determines the kind of fluctuations

$$\tilde{\boldsymbol{u}} = \boldsymbol{v} - \langle \boldsymbol{v} \rangle \ . \tag{2.12}$$

The Reynolds decomposition is done for velocity and pressure ($p = \bar{p} + \tilde{p}$) and is inserted in the Euler equation. After averaging only the evolution of the mean flow persists

$$\frac{\partial \boldsymbol{U}}{\partial t} + \langle (\boldsymbol{U} \cdot \boldsymbol{\nabla})\boldsymbol{U} \rangle + \langle (\boldsymbol{U} \cdot \boldsymbol{\nabla})\tilde{\boldsymbol{u}} \rangle + \langle (\tilde{\boldsymbol{u}} \cdot \boldsymbol{\nabla})\tilde{\boldsymbol{u}} \rangle + \langle (\tilde{\boldsymbol{u}} \cdot \boldsymbol{\nabla})\boldsymbol{U} \rangle = -\boldsymbol{\nabla}\bar{p} \ . \tag{2.13}$$

The mean velocity is invariant under the average $\langle \boldsymbol{U} \rangle = \boldsymbol{U}$ and the fluctuating velocity vanishes $\langle \tilde{\boldsymbol{u}} \rangle = 0$ as eqs. (2.11) and (2.12) yield. The same is applied to the pressure. As a consequence, the mixed terms in eq. 2.13 are zero. The Reynolds averaged Navier-Stokes equation (RANS) reads then

$$\frac{\partial \boldsymbol{U}}{\partial t} + \langle (\boldsymbol{U} \cdot \boldsymbol{\nabla})\boldsymbol{U} \rangle + \langle (\tilde{\boldsymbol{u}} \cdot \boldsymbol{\nabla})\tilde{\boldsymbol{u}} \rangle = -\boldsymbol{\nabla}\bar{p} \ . \tag{2.14}$$

As it can be seen, the eq. (2.14) still includes a term of fluctuating velocities. Since the RANS do not constitute a set of two equations split into a fluctuating and an average part, it is called the closure problem. In order to take a closer look on the fluctuating terms, the Euler equation is now treated in component notation

$$\partial_t U_i + \langle (U_j \partial_j) U_i \rangle + \langle (\tilde{u}_j \partial_j) \tilde{u}_i \rangle = -\partial_i \bar{p} \ . \tag{2.15}$$

The fluctuating term can be developed as

$$\langle (\tilde{u}_j \partial_j) \tilde{u}_i \rangle = \partial_j \langle \tilde{u}_i \tilde{u}_j \rangle - \langle \tilde{u}_i (\partial_j \tilde{u}_j) \rangle \ . \tag{2.16}$$

The last term on the right side vanishes, due to the incompressibility condition ($\boldsymbol{\nabla} \cdot \boldsymbol{v} = \partial_j \tilde{u}_j = 0$). Therefore the Euler equations reads

$$\partial_t U_i + \langle (U_j \partial_j) U_i \rangle + \partial_j \langle \tilde{u}_i \tilde{u}_j \rangle = -\partial_i \bar{p} \ . \tag{2.17}$$

The second term on the left-hand side is the convective derivative and the third term is the gradient of the so-called Reynolds stress defined as

$$R = \langle \tilde{u}_i \tilde{u}_j \rangle \ . \tag{2.18}$$

As the component notation suggests, the convective term and the Reynolds stress are tensors as for example the Reynolds stress is

$$R = \begin{bmatrix} \langle \tilde{u}_x^2 \rangle & \langle \tilde{u}_x \tilde{u}_y \rangle & \langle \tilde{u}_x \tilde{u}_z \rangle \\ \langle \tilde{u}_x \tilde{u}_y \rangle & \langle \tilde{u}_y^2 \rangle & \langle \tilde{u}_y \tilde{u}_z \rangle \\ \langle \tilde{u}_x \tilde{u}_z \rangle & \langle \tilde{u}_y \tilde{u}_z \rangle & \langle \tilde{u}_z^2 \rangle \end{bmatrix} \tag{2.19}$$

A detailed physical interpretation of the Reynolds stress can be found in section 2.6.2.

2.6.1 Two dimensional fluid dynamics in a magnetically confined plasma

In the context of a magnetically confined plasma like in the stellarator TJ-K, the dynamics can be described in two dimensions x and y, where x refers to a radial coordinate and y to a kind of the poloidal coordinate perpendicular to x and the magnetic field line. With regard to the zonal flow dynamics the Reynolds average is now chosen as spatial average over y ($\langle \cdot \rangle = \langle \cdot \rangle_Y$). For the poloidal mean flow in slab geometry the RANS-equation is

$$\partial_t U_y + \langle (U_x \partial_x) U_y \rangle_Y + \partial_x \langle \tilde{u}_x \tilde{u}_y \rangle_Y = -\partial_y \bar{p} \ . \tag{2.20}$$

The contributions $\langle (U_y \partial_y) U_y \rangle_Y$ and $\partial_y \langle \tilde{u}_y^2 \rangle_Y$ were already canceled out because the spatial derivative in y-direction of a constant is zero ($\partial_y \langle \cdot \rangle_Y = 0$). Following the same argument, the term on the right-hand side is zero because the pressure can be considered as constant on a flux surface ($\partial_y \bar{p} = \partial_y \langle p \rangle_Y = 0$), too. In the context of a constant confinement, there is no net mean in- or outward flow $U_x = 0$ as the potential is constant on a flux surface and the resulting $E \times B$ velocity is zero, too. As a consequence the second term on the left-hand side vanishes. Thus, eq. (2.20) can further be simplified and the dynamics of the zonal flow velocity can be described as

$$\partial_t U_y = -\partial_x \underbrace{\langle \tilde{u}_x \tilde{u}_y \rangle_Y}_{R} \ . \tag{2.21}$$

The expression of the average on the right-hand side is called the Reynolds stress (R) and its radial derivative is the Reynolds stress drive. Despite the suggestion of its name, the Reynolds stress drive does not necessarily enhance the zonal flow but can damp it, too. Initially, eq. (2.21) does not describe the energy transfer, but shows the way the gradient of the Reynolds stress

determines the amplitude of the zonal flow.

2.6.2 The Reynolds stress as a measure of the tilt of turbulent structures

As eq. (2.21) suggests, by excluding magnetic fluctuations that the evolution of the mean flow in a magnetic confined 2D turbulence system mainly depends on the Reynolds stress consisting of the radial and poloidal velocity fluctuations. Note that the plasma potential is the neutral fluid equivalent of

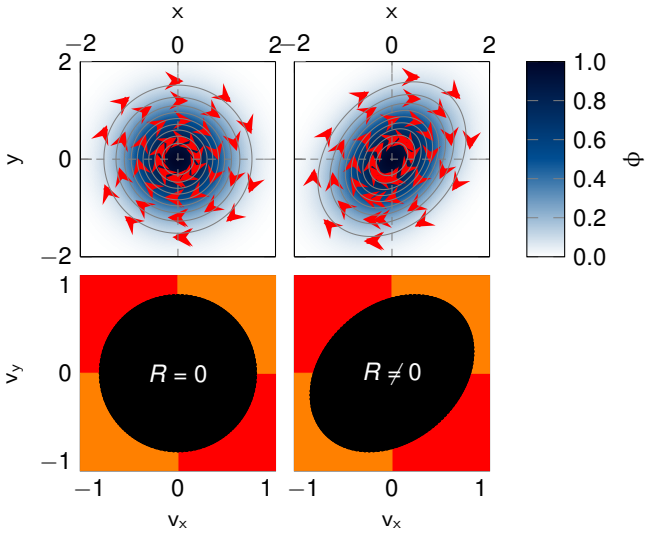

Figure 2.6: *(Top)* Scalar potential field in two dimensions with circular constant (left) and elliptical tilted (right) contours. The red arrows indicate the velocity vector field resulting from the derivatives of the potential. *(Bottom)* The velocity components plotted against each other. In the circular case, the contributions of the orange fields cancel the ones in the red field out and the Reynolds stress is zero. In the elliptical, tilted case, the resulting Reynolds stress is non-zero.

the stream function. In plasmas, electrostatic probes give direct access to the potential as stream function pendant with

$$v_i = (-1)^j B^{-1} \partial_j \phi \quad ; i, j \in [0, 1] \; ; i \neq j \quad . \tag{2.22}$$

Therefore the dynamics are determined by the change in the potential. The change in the potential, however, originates from perturbations in the plasma density. Indications are found that the strength of the coupling between potential and density is influenced by the magnetic curvature [57, 54] and the collisionality [58]. The structures can be stretched and tilted by shear flows or by the magnetic shear. An illustration of the velocity distribution resulting from a potential perturbation is shown in fig. 2.6. The distribution related to circular potential structure in 2D is opposed to that of a tilted potential structure. To this end the vector components of the resulting 2D velocity field are shown as coordinate pairs illustrated in the bottom row of fig. 2.6. For the Reynolds stress, all pair products of the distribution are summed. In the circular case the average is zero because the contributions

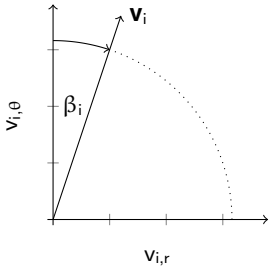

Figure 2.7: Scheme of the angle of incident (β_i) calculated from the components of the velocity fluctuations $\boldsymbol{v}_i = (v_{i,r}, v_{i,\theta})$.

in the different quadrants cancel each other (the blue ones with the orange ones). In the tilted case, the sum over the 2D distribution and, therefore, the Reynolds stress does not vanish. Hence, the Reynolds stress can be traced back to tilted potential structures. Note that an elliptically shaped distribution without tilt results in zero Reynolds stress as well because of its symmetry properties.

2.6.2.1 Quantification of structure tilt

One attempt to obtain an actual tilt angle from a data-set of velocity fluctuations in time is to calculate the angle of incident of each pair of values by taking the tangents of their slope as indicated in fig. 2.7 and average over all

pairs

$$\beta = \left\langle \arctan\left(\frac{v_{i,r}}{v_{i,\theta}}\right)\right\rangle_i \quad . \tag{2.23}$$

Another method is to calculate the averaged cross-phase between the fluctuating components by interpreting the Reynolds stress as a cross-correlation of the two different velocity components as [59, 60]

$$\cos(\alpha) = \frac{\langle \tilde{v}_r(t)\tilde{v}_\theta(t)\rangle_T}{\sigma_r \sigma_\theta} \quad . \tag{2.24}$$

Both phases can be heuristically related to each other shown in fig. 2.8. In

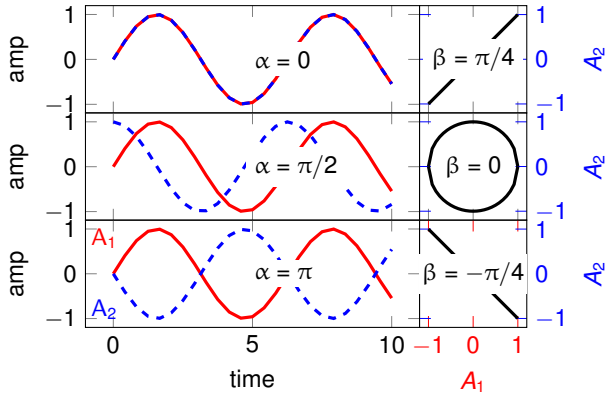

Figure 2.8: Relation between the cross-phase α of two artificial time signals $A_1(t)$ and $A_2(t)$ *(left)* and their $A_2(A_1)$ plot for different phase shifts *(right)*. The angle of incident is calculated by eq. (2.25) in the $A_2(A_1)$ plot.

the case of two identical time signals with a phase shift of zero ($\alpha = 0$) to each other, both correlate to one, i.e. they behave linear to each other. As a consequence the average slope is one which leads to $\beta = \pi/4$ (fig. 2.8-*top*). In another case with a time shift ($\alpha = \pi/2$), the average slope is zero and therefore $\beta = 0$ (fig. 2.8-*middle*). As a last consideration, the phase shift is $\alpha = \pi$ which leads to an anti-correlation, i.e. to a negative slope of minus one which results in $\beta = -\pi/4$ (fig. 2.8-*bottom*). Values for the time shift of $\alpha < 0$ and $\alpha > \pi$ are neglected because then the arccos-function is not

unique any more. These heuristic considerations lead to a presumed relation of

$$\alpha(\beta) = -2\beta + \frac{\pi}{2} \ . \tag{2.25}$$

2.6.2.2 Shear induced Reynolds stress

In context of the mechanism for the zonal flow drive (eq. 2.21), the Reynolds stress tensor for two-dimensional turbulence is reduced as

$$R = \langle \tilde{v}_x \tilde{v}_y \rangle_T \tag{2.26}$$

where $\langle \cdot \rangle_T$ denotes a temporal average allowing a poloidally resolved profile of the Reynolds stress and $\tilde{v}_i$ means the velocity fluctuations calculated from the potential fluctuations as

$$\tilde{\boldsymbol{v}} = \frac{\tilde{\boldsymbol{E}} \times \boldsymbol{B}}{B^2} = \frac{1}{B^2} \begin{pmatrix} -\partial_y \tilde{\phi} B_z + \partial_z \tilde{\phi} B_y \\ -\partial_z \tilde{\phi} B_x + \partial_x \tilde{\phi} B_z \\ -\partial_x \tilde{\phi} B_y + \partial_y \tilde{\phi} B_x \end{pmatrix} = \frac{1}{B_z} \begin{pmatrix} -\partial_y \tilde{\phi} \\ \partial_x \tilde{\phi} \\ 0 \end{pmatrix} \ . \tag{2.27}$$

Here, a magnetic field as $\boldsymbol{B} = (0, 0, B_z)$ is presumed. For the potential fluctuations the Fourier decomposition is chosen as

$$\tilde{\phi} = \phi_0 \exp\left[i \left(k_x x + k_y y - \omega t\right)\right] = \tilde{\phi}_0 \exp\left[i \left(k_x x + k_y y\right)\right] \ . \tag{2.28}$$

As a consequence, the velocity fluctuations can be rewritten as

$$\tilde{\boldsymbol{v}} = \frac{1}{B_z} \begin{pmatrix} -i k_y \\ i k_x \\ 0 \end{pmatrix} \tilde{\phi} \ . \tag{2.29}$$

For the Reynolds stress this yields [48]

$$\begin{aligned} R =& \langle \tilde{v}_x \tilde{v}_y \rangle_T = \left\langle k_x k_y \left(\frac{\tilde{\phi}}{B_z} \right)^2 \right\rangle_T = k_x k_y \left\langle \frac{\tilde{\phi}^2}{B_z^2} \right\rangle_T \\ &\propto k_x k_y \langle \tilde{\phi}_0^2 \rangle_T = R(B_z = 1) \ , \end{aligned} \tag{2.30}$$

Together with the shearing coordinates ($k_x = -V_E' \tau_L k_y$, eq. (2.8)) introduced in sec. 2.5, the Reynolds stress, induced by the electric shear, can be written

as

$$R_{\mathrm{V'_E}} = k_x k_y \, \frac{\langle \tilde{\phi}^2 \rangle_T}{B_z} = -V'_E \tau_L \, k_y^2 \frac{\langle \tilde{\phi}^2 \rangle_T}{B_z} \ . \tag{2.31}$$

The quadratic radial velocity can be expressed as $\tilde{v}_x^2 = -k_y^2 \tilde{\phi}/B_z$ and the shear dependent Reynolds stress can then be rewritten as

$$R_{\mathrm{V'_E}} = V'_E \tau_L \, \langle \tilde{v}_x^2 \rangle_T \ . \tag{2.32}$$

The relation between Reynolds stress and the shear flow can be interpreted as eddy viscosity [61, 30]

$$R = -\nu_{\mathrm{T}} \partial_x V \ . \tag{2.33}$$

The concept of eddy viscosity is used in e.g. large eddy simulations for simplicity in order to overcome the closure problem [62]. A positive correlation between the shear and the Reynolds stress, as it is the case in eq. (2.32), implies a negative turbulent eddy viscosity ν_{T}. This concept was already theoretically proposed by [63, 64] for two dimensional fluids.

In order to summarize the influence of the shear on the tilt, the first objective of this investigation is

- the tilt of turbulent structures can be quantified by the Reynolds stress. The background shear tilts turbulent vortex structures, which results in a linear dependency between shearing rate and Reynolds stress.

2.6.3 Energy transfer between turbulent energy and the mean flow

The influence of the shear induced Reynolds stress on the evolution of the kinetic energy of the poloidal mean flow is discussed. The Reynolds average is again chosen as spatial average over the poloidal angle. ($\langle \boldsymbol{u}(x,y,t) \rangle_Y = \boldsymbol{U}(x,t)$). The temporal change of the energy can be obtained by multiplying the equation for the momentum evolution (eq. (2.21)) with the poloidal mean flow U

$$\frac{1}{2} \partial_t U_y^2 = - \left(\partial_x R \right) U_y \tag{2.34}$$

The right-hand side can be expanded as

$$-\left(\partial_x R\right) U_y = -\partial_x \left(R U_y\right) + R \partial_x U_y \ , \tag{2.35}$$

and, hence, the temporal change of the mean flow energy can be written as

$$\partial_t \bar{E} + \partial_x \bar{T} = R \partial_x U_y := \mathcal{P} \ , \tag{2.36}$$

with $\bar{T} = R U_y$, which can be interpreted as a flux of the mean flows' kinetic energy [30]. The temporal evolution of the energy of the fluctuations can be derived by subtracting eq. (2.36) from a non averaged Euler equation as done in [65]

$$\partial_t \tilde{E} + \partial_x \tilde{T} = -R \partial_x U_y := -\mathcal{P} \tag{2.37}$$

with $\tilde{T} = 0.5 \langle \tilde{u}_x \tilde{u}_y \tilde{u}_y \rangle$. A comparison of the energy evolution of the mean flow eq. (2.36) with the one from the fluctuations eq. (2.37) shows the importance of the so-called production term

$$\mathcal{P} = R \partial_x U_y = -\langle \tilde{u}_x \tilde{u}_y \rangle \partial_x U_y \ . \tag{2.38}$$

The production term connects the evolution of the mean flow with the one of the fluctuations. If the production is positive ($\mathcal{P} > 0$), the term on the right-hand side in eq. (2.36) is negative and in eq. (2.37) positive. A positive $\mathcal{P}$ can be physically interpreted as an energy transfer from the turbulence into the mean flow and therefore "produces" the mean flow. Respectively, turbulence is generated by the mean flow, if the production is negative ($\mathcal{P} > 0$). The direction of the energy transfer depends on whether the Reynolds stress and the shear ($\partial_x U_y$) do have the same sign. Otherwise, the velocity field of the eddies counteracts the shear in the mean flow and energy is transferred from the mean-flow into the turbulence [66, 21, 67].

2.6.3.1 Energy transfer and time-independent (shear-) flows

In the following section a relation of the power in the zonal potential to the energy transfer is derived. Since the production term depends on the Reynolds stress influenced by the sheared flow field, a dependency of the energy transfer on the *background* shearing rate can be derived. Here, a background quantity is defined as such if both, the poloidal *and* the temporal average, are applied. In order to differentiate both averages, on the one hand, the total velocity field can be expressed by the spatial average $\langle \cdot \rangle_Y$ in

y-direction [68]

$$\boldsymbol{U}(x,t) = \langle \boldsymbol{u}(x,y,t)\rangle_Y = \langle \boldsymbol{U} + \tilde{\boldsymbol{u}}\rangle_Y \quad \tilde{\boldsymbol{u}} = \boldsymbol{u} - \boldsymbol{U} \Leftrightarrow \boldsymbol{u} = \boldsymbol{U} + \tilde{\boldsymbol{u}} \tag{2.39}$$

which is the original Reynolds average and defines the spatial fluctuations ($\tilde{\boldsymbol{u}}$) consecutively. On the other hand, the temporal average $\langle\cdot\rangle_T$ applied on the same velocity field ($\boldsymbol{u} = \boldsymbol{v}$) yields

$$\boldsymbol{V}(x,y) = \langle \boldsymbol{v}(x,y,t)\rangle_T = \langle \boldsymbol{V} + \tilde{\boldsymbol{v}}\rangle_T \quad \tilde{\boldsymbol{v}} = \boldsymbol{v} - \boldsymbol{V} \Leftrightarrow \boldsymbol{v} = \boldsymbol{V} + \tilde{\boldsymbol{v}}\ . \tag{2.40}$$

and determines the temporal fluctuations ($\tilde{\boldsymbol{v}}$). Whereas the spatially averaged velocity depends on the radius and the time, the temporal averaged velocity depends on the radius and the poloidal angle. The background shearing rate results from a spatial and temporal average of the radially changing velocity $\langle \partial_x \boldsymbol{v_y}\rangle_{Y,T}$.

Time evolution The temporal evolution of the energy of the mean flow in eq. (2.36) can be written as

$$\frac{1}{2}\partial_t U_y^2 = \frac{1}{2}\partial_t \left(\langle V_y + \tilde{v}_y\rangle_Y\ \right)^2 \tag{2.41}$$

$$= \langle V_y\rangle_Y\ \partial_t \langle \tilde{v}_y\rangle_Y\ + \frac{1}{2}\partial_t \langle \tilde{v}_y\rangle_Y^2 \tag{2.42}$$

where the relation $\partial_t \langle V_y\rangle_Y^2\ = 0$ was used. In order to determine the power of the fluctuations, an average over time is done. The first term on the right-hand side of eq. (2.42) vanishes as $\langle \partial_t \tilde{v}_y\rangle_T = -i\omega\langle \tilde{v}_y\rangle_T = 0$ because of eq. (2.40) where a fluctuating velocity $\tilde{v} = v_0 \exp(-i\omega t)$ is presumed. With the temporal average, eq. (2.42) further simplifies to

$$\left\langle \frac{1}{2}\partial_t U_y^2 \right\rangle_T = \frac{1}{2}\left\langle \partial_t \langle \tilde{v}_y\rangle_Y^2\ \right\rangle_T = -i\omega \left\langle \langle \tilde{v}_y\rangle_Y^2\ \right\rangle_T\ . \tag{2.43}$$

Note that the temporal average is not part of the Reynolds decomposition, i.e. the Reynolds average. The velocity ($\langle \tilde{v}_y\rangle = B_z^{-1}\partial_x \langle \phi\rangle_Y\ $) depends on the fluctuations in the potential ($\phi = \phi_0 \exp\left[i\left(k_x x + k_y y - \omega t\right)\right]$). Here, the poloidal wavenumber is zero $k_y = 0$ because of the poloidal average $\langle\cdot\rangle_Y$ and the potential becomes the zonal potential $\phi_{ZF} = \phi_0 \exp\left[i\left(k_x x - \omega t\right)\right]$. As a

consequence, the power in eq. (2.43) can be further expanded as

$$\begin{aligned} 0.5\left\langle \partial_t U_y^2 \right\rangle_T &= -i\omega\langle (B_z^{-1}\partial_x \phi_{ZF})^2 \rangle_T \\ &= iB_z^{-2}\omega k_x^2 \langle \phi_{ZF}^2 \rangle_T \\ &\propto \langle \phi_{ZF}^2 \rangle_T \ . \end{aligned} \tag{2.44}$$

The term in brackets denotes the power in the time-fluctuating zonal potential. It has been derived that the power of the zonal, kinetic energy is proptional to the power of the zonal potential.

Production In order to examine the influence of the background shear and the Reynolds stress on the production term, the following discussion is now treated in two parts, the Reynolds stress and the shear part. After determining the time-independent velocity in every single part, they are finally combined to the production term again.

First, the impact of a time-independent (shear-) flow on the Reynolds stress is discussed. Therefore the argument of the Reynolds stress is expanded by the Reynolds decomposition as

$$\tilde{u}_x\tilde{u}_y = (u_x - U_x)(u_y - U_y) \tag{2.45}$$

$$= u_x u_y - u_x U_y - u_y U_x + U_x U_y \tag{2.46}$$

$$= u_x u_y - u_x U_y \ . \tag{2.47}$$

The poloidal mean flow can further be separated in a time-independent V_y and a time-dependent v_y part as

$$U_y = \langle u \rangle_Y = \langle V_y + v_y \rangle_Y \tag{2.48}$$

and for the Reynolds stress in eq. (2.47) follows

$$\tilde{u}_x\tilde{u}_y = (V_x + \tilde{v}_x)(V_y + \tilde{v}_y) - (V_x + \tilde{v}_x)\langle V_y + \tilde{v}_y \rangle_Y \tag{2.49}$$

$$= \tilde{v}_x V_y + \tilde{v}_x\tilde{v}_y - [\ \tilde{v}_x\langle V_y \rangle_Y \ + \tilde{v}_x\langle \tilde{v}_y \rangle_Y \ ] \ . \tag{2.50}$$

In the next step the Reynolds average, here as space average over the coordinate y, is applied and the Reynolds stress can further be written as

$$\begin{aligned} \langle \tilde{u}_x\tilde{u}_y \rangle_Y \ &= \langle \tilde{v}_x V_y \rangle_Y \ + \langle \tilde{v}_x\tilde{v}_y \rangle_Y \\ &\quad - [\ \langle \tilde{v}_x\langle V_y \rangle_Y \ \rangle_Y \ + \langle \tilde{v}_x\langle \tilde{v}_y \rangle_Y \ \rangle_Y \ ] \ . \end{aligned} \tag{2.51}$$

The last term vanishes because

$$\langle \tilde{v}_x \langle \cdot \rangle_Y \ \rangle_Y \ = \underbrace{\langle \tilde{v}_x \rangle_Y}_{0} \ \langle \cdot \rangle_Y = 0 \ . \tag{2.52}$$

Thus the y-averaged Reynolds stress simplifies to

$$\langle \tilde{u}_x \tilde{u}_y \rangle_Y \ = \langle \tilde{v}_x V_y \rangle_Y \ + \langle \tilde{v}_x \tilde{v}_y \rangle_Y \ . \tag{2.53}$$

Second, the shear part is treated and expanded by the time-separation from eq. (2.40)

$$\partial_x U_y = \partial_x \left\langle V_y + \tilde{v}_y \right\rangle_Y \tag{2.54}$$

$$= \partial_x \langle V_y \rangle_Y \ + \partial_x \langle \tilde{v}_y \rangle_Y \ . \tag{2.55}$$

Hence, the shear can be separated into a time-dependent and a time-independent part, where the first part satisfies the condition of a background quantity.

Finally eq. (2.55) and eq. (2.53) are multiplied to the production term, which is temporally averaged, similar to eq. (2.43)

$$\langle \mathcal{P} \rangle_T = \langle \ \langle \tilde{u}_x \tilde{u}_y \rangle_Y \ \partial_x U_y \ \rangle_T \tag{2.56}$$

$$= \langle \ [\ \langle \tilde{v}_x V_y \rangle_Y \ + \langle \tilde{v}_x \tilde{v}_y \rangle_Y \ ] \ [\ \partial_x \langle V_y \rangle_Y \ + \partial_x \langle \tilde{v}_y \rangle_Y \ ] \ \rangle_T \tag{2.57}$$

$$= \langle \ \langle \tilde{v}_x V_y \rangle_Y \ \partial_x \langle V_y \rangle_Y \ + \ \langle \tilde{v}_x V_y \rangle_Y \ \partial_x \langle \tilde{v}_y \rangle_Y$$

$$+ \ \ \langle \tilde{v}_x \tilde{v}_y \rangle_Y \ \partial_x \langle V_y \rangle_Y \ \ + \ \langle \tilde{v}_x \tilde{v}_y \rangle_Y \ \partial_x \langle \tilde{v}_y \rangle_Y \ \rangle_T \ . \tag{2.58}$$

The first term vanishes ($\langle \tilde{v}_x \rangle_T = 0$) which leads to

$$\langle \mathcal{P} \rangle_T = \langle \ \langle \tilde{v}_x V_y \rangle_Y \ \partial_x \langle \tilde{v}_y \rangle_Y \ \rangle_T + \langle \tilde{v}_x \tilde{v}_y \rangle_{Y,T} \partial_x \langle V_y \rangle_Y$$

$$+ \langle \ \langle \tilde{v}_x \tilde{v}_y \rangle_Y \ \partial_x \langle \tilde{v}_y \rangle_Y \ \rangle_T \ . \tag{2.59}$$

The bracket $\langle \cdot \rangle_{Y,T}$ denotes a poloidal average as well as a temporal average. The first term depends on the time-independent, poloidal velocity (V_y), the second on the background shear ($\partial_x y \rangle_Y$) and the third term consists only of fluctuating velocities. The second term shows that the energy transfer into the poloidal mean flow depends on the product of the background Reynolds stress (poloidally and temporal averaged RS) and the background shear. It can further be shown, by equating eq. (2.44) with eq. (2.59), that the power in the zonally averaged potential depends on the second term in eq. (2.59),

too, because of

$$\langle \partial_t \bar{E} \rangle_T = \langle \mathcal{P} \rangle_T \qquad + C \tag{2.60}$$

$$\langle \phi_{ZF}^2 \rangle_T \propto \langle \tilde{v}_x \tilde{v}_y \rangle_{Y,T} \partial_x \langle V_y \rangle \qquad + D \tag{2.61}$$

where C and D are residual terms from eq. (2.36), for C and eq. (2.59), for D which includes C. The positive correlation $R \propto V_E'$, derived from eq. (2.32), has some effects on the energy transfer from the fluctuations into the time-independent mean flow. The third term in eq. (2.59) consists of the background RS and shear. If the RS is now replaced by eq. (2.32), the production term reveals a quadratic dependency on the background $E \times B$ shear.

$$\mathcal{P}_{\text{shear}} = \langle \tilde{v}_x \tilde{v}_y \rangle \frac{dV}{dx} \tag{2.62}$$

$$= \tau_L \langle \tilde{v}_x^2 \rangle_T \left(\frac{dV}{dx} \right)^2 = -\nu_T \left(\frac{dV}{dx} \right)^2 . \tag{2.63}$$

This relation was derived in [30] for two-dimensional fluids.

The influence of shear on the energy transfer between zonal flows and two-dimensional turbulence can be summarized in two further objectives of this investigation. The first states that

- the linear dependency between Reynolds stress and shearing rate results in a quadratic dependency between the energy-transfer, i.e. the production term, and the shearing rate.

Since the energy transfer effects the power distribution the second working hypothesis follows directly:

- as the energy transfer from the turbulence into the ZF rises with the background shearing rate, the spectral power is redistributed such that the power in the ZF rises compared to other modes, i.e. the relative ZF-power rises.

2.7 Drift-wave dynamics

Small perturbations in the plasma density can lead to so-called drift-waves which determine the dynamics in the edge of fusion-like magnetically confined plasmas [67] and constitute the second picture of plasma turbulence in this work. First, a qualitative description of drift-waves is given. Then the more analytical approach of the Hasegawa-Wakatani equations is discussed. By adiabatic approximation, these equations can be reduced to the Hasegawa-Mima equation. Based on this equation, the three-wave interaction is explained in Fourier space and the resonant manifold is explained as a set of possible couplings. In the last section the influence of a shear on the resonant manifold is discussed.

2.7.1 Qualitative description

In the region of the density gradient, density perturbations can occur, which spread parallel to the magnetic field. Their parallel elongation is characteristically much larger than their perpendicular width. Due to their lower inertia, the electrons follow the perturbation faster than the ions, so that electric fields are established. Because of quasi-neutrality the electric field parallel to the magnetic field induce electric field perpendicular to the magnetic field (see fig. 2.9). Together with the magnetic field, $E \times B$ drifts are formed,

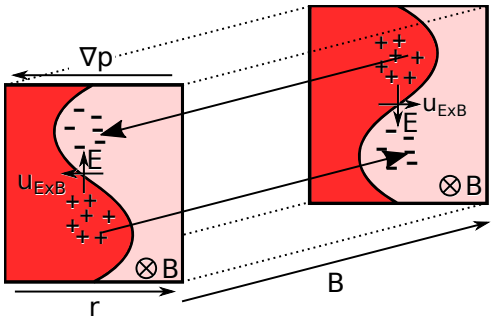

Figure 2.9: Electrons follow the density perturbation elongated to the magnetic field faster then the ions resulting in electric fields. The resulting $E \times B$ drifts shift the isobars leading to an effective movement of the perturbation in the electron-diamagnetic drift direction (adapted from [69, 67, 41]).

which lead to a shift of the isobars. Effectively, this displacement results in a drift of the wave in the electron-diamagnetic drift direction. The case is called adiabatic limit, if the electron response to the density disturbance is instantaneous. Then drift waves do not contribute to a radial net transport. However, if the electron response is delayed, e.g. due to resistivity or Landau damping, the drift waves become unstable and thus contribute to outward transport. The dynamics of the drift waves can be described in general by the Hasegawa-Wakatani equations and for the special adiabatic case by the Hasegawa-Mima equation.

2.7.2 Hasegawa-Wakatani equations

In this section, the Hasegawa-Wakatani equations which model the drift-wave turbulence are described only briefly. A more detailed derivation can be found in [58, 67, 57]. Nevertheless, this section motivates the use of the simplified Hasegawa-Mima equation. In the Hasegawa-Wakatani model, a first equation for the vorticity evolution can be derived from the quasi-neutrality ($\boldsymbol{\nabla} \cdot \boldsymbol{j} = 0$). A second equation, for the density, gives the continuity equation.

$$\partial_t \omega + \{\phi, \omega\} = \nabla_\parallel (n - \phi) / \nu \tag{2.64}$$

$$\partial_t n + \{\phi, n\} + K_n \partial_y \phi = \nabla_\parallel (n - \phi) / \nu \, . \tag{2.65}$$

Here, only the dimensionless quantities are shown. ϕ is the fluctuating potential normalized on the temperature, n the density fluctuations normalized on the background density, $\omega = \mathrm{rot}(\boldsymbol{\nabla}\phi)$ the vorticity, ν the collisionality and K_n the inverse density gradient length. Quantities of length are normalized on the drift parameter ($\rho_s = \sqrt{m_i T_e}/(eB)$) and quantities of time on the ion-cyclotron frequency ($\omega_{\mathrm{ci}} = eB/m_i$). Further, the advective derivative in 2D is expressed in terms of Poisson brackets $\{\phi, n\} = \partial_x \phi \partial_y n - \partial_y \phi \partial_x n$. The right-hand side of both equations describes the parallel dynamics of the electrons as they escape the initial density perturbation. The perpendicular dynamics are governed by the ions through the polarization drift. Important for the dynamics is the strength of the coupling between density and potential. This depends on the adiabaticity ($1/\nu$) [58] and the curvature effects of the magnetic field which require an extension of the Hasegawa-Wakatani equations [57]. A decoupling results in a time-shift between density and potential destabilizing the drift waves. Stronger curvature can lead to stronger instabilities of interchange nature.

2.7.3 Hasegawa-Mima equation

Fusion relevant plasmas usually operate at high temperature and hence high adiabaticity can be assumed. Consecutively, density and potential are equal, i.e. $n = \phi$. Now the vorticity eq. (2.64) is subtracted from the density fluctuations eq. (2.65) and the Hasegawa-Wakatani equations reduce to

$$\partial_t (\phi - \omega) + K_n \partial_y \phi = \{\phi, \omega\} \tag{2.66}$$

the Hasegawa-Mima equation [31]. This describes the evolution of the potential perturbations which can be set to $\hat{\phi} = \exp[i(\boldsymbol{kr} - \omega t)]$ where ω is the angular frequency.

Dispersion relation Now a dispersion relation can be derived as

$$\omega_{\mathrm{DW}}(\boldsymbol{k}) = \frac{K_n k_y}{1 + k^2} \tag{2.67}$$

Here, the inverse density gradient length $K_n = \rho_s / L_n$ can be deduced to the diamagnetic drift velocity when the normalization is removed ($u_{\mathrm{dia}} = -B^{-2} \boldsymbol{\nabla} p \times B = T_e / (e L_n B)$). The diamagnetic drift velocity describes the propagation of the waves (sec. 2.7.1). The denominator shows the influence of the polarization drift.

Non-linear interaction In order to analyze the non-linear behavior, the right-hand side can be rewritten as

$$\begin{aligned} \partial_t \left(\phi + \nabla^2 \phi\right) + i\omega_{\mathrm{DW}} \phi &= -\left(\boldsymbol{\nabla}\phi \times \boldsymbol{e}_z \boldsymbol{\nabla}\right) \nabla^2 \phi \\ &= \left(\boldsymbol{e}_z \times \boldsymbol{\nabla}\phi \cdot \boldsymbol{\nabla}\right) \nabla^2 \phi \end{aligned} \tag{2.68}$$

because of the circular-shift property of the cross-product. In the next step the right-hand side of eq. (2.68) is treated in Fourier space. For a discrete sampled potential, the Fourier representation can be written as

$$\phi = \sum_k \hat{\phi}_k \mathrm{e}^{i \hat{\boldsymbol{k}} \hat{\boldsymbol{r}}} \tag{2.69}$$

where k denotes a wavenumber dependency. Inserted in eq. (2.68) follows

$$\left[\partial_t \left(1+\nabla^2\right) + i\omega_{\mathrm{DW}}\right] \sum_k \hat{\phi}_k \mathrm{e}^{i\boldsymbol{k}\hat{\boldsymbol{r}}} = \left[\left(\hat{\boldsymbol{e}}_z \times \boldsymbol{\nabla} \sum_{k_1} \hat{\phi}_{k_1} \mathrm{e}^{i\boldsymbol{k_1}\hat{\boldsymbol{r}}}\right) \boldsymbol{\nabla}\right] \cdot \nabla^2 \sum_{k_2} \hat{\phi}_{k_2} \mathrm{e}^{i\boldsymbol{k_2}\hat{\boldsymbol{r}}} \,. \tag{2.70}$$

The term on the right hand side developes and can be defined as [70]

$$\sum_{k_1}\sum_{k_2} f_{k_1 k_2} := \sum_{k_1}\sum_{k_2} (\hat{\boldsymbol{e}}_z \times \boldsymbol{k}_1) \cdot \boldsymbol{k_2}\, \hat{\phi}_{k_1} \hat{\phi}_{k_2} k_2^2 \mathrm{e}^{i(\boldsymbol{k_1}+\boldsymbol{k_2})\cdot\hat{\boldsymbol{r}}} \,. \tag{2.71}$$

With the property

$$\sum_{k_1}\sum_{k_2} f_{k_1 k_2} = \sum_{k_2}\sum_{k_1} f_{k_2 k_1} \tag{2.72}$$

and the circular-shift property of the triple product ($(\hat{\boldsymbol{e}}_z \times \boldsymbol{k_2}) \cdot \boldsymbol{k_1} = -(\boldsymbol{k_1} \times \boldsymbol{k_2}) \cdot \hat{\boldsymbol{e}}_z$) follows

$$\begin{aligned}\sum_{k_1}\sum_{k_2} f_{k_1 k_2} &= \frac{1}{2}\sum_{k_1}\sum_{k_2} (f_{k_1 k_2} + f_{k_2 k_1}) \\ &= \frac{1}{2}\sum_{k_1}\sum_{k_2} (\boldsymbol{k_1} \times \boldsymbol{k_2}) \cdot \hat{\boldsymbol{e}}_z\, \hat{\phi}_{k_1} \hat{\phi}_{k_2} \left(k_2^2 - k_1^2\right) \mathrm{e}^{i(\boldsymbol{k_1}+\boldsymbol{k_2})\cdot\hat{\boldsymbol{r}}} \,.\end{aligned} \tag{2.73}$$

Now eq. (2.73) is multiplied by $\mathrm{e}^{-i\boldsymbol{k_3 r}}$ and summed over $\boldsymbol{r}$ which leads to

$$\frac{1}{2}\sum_{\hat{\boldsymbol{r}}}\sum_{k_1}\sum_{k_2} (\boldsymbol{k_1} \times \boldsymbol{k_2}) \cdot \hat{\boldsymbol{e}}_z\, \hat{\phi}_{k_1} \hat{\phi}_{k_2} \left(k_2^2 - k_1^2\right) \mathrm{e}^{i(\boldsymbol{k_1}+\boldsymbol{k_2}-\boldsymbol{k_3})\cdot\hat{\boldsymbol{r}}} \,. \tag{2.74}$$

The exponential part is a delta-function

$$\frac{1}{2}\sum_{k_1}\sum_{k_2} (\boldsymbol{k_1} \times \boldsymbol{k_2}) \cdot \hat{\boldsymbol{e}}_z\, \hat{\phi}_{k_1} \hat{\phi}_{k_2} \left(k_2^2 - k_1^2\right) \delta(\boldsymbol{k_1} + \boldsymbol{k_2} - \boldsymbol{k_3}) \,. \tag{2.75}$$

The expression gives a contribution when the argument of δ is zero: $\boldsymbol{k_1} + \boldsymbol{k_2} = \boldsymbol{k_3}$. It follows

$$\frac{1}{2} \sum_{k_1+k_2=k_3} (\boldsymbol{k_1} \times \boldsymbol{k_2}) \cdot \hat{\boldsymbol{e}}_z \left(k_2^2 - k_1^2\right) \hat{\phi}_{k_1} \hat{\phi}_{k_2} \ . \tag{2.76}$$

Finally the Fourier transformed Hasegawa-Mima yields

$$\partial_t \hat{\phi}_{k_3}(t) + i\omega_{\mathrm{DW}} \hat{\phi}_{k_3}(t) = \frac{1}{2} \sum_{k_1+k_2=k_3} \Lambda_{k_1,k_2} \hat{\phi}_{k_1}(t)\ \hat{\phi}_{k_2}(t) \tag{2.77}$$

where on the left-hand side the drift-wave dispersion relation is ω_{DW} and on the right-hand side there is the transfer term, with $\Lambda_{k_1,k_2} = (1 + k_3^2)^{-1} (\boldsymbol{k_1} \times \boldsymbol{k_2}) \cdot \hat{\boldsymbol{e}}_z \left(k_2^2 - k_1^2\right)$ as the transfer coefficient [31]. The sign of the transfer coefficient determines the direction of the energy transfer and its magnitude the strength. The sum over $\boldsymbol{k}_1$, $\boldsymbol{k}_2$ is limited

$$\boldsymbol{k}_1 + \boldsymbol{k}_2 = \boldsymbol{k}_3 \ . \tag{2.78}$$

It denotes a resonant condition in wavenumber-space and describes a three-wave interaction. Physically this can be interpreted as a kind of momentum balance where scattering is neglected [71, 72]. The three wave interaction opens the possibility of a coupling between small and large wavenumbers, i.e. the interaction between large turbulent structures and small turbulent structures. For each wavenumber in eq. (2.78) a frequency can be calculated with the dispersion relation eq. (2.67) $(\omega_1(k_1), \omega_2(k_2), \omega_3(k_3))$. For a resonant three-wave interaction the resonant condition has to be fulfilled in both, wavenumber- and frequency-space

$$\omega_1(\boldsymbol{k_1}) + \omega_2(\boldsymbol{k_2}) = \omega_3(\boldsymbol{k_3}) + \Delta\omega \quad \text{and} \quad \boldsymbol{k_1} + \boldsymbol{k_2} = \boldsymbol{k_3} \ . \tag{2.79}$$

Resonant manifold Both resonance conditions eq. (2.78,2.79) are connected by the dispersion relation eq. (2.67). As a consequence, only a distinct set of couplings is possible. For a specific mode this set of possible couplings is called the resonant manifold [72] and is shown in Euklidian space as the band-like structure in fig.2.10. Here, the randomly picked mode for illustrative purpose is chosen at $k_3 = (0.6, 0.4)$, whereas the ordinate shows the set of possible couplings of $\boldsymbol{k_2}$ in x-direction and the abscissa the ones in y-direction. The band-width is determined by the uncertainty in $\Delta\omega \to 0$. A special solution of the resonance condition in the wavenumber space is the ZF, because as a

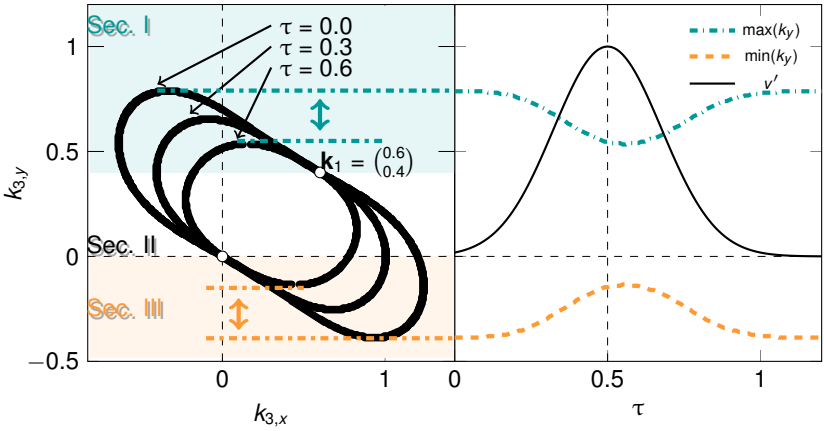

Figure 2.10: Illustration of the effect of shear flow on the extent of the resonance manifold. *Left:* The manifold (black band), $\mathbf{k}_1 = (0.6, 0.4)$ coupling with $\mathbf{k}_3$, shrinks with time τ in sections I and III. *Right:* A temporal varying shear v' (black solid line) leads to a dip in the extent of the manifold with respect to $k_{3,y}$.

trivial zero solution it is always part of the manifold ($\boldsymbol{k_i} = (k_x, 0)$).

The influence of the shear on the manifold In a next step, the influence of a constant shear on the resonant manifold is discussed, following [35]. To this end, the so-called shearing coordinates, similar to [73], are introduced as before mentioned in sec. 2.5. Hereby, the radial wavenumber is modified (eq: 2.8: $k_x' = k_x - k_y v' \tau$ with $\tau = t - t_0$) where t_0 is an initial time. In a magnetically confined turbulent system, it is almost impossible to determine an initial time of turbulence. This leads to time-dependent shear considerations, later in this section. The shearing coordinates (2.8) enter the dispersion relation. As a consequence, the change in the radial wavenumber due to the shear changes the coupling space in wavenumber- and frequency space. The wavenumber space reduces to smaller wavenumbers. Since now only small wavenumbers are available as coupling partners, their probability increases of being part of a coupling. Small scale turbulent structures (i.e. large wavenumbers) are forced to couple to the large flow structures (i.e. small wavenumbers). Physically, the mechanism is similar to the straining-out process of eddies, which explains the turbulence suppression by tilting and

incorporation, rather than by a breakup, of the vortices [47, 20]. Since the possibility of a coupling with the ZF ($k_y = 0$) is always a valid solution of the resonance conditions, independently of the shear, the probability of a coupling with the ZF increases at higher shear as the set of possible couplings decreases [35] in an evenly distributed probability density. It is argued that this is the mechanism behind large-scale structure formation in quasi 2D turbulent systems [74], such as atmospheric turbulence or plasma turbulence in toroidal fusion devices. These mesoscopic turbulent flows are, therefore, always part of the resonance manifold as a persisting component coupling with the drift waves. As being shear flows themselves, this leads to a self-amplification of the ZF and a suppression of the primary instability. The coupling probability of each Fourier mode is influenced by the transfer term $\Lambda_{\boldsymbol{k_1},\boldsymbol{k_2}}$ which determines the strength and direction of the coupling, i.e. whether a Fourier mode couples with another mode to a third mode or a three mode system is reduced to a two mode system. Gürcan argues that the strength of the coupling into the ZF reduced at advanced time [35].

For a further investigation of the manifold shrinking effect in the context of ZF drive the current model needs to be extended. As already pointed out in the original paper, a constant shear cannot capture the ZF dynamics [35]. Therefore the shear, by which $k'_{i,x}$ is modified (cf. Eq. (2.8)), is allowed to vary with time. To match the burst-like flow dynamics, found in the experiment TJ-K, the shear is modeled as $v'(\tau) \propto \exp(-\tau^2)$ in the following calculations. The effect on the resonance manifold is illustrated in Fig. 2.10. Here, the mode $\mathbf{k}_1 = (0.6, 0.4)$ is chosen as arbitrary example wave vector. Its manifold is shown on the left-hand side as a black band for the three time points $\tau = 0, 0.3$, and 0.6. With increasing time the manifold shrinks in its extent (marked as sec. I and III). There are two stationary solutions for the ZF (white dots), since $k_{1,y}$ does not change and $k_{2,y}$ is a linear combination of $k_{1,y}$ and $k_{3,y}$: first $k_{3,y} = 0$, second $k_{3,y} = 0.4$ where $k_{2,y} = 0$. The temporal evolution of the maximum (dashed line) and minimum (dashed-dotted line) extent of the manifold, with respect to $k_{3,y}$, is shown on the right-hand side of Fig. 2.10. The manifold shrinks with increasing shear (black solid line) and reaches a minimum in size after the shear becomes maximal ($\tau = 0.5$). This delay exists because $k'_{i,x}$ continuously shrinks with time at a non-zero shear, too (cf. Eq. (2.8)). When the shear decreases again the manifold expands back to its original state.

The behavior of the manifold under flow shear is the last object of this investigation which is stated as the following objective

- under the constraints of the resonance conditions in both, wavenumber and frequency space, and the dispersion relation, the zonal flow as time-dependent shear initially reduces the set of possible couplings and leads to a contraction of the resonant manifold.

2.7.4 Growth rate of drift waves

Since the shearing rate is classified by comparison with the growth rate [75], this section shortly discusses instabilities of drift-waves. Further, the shear can have an influence on the growth rate as discussed in this section.

Geometry effects If potential and density are not strongly coupled but experience a time-delay δ, drift-waves may become unstable depending of the direction of the time-shift

$$\frac{\tilde{n}}{\bar{n}} = (1 + i\delta)\frac{e\tilde{\phi}}{T_e} \ . \tag{2.80}$$

This can be modelled as a change in the adiabaticity in the Hasegawa-Wakatani equations which depends on parameters as the ion mass, the temperature and the density. Eq. 2.80 now leads to a different drift equation resulting in an unstable drift-mode for positive δ and in a stabilization of the mode for negative δ [41]. A growth rate can be calculated, which is a measure of how quickly the waves become unstable. Besides the collisionality as a contributor to the growth rate (c.f. eq. (2.65, 2.64)), it is theoretically found that the growth rate reveals asymmetries within a flux surface caused by the magnetic field configuration [76]. Thereby an estimation of the maximum growth rates can be calculated as[1]

$$\gamma \propto -\Omega_* + F\Omega_\mathrm{d} \tag{2.81}$$

where Ω_* depends on the density gradient length and F on the ratio between ion- and electron temperature. The so-called $\boldsymbol{\nabla} B$ drift frequency further depends on

$$\Omega_\mathrm{d} \propto -\frac{\kappa_n}{\sqrt{g^{ss}}} + \frac{\kappa_g}{\sqrt{g^{ss}}}\frac{B_0}{B}\chi_g\left(\Lambda + \frac{k_s}{k_\alpha}\right) \ . \tag{2.82}$$

[1] A short derivation of the geometry dependent growth rate can also be found in the appendix of [56] (german).

Hereby κ_n, κ_g are the normal and geodesic curvature respectively, g^{ss} the covariant metric tensor element with s as radial coordinate, $\chi_g = a^2 g^{ss} (2q)^{-1}$, with a as minor radius and q the safety factor, Λ is the field-line integrated local magnetic shear. The last term in brackets is the ration between radial and poloidal wavenumber. These parameters are the properties of the magnetic field configuration in particular determining the poloidal asymmetry in the growth rate.

Shear effects In addition to the effects of the magnetic field structure, shear flows can influence the time-lag between potential and density as well. This time-lag is also considered as a main contributor to turbulent transport [60, 54]. A relation between the growth- and shearing rate is estimated. Turbulent transport can be expressed as a diffusive transport down the density gradient via the mixing length estimate

$$D_{\mathrm{Turb}} \approx \frac{L_c^2}{\tau_{\mathrm{to}}} \ . \tag{2.83}$$

The diffusion can be understood as eddies of diameter L_c scooping particles towards the vessel wall within half of their turnover time (τ_{to}). The diameter

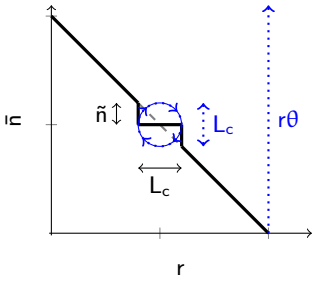

Figure 2.11: The concept of radial diffusion induced by the turnover of eddies. In order to restore the background gradient the eddy has to do half a turn. Hereby, particles are moved radially outwards (adapted from [11]).

L_c can be understood as radial correlation length and can be approximated

as $L_c \approx \pi/k_r$. The resultant diffusion coefficient is

$$D_{\mathrm{Turb}} \approx \frac{\pi^2}{k_r^2 \tau_{\mathrm{to}}} = \frac{\pi^2}{k_\theta^2 {V'_{E\times B}}^2 \tau_{\mathrm{to}}^3} \ . \tag{2.84}$$

In the last step, the shearing coordinates have been used ($k'_r = k_\theta V'_{E\times B}\tau_{\mathrm{to}}$, cf. sec. 2.5). The growth rate can be approximated by $\gamma = 1/\tau_{\mathrm{to}}$ which results in

$$\gamma_{\mathrm{shear}} \approx \frac{D_{\mathrm{Turb}}^{1/3} k_\theta^{2/3} {V'_{E\times B}}^{2/3}}{\pi^{2/3}} \propto {V'_{E\times B}}^{2/3} \ . \tag{2.85}$$

This dependency is derived by Biglari-Diamond-Terry (BDT) [77], too. With an increase of a shear, the growth rate is supposed to increase, too. Since eq. (2.85) is derived from a chain of approximations, a change of the dependency is possible, especially in the transition from low to high confinement where different phenomena may come into play.

2.8 Summary of main hypotheses and theoretical considerations

Shear flows in magnetically confined, toroidal plasmas are divided in stationary background shear flow and in time-dependent zonal flows. Both can be described by using the so-called shearing coordinates and can be integrated into various kinds of turbulent models. The plasma dynamics can be pictured using the Reynolds averaged Navier-Stokes (RANS) equations from fluid mechanics or using the description of drift waves.

- The tilt of turbulent structures can be quantified by the Reynolds stress. The background shear tilts turbulent vortex structures, which results in a linear dependency between shearing rate and Reynolds stress.

This tilt can be quantified by the mean cross-phase or by the angle of incident which do have a linear dependency, too. As the Reynolds stress is part of the production term, the energy transfer is influenced in favor of large scale mean flows such as zonal flows. A detailed derivation shows that the energy transfer depends quadratically on the stationary shearing rate.

- The linear dependency between Reynolds stress and shearing rate results in a quadratic dependency between the energy-transfer, i.e. the production term, and the shearing rate [30].

- As the energy transfer from the turbulence into the ZF rises with the background shearing rate, the spectral power is redistributed such that the power in the ZF rises compared to other modes, i.e. the relative ZF-power rises.

In the picture of drift waves, the nonlinear behavior can be described by three-wave interaction. Following a specific dispersion relation the waves have to satisfy the resonance condition in wavenumber- and frequency space. So only a distinct set of possible couplings is possible.

- Under the constraints of the resonance conditions in wavenumber frequency space and the dispersion relation, the zonal flow as a time-dependent shear initially reduces the set of possible couplings and leads to a contraction of the resonant manifold. Later, because of a decreasing zonal flow, the resonant manifold expands back to its original state.

Chapter 3

Stellarator TJ-K and experimental setup

All studies are performed at the stellarator experiment TJ-K[1]. After a short introduction of the stellarator TJ-K, the principles of diagnostics used in this work are explained (sec. 3.1). Sec. 3.2 explains plasma biasing to show how the equilibrium profile of the plasma potential and, in consequence, the background shear changes. Fig. 3.1 shows that the plasma is shaped by the externally applied magnetic field. The "snake-like" plasma body changes its shape in the poloidal cross-section depending on the toroidal position in contrast to a tokamak where the shape of the cross-section is toroidally the same. Selected inlays in fig. 3.1 show that the shape can change from a triangular to a more elliptical shape. The major radius of TJ-K is $R_0 = 0.6\,\mathrm{m}$ and the plasma radius $r_0 = 0.1\,\mathrm{m}$. The twist of the magnetic field line varies radially between $\iota = 0.2 - 0.3$. The peak density is at around $n_e = 1 \cdot 10^{17}\,\mathrm{m}^{-3}$. For this work the plasma has been heated by microwaves with a frequency of 2.45 GHz at a power of 2.4 kW. This leads to low temperatures of $T_i \leq 1\,\mathrm{eV}$,$T_e \leq 15\,\mathrm{eV}$ [80, 81], which provides the possibility to analyze the plasma within the confinement region by means of Langmuir probes and to control the plasma equilibrium with a biased electrode placed inside the confinement region.

The main diagnostics are the movable 2D unit carrying different kinds of probes (Port O6) and an array of 128 Langmuir probes (Port O2). A bias voltage is applied between an electrode inside the confinement (Port T6) and limiter plates (Port O3/O5). The limiter plates are galvanically connected to the vessel wall. The plates define a slightly smaller area than the confinement given by the magnetic field. This ensures that the biasing effect only applies to the plasma inside the confinement region. With this kind of biasing the

[1] TJ-K was built by the CIEMAT in Madrid as TJ-IU [78] where it was operated with high temperature plasmas [28]. It is a type torsatron stellarator despite the abbreviation (TJ - Tokamak de la Junta de Energia Nuclear) maintained for administrative reasons [79]. The experiment moved to Kiel (what the K stands for) and later to Stuttgart.

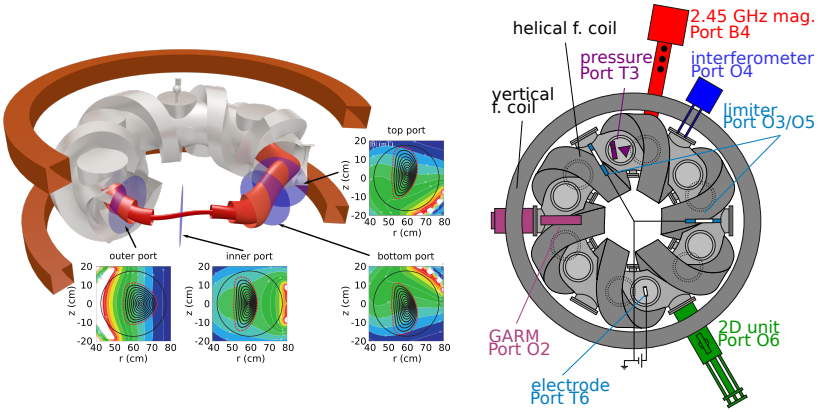

Figure 3.1: Schematic view on the stellarator TJ-K. It shows how the plasma shape changes depending on the toroidal position. The calculations of the magnetic field are taken from [56].

control of the $E\times B$ shearing rate is achieved.

The stellarator TJ-K is used for investigations in new heating scenarios [82, 83], plasma diagnostics [84, 85] and intermittent events in the scrape-off layer outside the confinement region [86, 87]. Further, studies of the plasma turbulence in the stellarator TJ-K revealed that the dynamics are dominated by drift waves similar to the dynamics at the edge of the confinement region in fusion plasmas [29]. The magnetic fluctuations are negligible [88]. The elongation of the turbulent structures in the parallel direction ($L_\parallel$) is much larger than their perpendicular width ($L_\perp$ with $L_\parallel \gg L_\perp$) [89]. The two-dimensional character of the turbulence is confirmed by the inverse-cascade [45] and the power laws [46]. Since in standard TJ-K plasmas the electric field and therefore the $E\times B$ rotation is weak, the drift waves are moving in the electron diamagnetic drift [90]. The wavenumber-frequency ($k-f$) spectrum indicates a doppler shifted dispersion relation following drift wave dynamics [56].

3.1 Diagnostics

The low temperature plasmas in TJ-K allow to obtain important equilibrium parameters, as the electron temperature and the density, inside the

confinement region by invasive diagnostics as the swept Langmuir probe (sec. 3.1.1). By modification of this Langmuir probe, it is even possible to measure potential and density fluctuations (sec. 3.1.3). The emissive probe allows measuring the plasma potential directly, which is important to calculate the equilibrium $E\times B$-velocities and the shear (sec. 3.1.2).

3.1.1 Langmuir probe

The standard Langmuir probe in TJ-K is a tungsten wire of diameter ø=200 µm. Except its probehead it is shielded co-axially by a ceramic - metal - ceramic tube combination. The probe is biased by a slowly changing voltage (U_{PBias}) with respect to ground with a frequency of $f_{\mathrm{PBias}} = 10\,\mathrm{Hz}$. The measured return current over the bias voltage results then in a Langmuir characteristic shown in fig. 3.2. The range from $U_{\mathrm{PBias}} \lessapprox \phi_{\mathrm{pl}}$ can be modeled by

$$I_{\mathrm{PBias}}(U_{\mathrm{PBias}}) = I_{i,\mathrm{sat}} + I_{e,\mathrm{sat}} \exp\left(-\frac{\mathrm{e}\,(\phi_{\mathrm{pl}} - U_{\mathrm{PBias}})}{T_{\mathrm{e}}}\right) \tag{3.1}$$

where $I_{i,\mathrm{sat}}$ is the ion saturation current, $I_{e,\mathrm{sat}}$ the electron saturation current, ϕ_{pl} the plasma potential (red, dashed line in fig. 3.2) and T_{e} the electron temperature. The characteristic can be classified into three regions [91]:

- The electron saturation region is defined in the range of $\phi_{\mathrm{pl}} \leq U_{\mathrm{PBias}}$. In an ideal case with a planar Langmuir probe head (gray-thick line in fig. 3.2), all electrons next to the probe are drawn and the current saturates. Different probe-head-geometries as well as a magnetized plasma lead to different electron saturation currents [41].

- In the electron repelling region, at lower voltages $U_{\mathrm{PBias}} < \phi_{\mathrm{pl}}$, only electrons with a high thermal velocity can overcome the Coulomb barrier to reach the probe tip. Towards more negative bias, this leads to an exponential decay of the probe current. The electron temperature can be obtained from a fit of the exponential part of the characteristic shown in fig.3.2 as a red line.

- At negative voltages ($U_{\mathrm{PBias}} \ll \phi_{\mathrm{pl}}$), all the ions around the probe are attracted. As a consequence, the ion current I_{PBias} saturates. This ion

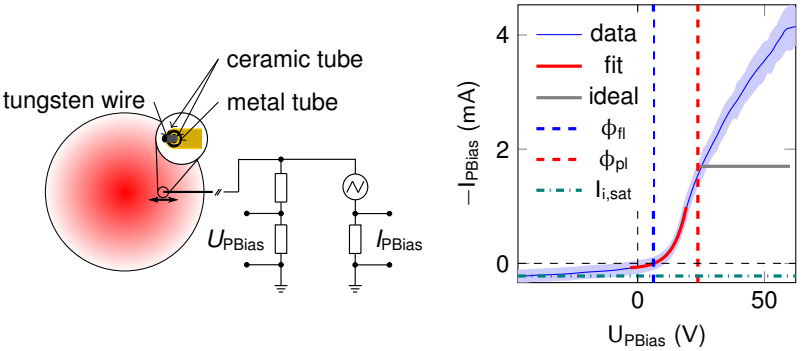

Figure 3.2: *(Left)* Scheme of the experimental setup and electric circuit of a swept Langmuir probe to obtain the $I(U)$) curve. *(Right)* The characteristic ($I(U)$) of the swept Langmuir probe. The temperature is obtained by an exponential fit, the density from the ion-saturation current and the temperature.

saturation current $I_{i,\mathrm{sat}}$ is proportional to the electron density n_e

$$I_{i,\mathrm{sat}} = 0.61 e n_\mathrm{e} S \sqrt{\frac{T_\mathrm{e}}{m_\mathrm{i}}} \tag{3.2}$$

where e is the elementary charge, S corresponds to the probe surface, T_e to the electron temperature and m_i to the ion mass [41]. However, the effective probe surface changes in the presence of a magnetic field $S(r) \propto B(r)^{-1}$ [92]. The gyration movement allows particles to reach the probe from a greater distance. This distance variation over the radius is reflected in the number of particles next to the probe. The current depends linearly on the gyration radius. Low magnetic fields result in large gyration radii and make a correction necessary. Finally the density relates as

$$n_\mathrm{e}(r) \propto \frac{I_{i,\mathrm{sat}}(r) B_0(r)}{\sqrt{T_\mathrm{e}(r)}} \ . \tag{3.3}$$

In this work, the shape of the right-hand side of eq.(3.3) is normalized on the line-averaged density obtained from the interferometer signal. This avoids the need to determine the absolute, effective probe surface.

It is possible to extract two operating points within the characteristic in order to obtain the density and the potential fluctuations. If the temperature fluctuations inside the confinement region are assumed to be small compared to the density fluctuations, the proportionality $\tilde{I}_{i,\mathrm{sat}} \propto \tilde{n}$ is valid. The operating point within the characteristic is at a constant voltage of $U_{\mathrm{PBias}} = -90\,\mathrm{V}$ inside the ion saturation region.

The other operating point is where the bias current vanishes ($I_{\mathrm{PBias}} = 0\,\mathrm{mA}$). Here, the measured potential is the floating potential ϕ_{fl}. An isolated electrode takes this voltage with respect to the vessel potential which is approximately equal to ground at TJ-K. The floating potential is always in the electron repelling region (blue dashed line in fig. 3.2) and therefore smaller than the plasma potential ($\phi_{\mathrm{fl}} < \phi_{\mathrm{pl}}$). The equation (3.1) $I_{\mathrm{PBias}}(\phi_{\mathrm{fl}}) = 0\,\mathrm{mA}$ results together with $I_{e,\mathrm{sat}} = -en_{\mathrm{e}}S\sqrt{T_{\mathrm{e}}(2\pi m_{\mathrm{e}})^{-1}}$ in

$$\phi_{\mathrm{fl}} = \phi_{\mathrm{pl}} + \frac{T_{\mathrm{e}}}{e}\ln\left[0.61\sqrt{2\pi\frac{m_{\mathrm{e}}}{m_{\mathrm{i}}}}\right] . \tag{3.4}$$

In eq. (3.4) the difference between plasma and floating potential is proportional to the electron temperature. In order to obtain the plasma potential fluctuations which are subject to this study, the approximation $\tilde{\phi}_{\mathrm{fl}} \approx \tilde{\phi}_{\mathrm{pl}}$ can be done because electron temperature fluctuations are small in TJ-K ($\tilde{T}_e \approx 0$) [84]. This simplifies the measurement because the probe acquiring the potential fluctuations does not need a sophisticated setup like the emissive probe obtaining the time-independent plasma potential.

3.1.2 Emissive probe

As mentioned in sec. 3.1.1, the plasma potential can be estimated from the higher limit of the exponential increase, the electron repelling region. A determination of the plasma potential can be done via the derivative of the characteristic, shown in fig. 3.3-*right*. From experience, the characteristic signal often begins to be noisy at these voltages and a calculation of ϕ_{pl} with this method turns out to be difficult.

The emissive probe is a diagnostic to measure the plasma potential directly. The probe head is a tungsten loop, whereas the lead in wires consist of copper because of its higher conductivity. The loop is heated externally with a heating current I_{heat}. At high heating currents, only the probe head of tungsten - with its lower conductivity - begins to glow and to emit electrons. Compared to the plasma potential, the potential of the probe-head is negative

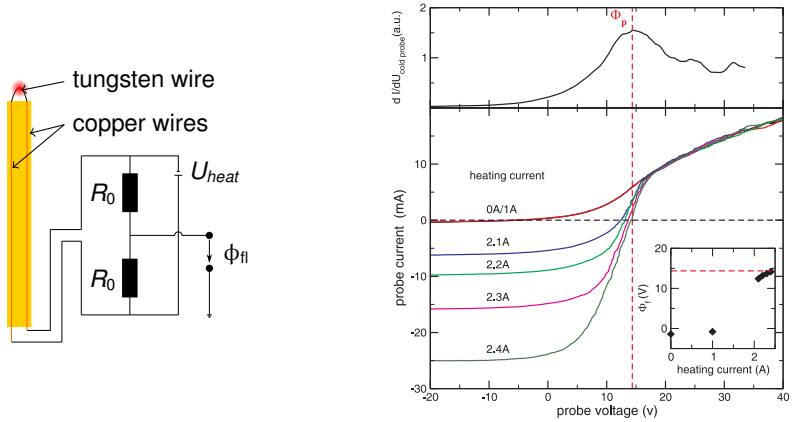

Figure 3.3: *(Left)* Scheme of the electric circuit of an emissive probe. *(Right)* The characteristics change with increasing heating current of an emissive probe and the floating potential shifts towards the plasma potential (from [84]).

for the electrons, and the electrons are repelled. This results in an emissive current which adds to the ion-saturation current [93]. This is shown in fig. 3.3-*right* where the characteristic curves are plotted for different heating currents [84]. For higher heating currents, the ion saturation currents take much higher absolute values than in the cold case. In the region $U_{\mathrm{PBias}} \gg \phi_{\mathrm{pl}}$ no electrons leave the probehead area anymore and no current the electron saturation region. For increasing emissive currents the characteristic becomes more and more symmetric. The change in the characteristics results in a shift of the floating potential ϕ_{fl} towards the plasma potential ϕ_{pl}. This shift of emissive probe-chars at different heating currents is shown in the inlay of fig. 3.3. For high heating currents the floating potential saturates and the approximation $\phi_{\mathrm{fl}} \approx \phi_{\mathrm{pl}}$ is valid.

The main disadvantage of emissive probes is their short durability. In the future, a coating of the tungsten wire with lanthanum hexaboride might be desirable. It has a much lower work function than tungsten which might increase the recovery factor of emitting electrons. This may result in a faster saturation of the floating potential at lower heating currents and thus in a longer lifetime.

3.1.3 Global array for Reynolds stress measurement

In this work, the diagnostic to measure density and potential fluctuations is the so-called "Global Array for Reynolds Stress Measurement" (GARM) [94]. The array consists of 128 Langmuir probes distributed on four different flux surfaces (fig. 3.4-*right*). As shown in fig. 3.4-*left*, the probes are perpendicular to the surfaces. The probes have been oriented towards the projections of the

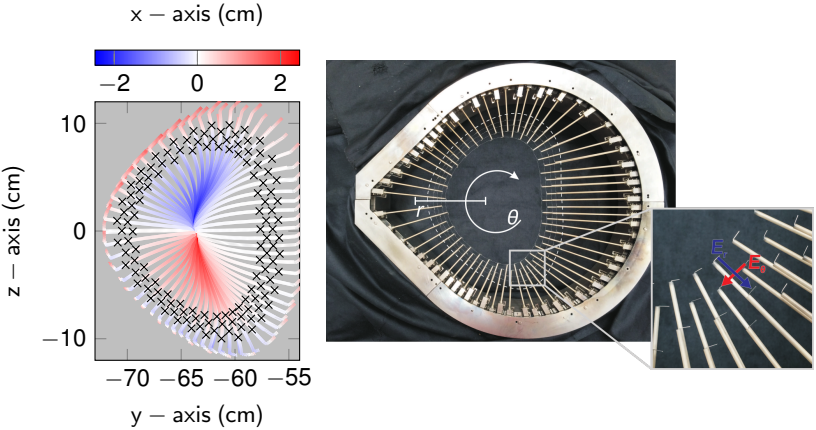

Figure 3.4: (*Left*) Scheme of probe positions at O2 Port. It shows that the probes are aligned to the normals. The kink of the normals in the outer region defines the position of the last closed flux surface because the normal tracing fails outside the confinement region. Here, no closed flux surface can be defined and therefore no valid normals can be calculated. (*Right*) Photo of the GARM array taken from [58]. The inlay shows principles of how the radial and poloidal electric fields are calculated from difference quotients of the potential measured by the pins.

flux surface normals (not radially towards the plasma center) and arranged according to the projections of the geodesic coordinates [58]. The probes can either be set on floating potential mode (for potential fluctuations $\tilde{\phi}_{\mathrm{fl}} \approx \tilde{\phi}_{\mathrm{pl}}$) or on ion saturation mode (for density fluctuations $\tilde{I}_{i,\mathrm{sat}} \propto \tilde{n}$) as described in sec.3.1.1. The fluctuations are acquired by the Genesis GEN16t transient recorder providing a time resolution of 1 MHz. The 128 channels usually acquire 2^{20} samples. This leads to a Nyquist-frequency of 500 MHz, enough to analyze the main features in the turbulent spectrum found mostly in frequencies below 100 kHz as previous investigations showed [95, 51, 54]. For

the calculation of the Reynolds stress the electric field fluctuations in normal projection direction and geodesic projection plane are calculated from the difference quotients of the potential fluctuations similar to [59]

$$\tilde{E}_{pn} = -\frac{\tilde{\phi}_{\text{fl}\,k(\theta)+1} - \tilde{\phi}_{\text{fl}\,k(\theta)}}{\Delta d_{pg}} \tag{3.5}$$

$$\tilde{E}_{pg} = -\frac{\tilde{\phi}_{\text{fl}\,i(\text{FS})+2} - \tilde{\phi}_{\text{fl}\,i(\text{FS})}}{\Delta d_{pn}} \ . \tag{3.6}$$

From the fluctuation in the potential the velocities can be calculated as

$$\tilde{v}_{pn} \approx \tilde{E}_{pg}/B_{pp} \qquad \tilde{v}_{pg} \approx -\tilde{E}_{pn}/B_{pp} \ . \tag{3.7}$$

Here, B_{pp} is the magnetic field component perpendicular to the poloidal cross-section. With the velocity fluctuations calculated by eq. (3.7), the Reynolds stress ($R = \langle \tilde{v}_{pn}\tilde{v}_{pg}\rangle_T$) can be calculated for two different flux surfaces poloidally resolved.

3.2 Biasing

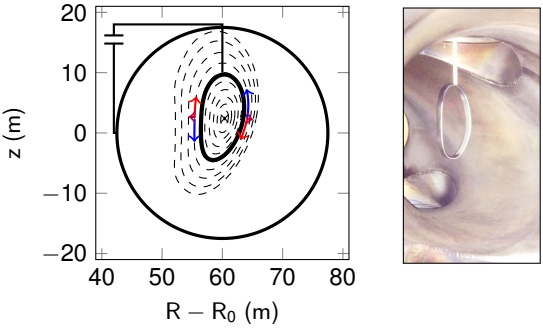

Figure 3.5: *(Left)* Scheme of the flux surface align electrode. *(Right)* A photo of the ring electrode already positioned in the vessel without plasma.

In this work, changes in plasma parameters in TJ-K are enabled by a ring-shaped electrode placed in the confinement region [95] as shown in fig. 3.5. A positive potential between the ring electrode and the limiters is set where

the limiters are galvanically connected with the vessel wall. This excludes biasing effects at the LCFS. The $E \times B$-rotation is generated as follows: the inhomogeneous magnetic field causes a loss of the parallel velocity component on the low field side due to thermalization. The missing contributions can no longer be converted into the perpendicular velocity component on the high field side. This effectively leads to perpendicular frictional forces resulting in a $\boldsymbol{F} \times \boldsymbol{B}$ drift to the outside [96]. Since this drift is mass-dependent, the ions are more affected than the electrons, which in turn leads to an outside return current. A stationary, ambipolar electric field is formed leading to an enhancement of the background $E \times B$-rotation [95].

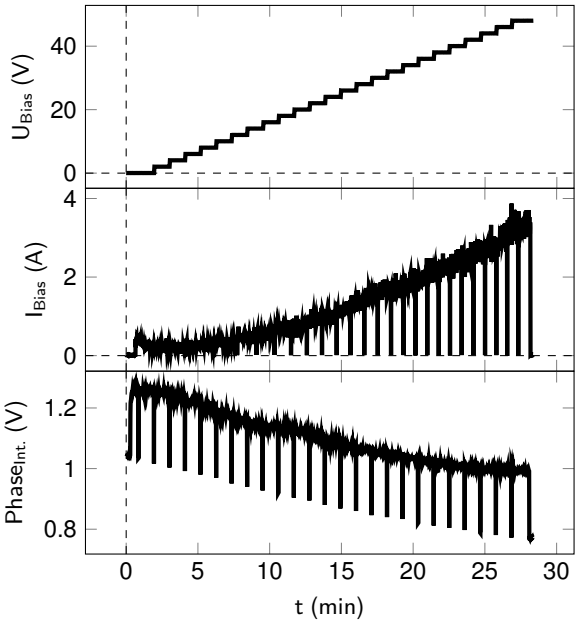

Figure 3.6: *(Top)* Time trace of the bias voltage applied between electrode and vessel wall. The bias voltage is increased step-wise with a constant phase ($\Delta t \approx 45\,\mathrm{s}$). *(Middle)* The bias current increases with higher bias voltages as well. *(Bottom)* The interferometer signal over time. Short off-states of the plasma ensure the needed offset equalization.

As fig. 3.6-*top* shows, the bias voltage is increased step-wise with a phase

duration of around one minute. Within these phases the carrier with the emissive probe and the swept Langmuir probe is moving and radial profiles of the equilibrium parameters are obtained from inside to outside. A smaller radial step-size ($\Delta r = 0.0033\,\mathrm{m}$) compared to previous studies ($0.01\,\mathrm{m}$ [58]) is needed in order to calculate reliable derivatives (up to second order) of the potential to obtain the shearing rate (see later sec. 5.2). This slows down the measurement process and takes around $\Delta t \approx 45\,\mathrm{s}$ for one profile because each measurement at each of the 28 points takes one second and the movement to the measurement points takes time, too. The profile measurement ends outside the confinement region and the measurement of the floating potential fluctuations by the GARM is done subsequently. After this, the bias voltage is increased. With increasing bias voltage the current increases, too (fig. 3.6-*middle*). Previous studies [95, 97] already showed that negative bias voltages result in low currents because they are limited by ion saturation explained in Langmuir probe theory (sec. 3.1.1). The small jumps to $I_{\mathrm{Bias}} = 0\,\mathrm{A}$ at the end of each phase are caused by a controlled off-state of the heating system ($\Delta t = 1\,\mathrm{s}$). This is necessary in order to obtain the line-averaged density from the interferometer phase-signal (fig. 3.6-*bottom*) which needs an offset adjustment compared to the off-state [92, 98]. This offset experiences a temperature shift caused by the hot coils. A typical discharge takes about 28 min and is limited by the permitted maximum temperature of the coils. A new remote system was set up allowing to pre-program the control of the diagnostics as well as the control of the plasma of the individual phases. So up to 25 subsequent biasing phases can be applied.

Chapter 4

Data analysis and methods

In preparation for the analysis of the experimental data, this chapter shortly sketches important analysis techniques. First statistical moments are introduced sec. (4.1). Then, the advanced, conditional averaging technique is described in sec. 4.2. In the sec. 4.3 useful Fourier methods are discussed, including the average phase and the bicoherence.

4.1 First order Statistics

The GARM array (sec. 3.1.3) allows measuring the floating potential on one flux surface in poloidal space and time. Such a data-set can be stored in a two-dimensional array

$$x_{j,l} = \phi_{\mathrm{fl}}(t, \theta) \tag{4.1}$$

where the index j counts the single datapoints in time and l the ones in poloidal space. The condition $\tilde{\phi}_{\mathrm{pl}} \approx \tilde{\phi}_{\mathrm{fl}}$ only applies to temporal fluctuations and the temporal mean

$$\bar{\phi}_{\mathrm{fl}}(\theta) = \bar{x}_l = \frac{1}{N_j} \sum_j x_{j,l} \ , \tag{4.2}$$

with N_i the total number of time points, must be removed from the data-set resulting in the potential fluctuations

$$\tilde{\phi}_{\mathrm{fl}}(t, \theta) = \tilde{x}_{j,l} = x_{j,l} - \bar{x}_l \ . \tag{4.3}$$

ZF are defined to be constant on a flux surface and therefore constant over the poloidal angle. In preparation for the analysis of ZF-dynamics the

potential fluctuations are poloidally averaged

$$\phi_{\mathrm{ZF}}(t) = \tilde{x}_j = \frac{1}{N_l} \sum_l \tilde{x}_{j,l} \tag{4.4}$$

which reduces the data-set to only one time-dependent signal. The average of a single signal is also called the first moment (μ_1) of descriptive statistics. The second moment is the variance and, in the case of the ZF signal, can be written as

$$\mu_2 = \frac{1}{N_j} \sum_j (x_j - \mu_0)^2 = \sigma^2 \tag{4.5}$$

where μ_1 is the time average of the zonal potential fluctuations which can be considered zero in this specific case because the temporal mean was subtracted before. The variance is the squared standard deviation σ.

4.2 Conditional average

In TJ-K, the dynamics of the time-dependent zonal flows are analyzed with the help of the conditional average technique [51, 99, 100]. As the name states, only time series are taken which satisfy certain conditions. In the case of the ZFs, time intervals are taken with zonal amplitudes higher than 2σ as shown in fig. 4.1-*top*. This ensures that only intervals are analyzed where the amplitude of the ZF is comparably high. Fig. 4.1-*bottom-left* shows how selected intervals develop a common behavior around the trigger time point. This trend is extracted by the average over all realizations and is shown in fig. 4.1-*bottom-right*, the conditional averaged zonal potential.

Since the whole data-set is uniquely indexed, different, pre-calculated quantities, as e.g. the Reynolds stress, can be conditional averaged and analyzed with respect to the selected ZF amplitudes.

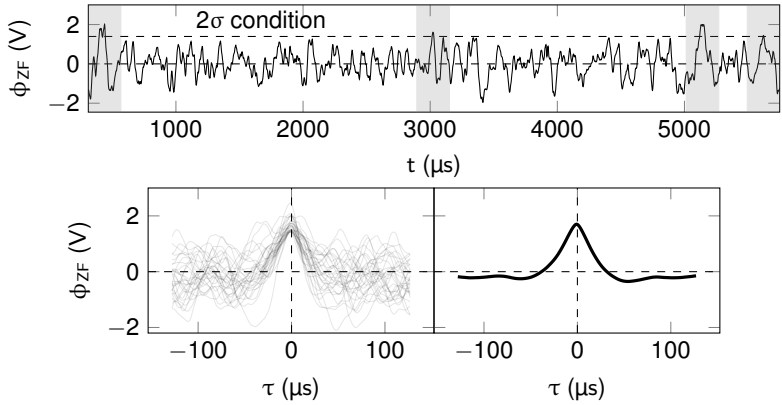

Figure 4.1: (*Top*) Time intervals are exemplary marked in gray and taken out of a signal where the signals satisfy a certain condition (higher than 2σ). (*Bottom-left*) Selected intervals develop a common behavior around the trigger time point. (*Bottom-right*) An average over all intervals gives the conditional averaged signal.

4.3 Fourier analysis

Fourier techniques are used to resolve the potential fluctuations in wavenumber- and frequency space. They are further useful to extract three-wave interaction by comparing the phase contributions in Fourier space. This section only sketches the Fourier techniques used in this work. A more detailed introduction gives Hinich/Clay [101] and extensive proofs can be found in the script of Gavin [102]. In preparation of the power-spectrum or bicoherence of the spectrum, the data-set of the potential fluctuations is Fourier transformed as

$$\hat{x}(k,\omega) = \mathcal{F}_F\left[x_{j,l}\right] = \frac{1}{N_{j,l}} \sum_{j,l} x_{j,l} \mathrm{e}^{i\left(k_n \theta_l - \omega_m t_j\right)} \tag{4.6}$$

$$x(r\theta,t) = \mathcal{F}_B\left[\hat{x}_{n,m}\right] = \frac{1}{N_{n,m}} \sum_{n,m} \hat{x}_{n,m} \mathrm{e}^{-i\left(k_n r\theta_l - \omega_m t_j\right)} \ . \tag{4.7}$$

Here, $r\theta_l$ is the discrete poloidal coordinate, r being considered constant. ω is the angular frequency and k the wavenumber. n, m index the discrete wavenumbers and frequencies.

4.3.1 Spectra

(Auto)-Powerspectrum In this work, the power of the ZF is compared with other spectral contributions. An auto-powerspectrum can be calculated by

$$P_{x,x}(\omega_m, \theta_l) = \langle \hat{x}^*(\omega_m, \theta_l)\hat{x}(\omega_m, \theta_l)\rangle_E \tag{4.8}$$

where the asterisk denotes the complex conjugate. In addition, an average $\langle\cdot\rangle_E$ over an ensemble of time-intervals is applied evenly taken out of the total signal similar to the conditional average but without a specific condition. The spectrum determines the way the power in the fluctuating signal is distributed on the different frequencies and wavenumbers. Parseval's theorem says that the averaged powerspectrum is equal to the variance of a mean-free signal.

$$\frac{1}{N_m}\sum_m P_{x,x}(\omega_m, \theta) = \frac{1}{N_i}\sum_i x_{i,j} = \mu_1(\theta) = \sigma^2(\theta) \tag{4.9}$$

For two dimensions a $kf-$ spectrum can be calculated

$$P_{x,x}(\omega_m, k_n) = \langle \hat{x}^*(\omega_m, k_n)\hat{x}(\omega_m, k_n)\rangle_E \ . \tag{4.10}$$

Correlation-function In order to determine important properties of the average turbulent structure such as its life-time with growth and decay, correlation functions are introduced. The auto-correlation-function ($C_{x,x}$) compares a signal with itself, but with an arbitrary shifted time τ. It is normalized such that it can only take values between $[-1, 1]$ and is one at zero time-lag $C_{x,x}(\tau = 0) = 1$. In terms of Fourier transformations the correlation-function can be expressed by the back-transformation from the auto-powerspectrum

$$C_{x,x}(\tau, r\theta_l) = \mathcal{F}_B\left[\hat{x}^*_{l,m}\hat{x}_{l,m}\right] \tag{4.11}$$

The maximum around $\tau \approx 0$ can be approximated by a Gaussian ($C \propto \exp(-\tau^2/\tau_c^2)$) which gives the correlation time τ_c. The method of the correlation-function is extended to obtain spatial information about the turbulent structure. Therefore, the reference signal ($x = x_{l,m}$) is shifted in the poloidal space ($r\Delta\theta_l$) which means that it is compared with other signals ($x_{o,m}$) measured on different positions ($l \neq o$). The cross-correlation-function

yields

$$C_{x_1,x_2}(\tau, r\Delta\theta_o) = \mathcal{F}_B\left[\hat{x}^*_{l,m}\hat{x}_{o,m}\right] \tag{4.12}$$

Cross-powerspectrum A comparison of two different signals is not necessarily restricted to the space-time domain. Even different quantities such as the radial and poloidal velocity fluctuations calculated at the same position can be compared. Besides the cross-correlation-function, a cross-powerspectrum can be applied resolving the information in the wavenumber- and frequency space. An estimation of the cross-powerspectrum is

$$P_{x,y}(\omega_m, k_n) = \hat{x}^*(\omega_m, k_n)\hat{y}(\omega_m, k_n) = h_{x,y}(\omega_m, k_n)\cos(\alpha(\omega_m, k_n)) \tag{4.13}$$

where $h_{x,y} = \Re(P_{x,y})$ is the cross-amplitude and α the cross-phase.

Average cross-phase The cross-power-spectrum of the radial and poloidal velocity fluctuations is equal to the Reynolds stress and the cross-phase is suggested to give information about the tilt of the turbulent structures. In this work, only an average cross-phase is of interest without the spectral information. The average cross-phase can be approximated from the cross-correlation-function at zero time lag ($\tau = 0$) [60]

$$\cos(\alpha) = \frac{C(\tau = 0)}{\sigma_{x,x}\sigma_{y,y}} \ . \tag{4.14}$$

4.3.2 Wavelet transformation

The theory of the manifold-shrinking (see sec. 2.7.3) suggests a change in the coupling behavior in Fourier space of the potential fluctuation over time. To investigate this theory time-dependent Fourier coefficients are obtained by wavelet transformation. Each frequency is scanned by wavelets which have the property that their temporal width depends on the variable (a), called scale. The scales are related to the frequency as $\omega = (2\pi + \sqrt{2 + 4\pi^2})/2a$. The dependency of the temporal width of a wavelet on the frequency ensures that the length analyzed time segment falls in the current frequency range which is scanned by the wavelet [103]. In this work the Morlet-wavelet is

chosen which is defined as

$$\Psi_a = \frac{1}{\sqrt{a}}\pi^{-0.25}\exp\left[i\frac{2\pi t}{a} - \frac{1}{2}\left(\frac{t}{a}\right)^2\right] . \tag{4.15}$$

In the case of the potential fluctuations, the Fourier-transformed two-dimensional data-set ($\hat{x}(\omega, k)$) is convoluted with the Morlet-wavelet as

$$\mathcal{W}(\omega, k, t) = \sum_{\omega} \hat{x}(\omega, k)\Psi_a(\omega, t)\mathrm{e}^{i\omega t} . \tag{4.16}$$

The result is a three-dimensional array. One dimension is the time, whereas the others are the frequency and the wavenumber domain. Now, the temporal behavior of the single modes can be analyzed over time.

4.3.3 Bispectrum

The drift-wave model suggests nonlinear interaction of the waves. A method to analyze three-wave coupling is the auto-bicoherence consisting first of a bispectrum formed as

$$B(k_1, k_2) = \langle\hat{\phi}(k_1)\hat{\phi}(k_2)\hat{\phi}^*(k_3)\rangle . \tag{4.17}$$

Hereby, the different spectral contributions of the potential fluctuations are compared. The bispectrum gives contributions only if all three wave vectors are phase-locked coupled. In the case of randomly distributed phases the bispectrum vanishes ($B = 0$). If the condition $k_1 + k_2 = k_3$ is satisfied, maximum possible values for the bispectrum emerge. The bispectrum is able to detect three-wave interaction but does not provide information about the significance of the wave-coupling. A measure of the phase coherence is provided if the bispectrum is normalized to the so-called bicoherency.

$$b(k_1, k_2) = \frac{\langle\hat{\phi}(k_1)\hat{\phi}(k_2)\hat{\phi}^*(k_3)\rangle}{\langle|\hat{\phi}(k_1)\hat{\phi}(k_2)|^2\rangle\langle|\hat{\phi}(k_3)|^2\rangle} . \tag{4.18}$$

It can be shown by the Cauchy-Schwartz inequality that the bicoherence is limited between $0 \leq b \leq 1$. Here, a value of zero indicates stochastic phase relations, while a value near one implies strong phase coherence. The significance level can be estimated as $s = 1/\sqrt{N}$ where N is the number of ensembles for the average [105, 106]. Further, the bicoherence domain which is restricted within the Nyquist-wavenumbers k_{Ny} has the following

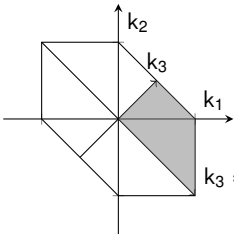

Figure 4.2: Limitation of the wavenumber space for the bicoherence due to the Nyquist frequency. Symmetry properties of the wavenumber domain for the bicoherence as in eq. (4.20) reduce the non-redundant part to the grey area (adapted from [104]).

symmetry axes and properties [104]

$$k_1 - k_2 = 0 \qquad k_1 + k_2 = 0 \ , \tag{4.19}$$

$$b^2(k_1, k_2) = b^2(k_2, k_1) = b^2(-k_1, -k_2) \tag{4.20}$$

indicated in fig. 4.2.

4.4 Elliptical model

To determine the life time and size of turbulent structures, usually the Taylor hypothesis is used [107]. It states that the fluctuations are independent of a constant background velocity (v) and the time can be expressed as $t = x/v$ (with x as spatial coordinate) which labels the turbulence as "frozen turbulence". A turbulent structure of half size l_d is moving on a background flow v leading to a cross-correlation function in space (ϵ) and time (τ) as in fig. 4.3-*left* and for the 1/e-contour line follows $\epsilon(\tau) = v\tau \pm l_d$ (red lines). Nevertheless, turbulent structures first have to evolve and then will decay again. Therefore the model is expanded to the elliptical model first proposed by Briggs [108], theoretically examined by Zhao [109] and in fusion science already applied in Doppler-reflectometry [110, 111]. For the new model, the cross-correlationfunction can be estimated as

$$C(\epsilon, \tau) = \exp\left[-\left(\frac{\tau^2}{\tau_c^2} + \frac{(\epsilon - v\tau)^2}{l_d^2}\right)\right] \ . \tag{4.21}$$

For $C = 1/e$ the cross-correlation function shows a tilted ellipse as demon-

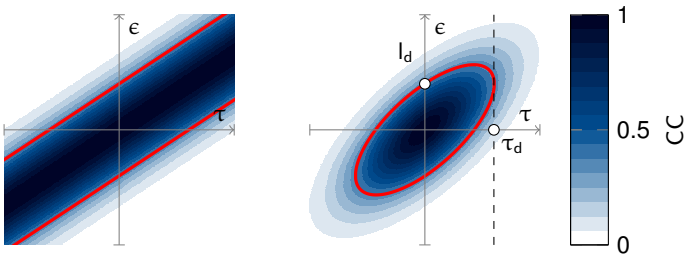

Figure 4.3: (*Left*) The cross-correlation function modeled by the Taylor-hypothesis. (*Right*) The elliptical model as an expanded Taylor-hypothesis by including the evolution and decay of turbulent structures.

strated in fig. 4.3-*right* (red). At $\tau = 0$ the cross-correlation function reduces to a simple Gaussian function corresponding to a cut in the 2D function, and the correlation length l_d can be obtained by a fit. In order to determine τ_c, the maximum value of τ has to be obtained from the $1/e$-contour ellipse. Another approach is to perform a fit to the envelope of the cross-correlation functions for different space shifts ϵ in the time domain. In contrast to the original "frozen turbulence" model of Taylor, a cut at $\epsilon = 0$ is not sufficient to reveal the correlation time τ_d. The elliptical model is far from being complete [111]. Therefore a few remarks are given on possible causes that may lead to a difference between model and experiment. First, the elliptical model only includes one dimension in space and should be expanded for 2D turbulence. Recent results further imply that the shearing coordinates ($v'\tau_L\epsilon_1$-cf. sec. 2.5) have to be introduced [111]. This leads to

$$C(\epsilon_1, \epsilon_2, \tau) = \exp\left[-\left(\frac{\tau^2}{\tau_c^2} + \frac{\epsilon_1^2}{l_1^2} + \frac{(\epsilon_2 - v\tau - v'\tau_L\epsilon_1)^2}{l_2^2}\right)\right] , \qquad (4.22)$$

with ϵ_1, ϵ_2 as the spatial shifts and their correlation lengths l_1, l_2. Eq. (4.22) describes an ellipsoid as shown in fig. 4.4. From selected sections of the ellipsoid, the required quantities can be extracted. For a $\epsilon_1 = 0$ cut the original elliptical model (eq. 4.21) is regained and the correlation time as well as the l_2 length can be obtained. A cut of the ellipsoid at $\tau = 0$ is necessary to get information about the shearing part $a = v'\tau_c$. In contrast to the shear-free case (dashed contours), a non-zero shear results in a tilt of the ellipse shown in fig. 4.4-*right* right discussed in [111]. The slope of

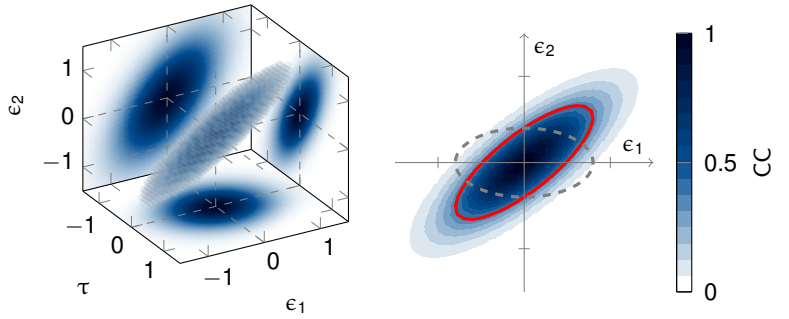

Figure 4.4: (*Left*) The ellipsoid described by eq. (4.22) models the cross-correlation function around its maximum including the radial and poloidal space domain as well as the shearing coordinates. The shadows correspond to re-normalized CCFs integrated over the respective spatial direction. (*Right*) A section of the ellipsoid at $\tau = 0$ reveals a tilted ellipse. The tilt can be deduced to the implemented shear as the ellipse is not tilted in the shear-free case (dashed).

the ellipses' main axis is not equal to the parameter a which requires a more sophisticated method, e.g. regression. In order to obtain the correlation length l_1 it is useful to take the ϵ_1 intersect at $C = 1/e$ of the ϵ_2-integrated ellipse. This ellipse corresponds to the "shadow" of the ellipsoid as indicated in fig. 4.4-*right*.

Another disadvantage of all proposed models is that they do not differentiate between a growth or decay time, which can be tackled by treating positive ($\tau > 0$) and negative time shifts ($\tau < 0$) separately. The two different Gaussian fits around the maximum result in a growth time and decay/decorrelation time (τ_g, τ_d). The life-time of the structure is composed of $\tau_L = \tau_g + \tau_d$.

Chapter 5

Equilibrium and shear

As soon as currents are drawn from the plasma by the biasing electrode, a new equilibrium state is achieved with changes in the plasma potential and in the temperature profiles. This has an impact on turbulence through changes in e.g. the collisionality and the density gradient. Changes in the equilibrium profiles of TJ-K plasmas induced by electrode biasing are documented here. Moreover, the equilibrium of background shear is analyzed and compared to turbulence growth rates.

5.1 Influence of the plasma biasing on equilibrium profiles

The plasma pressure is governed by the electrons, $p \approx p_e = n_e T_e$, since the ion temperature is low compared to the electron temperature of the plasmas in TJ-K ($T_i \ll T_e$) [**mahdizadeh2004**]. The gradient of the pressure determines the diamagnetic drift and therefore the growth and propagation of drift waves. The profiles are obtained by a radially moving Langmuir probe as described in sec. 3.1.1. In fig. 5.1-*top*, the density profiles are shown for different bias voltages applied to the electrode. The center of the plasma is at $R - R_0 = 0.04\,\mathrm{m}$, the flux surface of the electrode is at $R - R_0 = 0.085\,\mathrm{m}$, the flux surfaces of the array are in the range of $R - R_0 = 0.10\,\mathrm{m} - 0.115\,\mathrm{m}$ and the LCFS defined by limiter plates is at $R - R_0 = 0.1228\,\mathrm{m}$ [58, 57]. Qualitatively the maximum values in the center of the confinement region slightly increase with higher bias voltages. For highest voltages, it is not possible to obtain the density within the region included by the electrode because the Langmuir probes caused a plasma break-down in this region. The electron temperature shows higher values at the edge of the confinement region (fig. 5.1-*center*). Here the heating position, i.e. the upper hybrid resonance, is assumed [92]. T_e shows a slight increase mostly located at the edge of the confinement region for bias voltages below $U_{\mathrm{Bias}} \approx 50\,\mathrm{V}$. The resulting pressure profile is shown in fig. 5.1-*bottom*. At low bias voltages,

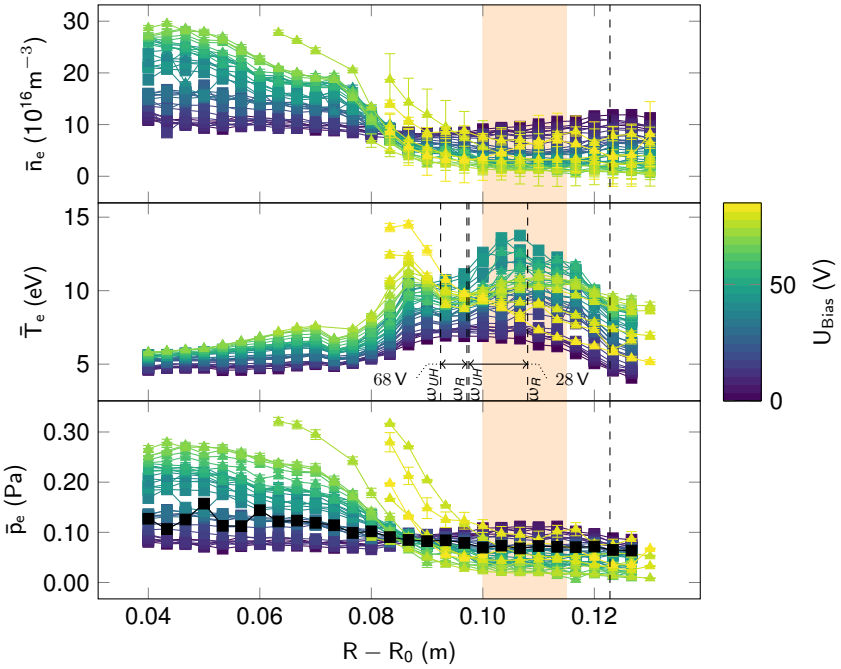

Figure 5.1: Radial profiles of the density, the temperature and the pressure for different bias voltages (color) in a H discharge (#12334, 12336). It shows that a centrally peaked pressure profile is beginning to evolve for $U_{\mathrm{Bias}} \approx 25\,\mathrm{V}$. The density gradient qualitatively steepens with higher bias voltage.

there is a hollow density profile and in consequence a hollow pressure profile due to the high nominal neutral gas pressure $p_0 = 9\,\mathrm{mPa}$ which is supposed to change the collisional processes [112]. Nevertheless, this pressure was used for stable conditions in plasmas at TJ-K with limiters placed therein. For increasing bias voltage, a peaked profile develops. This evolution is completed at a bias voltage of $U_{\mathrm{Bias}} = 26\,\mathrm{V}$. For this specific bias voltage the pressure profile, marked by black squares in fig. 5.1-*bottom*, implies that bias voltages higher than $U_{\mathrm{Bias}} = 25\,\mathrm{V}$ definitely exhibit a centrally peaked profile.

The increase of the pressure gradient at constant flux is an indicator of a transport barrier and an improved confinement [12]. The higher pressure

gradient has its origin in the increase of temperature and density in the center. Changes in the density profile cause a shift in the heating position at the upper-hybrid frequency (ω_{UH}) as well as the right-hand cutoff ω_{R} to the plasma center [92]. At the same time the tunneling distance of the incoming microwave between cutoff and heating position decreases, so that the heating becomes more efficient at higher voltages. These two effects lead to an increase of the temperature in the center of the plasma. Therefore, the particle sources related to ionization [113] inside the biased flux surface are expected to increase significantly. This results in reduced particle confinement times (τ_P) as estimated similarily to [95] ($\tau_P \propto N_{\mathrm{Ion}}^{-1}$).

Besides the curvature [114, 115], the collisionality is an important parameter controlling the coupling between potential and density fluctuations as seen from the Hasegawa-Wakatani equations [116]. The higher the collisionality (i.e. the lower the adiabaticity), the lower is the coupling. It could already been shown that indeed a change of the collisionality influences the energy transfer into the zonal flows and therefore changes the power distribution in the spectrum [51]. So it is important to investigate the behavior of the collisionality with biasing. Following [116, 51] the collisionality C^* depends as

$$C^* = \frac{\hat{\nu}}{k_\parallel^2} = \frac{B n_e}{k_\parallel^2 m_i T_e^{5/2}} \propto \frac{n_e}{T_e^{2.5}} = C \tag{5.1}$$

on the equilibrium parameters. Here B is the magnetic field strength, n_e the density, $k_\parallel$ the parallel wavenumber, m_i the ion mass and T_e the electron temperature. The parameter C covering the main dependencies of the collisionality is calculated from the temperature and density at the position of the array. The collisionality, shown in fig. 5.2-*top*, changes in the region of low bias voltages as the equilibrium profiles already suggested (fig. 5.1). As a consequence, these data-sets are excluded from the investigation of the $E\times B$-shear influence on the drift-wave turbulence and zonal flow generation in order to rule out adulterant correlations on the parameter C. The density gradient length influences the properties of drift-wave turbulence. For specific turbulence scaling studies the density gradient scale length is desired to be constant. In this work the gradient scale length is estimated by a fit of the density profile as $n(r) \approx \exp\left[-(r-r_0)^2/L_n^2\right]$ with $r_0 = 0.04\,\mathrm{m}$ as the plasma center. It enters a nearly constant regime at $U_{\mathrm{Bias}} = 20\,\mathrm{V}$, as shown fig. 5.2-*bottom*.

The equilibrium was investigated with reference to the pressure profile, the

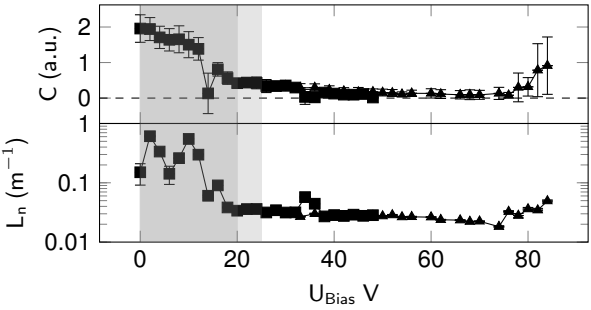

Figure 5.2: The collisionality (at the GARM position) and the density-gradient scale length plotted against the bias voltage. In the regime of lower bias-voltages (dark grey), both parameters appear to develop until $U_{\mathrm{Bias}} = 20\,\mathrm{V}$. The light grey area indicates the excluded data-sets in consequence of changes in the pressure profile (#12334,#12336).

collisionality and the density gradient length. While the collisionality and density gradient length enter a constant regime at a bias voltage $U_{\mathrm{Bias}} \approx 20\,\mathrm{V}$, the evolution of the pressure profile can be regarded as completed at a bias voltage of $U_{\mathrm{Bias}} = 25\,\mathrm{V}$. Therefore, only the data-sets of $U_{\mathrm{Bias}} \geq 25\,\mathrm{V}$ will be taken for analysis in the following sections.

5.2 $E\times B$ shear

For the calculation of the $E\times B$-shearing rate, the radial electric field has first to be derived from the plasma potential. Therefore the plasma potential is obtained from a radially moving emissive probe as described in sec. 3.1.2. The radial profiles for different bias voltages are shown in fig. 5.3. With increasing bias voltage, the plasma potential at the center raises strongly. The currents drawn result in a local enhancement of the radial electric field ($\boldsymbol{E}$=-$\boldsymbol{\nabla}\phi$) in the range $R - R_0 = 0.075\,\mathrm{m} - 0.12\,\mathrm{m}$ while inside the biased flux surface the shape stays unchanged.

As the plasma potential is constant on a flux surface, the gradient points to the direction perpendicular to the surface, i.e. the normal direction ($\boldsymbol{E} = (E_n, 0, 0)$). Thus, the electric field has a component perpendicular to the poloidal cross-section where they are not directly oriented against the plasma centre but rather tangential to the curves shown in fig. 5.4-*left*. Furthermore, the distance between the flux surfaces changes poloidally. This

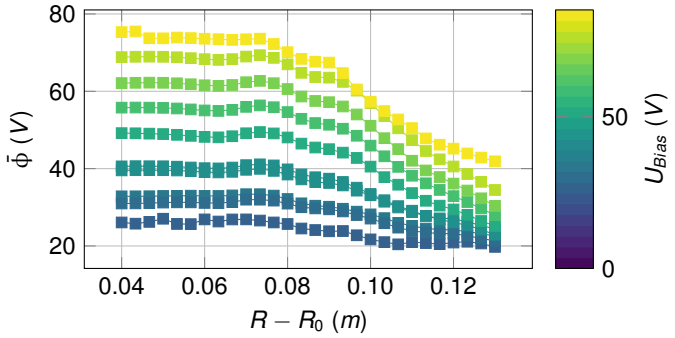

Figure 5.3: Radial profile of the plasma potential measured by an emissive probe for different bias voltages at Port O6. With increasing bias voltage the gradients in the potential steepen (#12334,#12336).

suggests that the electric field has a poloidal dependence ($E_n = E_n(\theta)$),too. Hence, for the $\boldsymbol{v}_{E\times B}$ flow field, the 3D potential distribution is needed which can principally be obtained from flux surface mapping of radial profiles as shown exemplarily in fig. 5.4-*right* for the $U_{\mathrm{Bias}} = 72\,\mathrm{V}$ bias case. Together with the metric of the magnetic field obtained from the MCC-code[1] [117], an $E\times B$-velocity can be calculated as

$$\boldsymbol{v}_{E\times B} = -\frac{\boldsymbol{\nabla}\phi \times \boldsymbol{B}}{B^2} = -\frac{\partial_s\phi(s)|\boldsymbol{\nabla}s|\overbrace{\frac{\boldsymbol{\nabla}s}{|\boldsymbol{\nabla}s|}}^{\hat{\boldsymbol{e}}_g} \times \hat{\boldsymbol{e}}_b\, B}{B^2}$$
$$= \overbrace{-\partial_s\phi(s)|\boldsymbol{\nabla}s|}^{E_n}\frac{1}{B}\hat{\boldsymbol{e}}_g = \frac{E_n}{B}\hat{\boldsymbol{e}}_g \tag{5.2}$$

with s as flux surface label. Note that the velocity vector is parallel to the geodesic vector, but not necessarily in the poloidal cross-section plane like the pins of the array. In order to compare the velocity with the turbulence measured by the array, the systems have to be identical. Therefore, the

[1] MCC: Magnetic Confinement Code, unpublished.

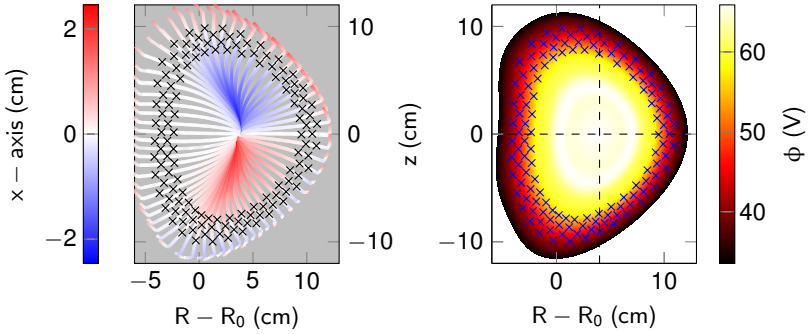

Figure 5.4: (*Left*) Traced paths of normals through pin positions (crosses) in the poloidal cross-section. The deviations from the poloidal plane are color coded. (*Right*) The radial profile of the plasma potential measured by the emissive probe mapped on the flux surface cross-sections which are calculated by the MCC-Code at Port O2 (Array position) (#12336,$U_{\mathrm{Bias}} = 72\,\mathrm{V}$).

velocity is projected into the cross-section

$$\boldsymbol{v}_{\mathrm{pg}} = (\boldsymbol{v}_{E\times B} \cdot \hat{\boldsymbol{e}}_{\boldsymbol{R}})\ \hat{\boldsymbol{e}}_{\boldsymbol{R}} + (\boldsymbol{v}_{E\times B} \cdot \hat{\boldsymbol{e}}_{\boldsymbol{z}})\ \hat{\boldsymbol{e}}_{\boldsymbol{z}} \tag{5.3}$$

$$\boldsymbol{n}_{\mathrm{pn}} = (\boldsymbol{\nabla} s \cdot \hat{\boldsymbol{e}}_{\boldsymbol{R}})\ \hat{\boldsymbol{e}}_{\boldsymbol{R}} + (\boldsymbol{\nabla} s \cdot \hat{\boldsymbol{e}}_{\boldsymbol{z}})\ \hat{\boldsymbol{e}}_{\boldsymbol{z}}\ . \tag{5.4}$$

Here, $\hat{\boldsymbol{e}}_{\boldsymbol{z}}$ is the vertical z-axis unit vector of the torus and $\hat{\boldsymbol{e}}_{\boldsymbol{R}}$ the unit vector of the major radius. The normal vector field ($\boldsymbol{\nabla} s$) is projected, too, in order to obtain effective path lengths for each pin in preparation for further derivation of the velocity along the projected normals ($\boldsymbol{n}_{\mathrm{pn}}$). Now, the $E\times B$-shearing rate can be calculated similarly to cylindrical fluid systems [118] as

$$\frac{\mathrm{d}v}{\mathrm{d}r} = \frac{\mathrm{d}(\omega r)}{\mathrm{d}r} = \omega + \underbrace{r\frac{\mathrm{d}\omega}{\mathrm{d}r}}_{\text{shear}}\ . \tag{5.5}$$

Here, only deviations from the angular frequency ($\omega = 2\pi f = v/r$) are referred to as shearing rate (the last part of eq. (5.5)). For the experiment TJ-K the shearing rate yields

$$\Omega_\theta = \frac{1}{2\pi} n_{\mathrm{pn}} \cdot \partial_{n_{\mathrm{pn}}} \left(\frac{\bar{v}_{\mathrm{pg}}}{n_{\mathrm{pn}}} \right)\ . \tag{5.6}$$

The poloidal profiles of the velocity as well as those of the shearing rate calculated from the same data-set as in fig. 5.4 are shown in fig. 5.5-*left* and *middle* respectively. Both vary with the poloidal angle which leads to a first indication that the tilt of turbulent eddies may poloidally change, too.

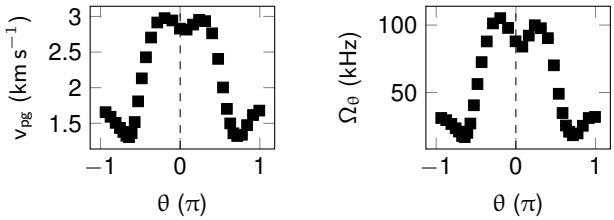

Figure 5.5: *(Left)* The geodesic velocity component projected on the cross-section plotted against the poloidal angle. *(Middle)* The poloidal profile of the shearing rate calculated from the projected velocity as in eq. (5.6). The variation in the polodial profiles is caused by the poloidally varying distance of the flux-surfaces (#12336,$U_{\mathrm{Bias}} = 72\,\mathrm{V}$).

In order to compare the shearing rate with the power in the zonal flow, a poloidal average is needed. Fig. 5.6 shows the averaged shear in dependence of the applied bias voltage ($\Omega = \langle\Omega_\theta\rangle_\theta$). Hereby only contributions under comparable equilibrium conditions for bias voltages greater than $U_{\mathrm{Bias}} \geq 23\,\mathrm{V}$ have been considered as argued with regard to the collisionality and the density gradient length in sec. 5.1. The error bars are the uncertainty in the mean by a min/max estimation in the poloidal profile. With increasing bias voltage the shear increases demonstrating that the shearing rate can be controlled externally by the biased ring-electrode.

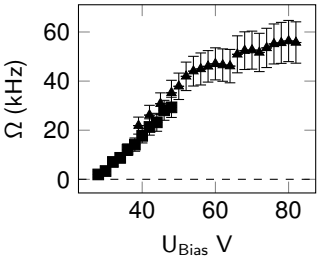

Figure 5.6: The shearing rate increasing with the bias voltage (#12334,#12336).

5.3 Growth rates

In order to classify the shear, a comparison with the growth rate of drift-wave turbulence is carried out in this section. The growth rates can experimentally be determined by the elliptical or ellipsoidal model (see sec. 4.4). Hereby, cross-correlation functions (CCFs) are calculated from the potential fluctuations measured with the poloidal probe array (cf. GARM in sec. 3.1.3). For one specific reference probe position the 2D cross-correlation function is shown in fig. 5.7. The 1/e contour level has roughly an elliptical shape. In preparation for the calculation of the growth time, the CCFs are projected in the time domain (fig. 5.7-*right*). Furthermore, the envelope of the CCFs at different poloidal shifts is extracted (thick line). A Gaussian fit of the envelope ($CC_{\text{fit}} = \exp\left[-\tau^2/\tau_g^2\right]$) for negative τ reveals the growth time τ_g.

The growth rate is calculated from the inverse of the growth time ($\gamma = \tau_g^{-1}$) and its poloidal profile is shown in fig. 5.8-*left*. The profile exhibits an asymmetry where higher growth rates are found at positive poloidal angles. Its maximum is near $\theta \approx 0.1\pi$. The asymmetry in the profile might be explained by the curvatures and the geometry of the magnetic field. The growth rate is calculated with the MCC-code [117] as indicated in eq. 2.81 [76] which incorporates normal and geodesic curvatures as well as integrated local

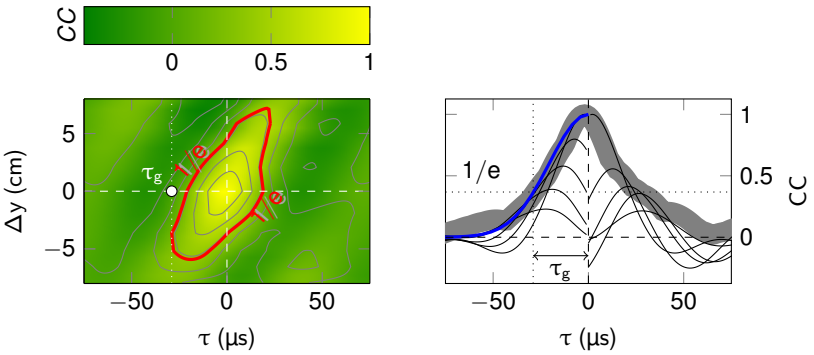

Figure 5.7: *(Left)* The cross-correlation function in two dimensional space with the poloidal shift Δy on the ordinate and the time shift τ on the abscissa. The red contour line implies the e^{-1}-level, which has roughly the shape of an ellipse. *(Right)* The growth time is obtained from the width of a Gaussian fit (blue for negative) on the envelope of the different cross-correlations over the negative time shift τ.

magnetic shear and is shown in fig. 5.8 as solid line. Even though the calculated growth rate does not account for the 3D eigenmode structure, the position of the maximum qualitatively agrees with the growth rate experimentally obtained which dynamically includes the full spectrum of drift waves. The red, hatched area highlights the poloidal section where the magnetic field configuration is expected to destabilize drift waves. Both, the experimental determined growth rate as well as the calculated one, exhibit their maximum value at around $\theta \approx 0.1\pi$ within the mentioned area.

In fig. 5.8-*right*, the poloidal profile of the turbulent transport from a previous study at TJ-K shows a quite similar behavior, especially the location of the turbulent transport is almost identical [119]. The drift-waves are destabilized by features of the magnetic field configuration such as geodesic and normal curvature as well as the integrated local magnetic shear which are theoretically incorporated in the estimation of maximum growth/damping rates of Nasim [76]. This is experimentally confirmed by the poloidal profile of the growth rate. The destabilization is the result of a phase shift between potential and density ($\alpha_{\phi,n}$) fluctuations and simultaneously leads to turbulent transport ($\Gamma \propto \sin \alpha_{\phi,n}$) [120, 54] as mentioned in sec. 2.7.4.

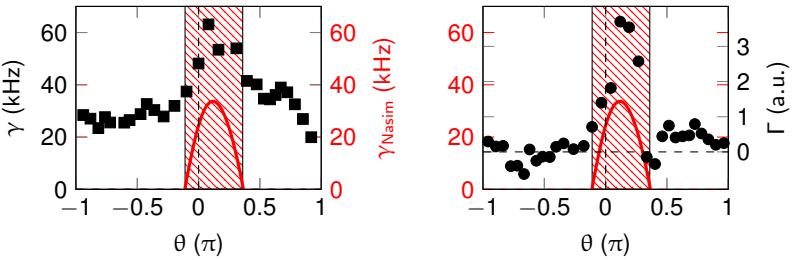

Figure 5.8: *(Left)* The poloidal profile of the growth rate calculated from the elliptical model (squares) applied to potential fluctuations . The solid line shows the maximum growth/damping rates calculated by [117] following [76]. Both profiles agree qualitatively well and have their maximum value at $\theta \approx 0.1\pi$. The shaded area indicates the poloidal range where the growth rate is positive. *(Right)* Poloidal profile of the turbulent transport as adapted from [119] in the same representation as (*left*).

5.4 Classification of shear

The shearing rate calculated in sec. 5.2 is now put in relation to the growth rate (γ). The ratio between the shearing rate and the growth rate is used as a rough criterion ($\zeta = \Omega/\gamma$) to distinguish different shear regimes [75]. If

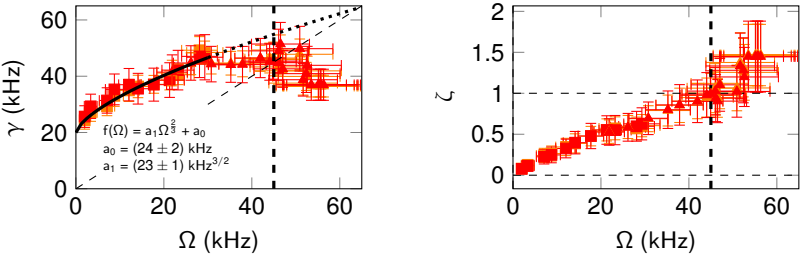

Figure 5.9: (*Left*) The growth rates of potential fluctuations plotted against the shearing rate. The dashed line shows $\gamma = \Omega$ and divides the plot in two areas. The upper-left corresponds to the weak shear regime, whereas the lower-right denotes the strong shear regime. After the transition at roughly $\Omega \approx 45\,\mathrm{kHz}$ the growth rate decreases, which might be a first indicator for decorrelation. (*Right*) The ratio between the shearing rate and the growth rate ($\zeta = \Omega/\gamma$), where a value of $\zeta = 1$ defines the transition criteria from the weak to the strong shear regime (#12334,#12336).

the shearing rate exceeds the growth rate (i.e. $\zeta > 1$), the shear distorts the turbulent structures faster than they can evolve. Larger structures are torn apart into smaller structures. As a consequence, strong turbulent amplitudes can not be generated anymore, one says the turbulence is suppressed. This is the common understanding of processes in the H-mode. Recent results suggest that the energy of turbulent small scale eddies is transferred to large scale structures due to the two-dimensional character of turbulence in a magnetically confined plasma [121, 95, 47, 35]. Nevertheless, in both cases the shearing exceeds the growth rate, which results in the reduction of the turbulent amplitudes. The regime with $\zeta > 1$ so-called strong shear regime. In contrast, $\zeta < 1$ defines the weak shear regime. The ratio is shown in fig. 5.9-*right*. The low shear regime is found between $\Omega = 0\,\mathrm{kHz} - 45\,\mathrm{kHz}$ and the strong shear regime starts at around $\Omega = 45\,\mathrm{kHz}$.

Fig. 5.9-*left* shows the growth rate plotted against the shearing rate. The dashed line implies the limit towards the strong shear regime $\gamma = \Omega$, the area in the upper left describing the weak and in the lower right the strong

shear regime. For the low shear regime the growth rate seems to scale with the shearing rate as expected from the BDT hypothesis $\gamma \propto \Omega^{2/3}$ derived in sec. 2.7.4. For the range $\Omega = 0\,\mathrm{kHz} - 30\,\mathrm{kHz}$, a fit ($f(\Omega) = a_1 \Omega^{\frac{2}{3}} + a_0$) is shown as a solid line. At a shearing rate of $\Omega \approx 30\,\mathrm{kHz}$, the growth rate starts to deviate noticeably from the BDT model and drops below the shearing rate at $\Omega \approx 45\,\mathrm{kHz}$. This might be explained by nonlinear effects as theoretically proposed by [35]. The result is a jump between two solutions for the growth rate at the shear transition. The drop of the growth rate to lower values might be explained by decorrelation and indicates the transition into a new shear regime.

5.5 Summary of equilibrium analysis

In preparation for more detailed turbulence analyses, important equilibrium quantities were examined for their dependence on different bias voltages. For scaling analyses of the shear effect on turbulence, the density gradient scale length and collisionality must not change significantly. In particular, the collisionality should be constant with regard to analyses of zonal flow enhancement because of the collisionality scaling of ZFs [51]. As mentioned before, all these considerations led to a conservative selection of data sets with bias voltages of $U_{\mathrm{Bias}} > 25\,\mathrm{V}$.

The stationary $E{\times}B$ shearing rate was obtained from the plasma potential measurement with the emissive probe. By including the metrics of the stellarator TJ-K and considering the rotational geometry, a shearing rate was calculated according to [122]. It was shown that the $E{\times}B$ shearing rate can well be controlled by external biasing.

For a classification of different shear regimes a comparison with the growth rate is necessary [75]. To this end, the growth rate was calculated from the elliptical model. Poloidal profiles showed a good agreement with the local drift-wave destabilization capability of the confining magnetic field structure as calculated according to theoretical approaches in [76]. The growth rate arises from a phase shift between density and potential perturbations which enables turbulent transport [60, 120]. In addition, the poloidal profile of the growth rate and the profile of the turbulent transport from previous studies [119] are found to be consistent.

At last the growth rate and the shearing rate were compared in order to identify different shear regimes [75]. The low shear regime is defined by the ratio of shearing rate to growth rate being lower than one and the strong shear

regime by the shearing rate exceeding the growth rate. The limit between both shear regimes, where the ratio is one, is found to be at $\Omega \approx 45\,\mathrm{kHz}$. Here the growth rate equals the shearing rate. Further, the relation between growth rate and shearing rate $\gamma \propto \Omega^{2/3}$, proposed by Biglary-Diamond-Terry [77], was confirmed in the range of $\Omega = 0\,\mathrm{kHz} - 30\,\mathrm{kHz}$.

Chapter 6

Background tilt and Reynolds stress

After the description of how the background shearing rate is determined in TJ-K (chap. 5) the influence of the background shear rate on the Reynolds stress and the tilt of turbulent structures will be discussed. In this chapter, the influences on the time-independent Reynolds stress, i.e. on its poloidal profile, and the average cross-phase between the radial and the poloidal velocity fluctuations are investigated: local cross-phases are compared with work angles and actual tilt angles. The observed eddy tilts are discussed with respect to magnetic shear and background $E \times B$ shear as well as with respect to the time-independent Reynolds stress.

6.1 Time-independent Reynolds stress and the tilt of turbulent structures.

In the fluid picture, shears tense fluid elements with an effective tilt of turbulent structures as a consequence. Since the shear tenses of the fluid element can be quantified by the Reynolds stress (R), a dependency between the tilt angle and R is expected (sec. 2.6.2). A study of the Reynolds stress poloidal profile with respect to different properties of the magnetic field configuration (normal/geodesic curvature, (integrated) local magnetic shear) has already been done in [59] for unbiased helium discharges. Furthermore, a qualitative comparison of R with the 2D velocity distributions can be found in [59], too. As a further completion of Reynolds stress picture as a tilt of turbulent eddies, the differently evaluated tilt angles (cross-phase and angle of incident) are compared with R. Whereas R is calculated from the temporally fluctuating velocity components ($R = \langle \tilde{v}_r \tilde{v}_\theta \rangle_T$, sec. 3.1.3), similar to [51], the cross phase calculation (α) is carried out $R = h_{\tilde{v}_r,\tilde{v}_\theta} \cos(\alpha_{\tilde{v}_r,\tilde{v}_\theta})$ (sec. 4.3.1). The poloidal profile of R *(upper-left)* is shown in fig. 6.1 for the case without background flow shear ($\Omega \approx 0$). Both have an asymmetric shape with local maxima at $\theta \approx -0.6\pi$, $\theta \approx 0.4\pi$. The R profile shows higher positive values

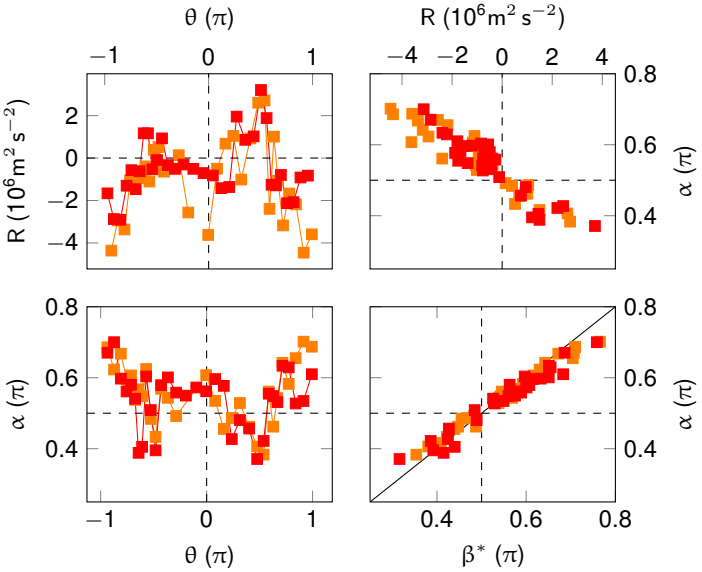

Figure 6.1: *(Upper-left)* Poloidal profile of R. *(Upper-right)* Comparison of R with the average cross-phase. *(Lower-left)* The poloidal profile of the average cross-phase. *(Lower-right)* The poloidal profile of the average cross-phase α and the angle of incident β. The relation $\alpha = \beta^* = -2\beta + \pi/2$ is confirmed by a correlation coefficient of $R_C = 0.98$.

in the range $0 \lessapprox \theta \lessapprox 0.5\pi$ compared to the same region for negative θ as discussed in [59]. The cross-phase (fig. 6.1-*lower-left*) reveals a reversed behavior to R. As a consequence, the comparison of both (fig. 6.1-*(upper-right)*) shows a negative, linear relation between the cross-phase and R. This is in accordance with $R \propto \cos(\alpha)$. The good agreement further suggests that the cross-phase gives the dominant contribution to R in negative correlation.

Furthermore, the tilt of the eddies is correlated to the angle of incident ($\beta = \left\langle \arctan\left[\tilde{v}_r \tilde{v}_\theta^{-1}\right]\right\rangle_T$). A heuristic consideration (sec. 2.6.2.1) relates both angles as $\alpha = \beta^* = -2\beta + \pi/2$. Fig. 6.1-*(lower-right)* shows the average cross-phase versus the modified angle of incident (β^*). The strong linear dependency confirms the proposed relation between the angles with a correlation of $R_C = 0.98$.

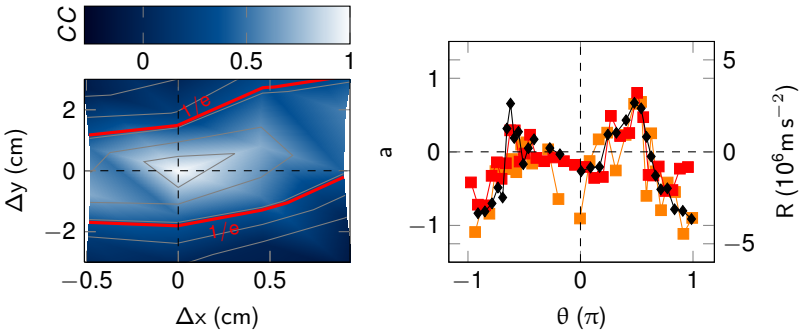

Figure 6.2: (*Left*) The $\tau = 0$ cut of the cross-correlation function in the radial and poloidal shift domain shows a sector of the tilted ellipse modelled by eq. (6.2). (*Right*) Comparison of the tilt of turbulent potential structures obtained by regression of eq. (6.2) (diamond) and R (square). Both show a qualitatively good agreement, which confirms that R is a measure for the tilt of turbulent structures.

In order to analyze the tilt of the turbulent structures, the cross-correlation-functions are modelled around the maximum as

$$CC(\tau, \Delta x, \Delta y') = \exp\left[\frac{\tau^2}{\tau_c^2} + \frac{\Delta x^2}{l_x^2} + \frac{\Delta y'^2}{l_y^2}\right] \tag{6.1}$$

where the variables $\tau, \Delta x, \Delta y'$ are the time, the radial and the poloidal shift with their correlation lengths τ_c, l_x, l_y, respectively. Together, this describes a tilted ellipsoid and constitutes an extension of the elliptical model (sec. 4.4). Again, the shearing coordinates (sec. 2.5) are introduced as $\Delta y' = \Delta y - \bar{v}_y \tau - V_E' \tau_c \Delta x$. Since in this context only the tilt ($a = V_E' \tau_c$, with τ_c as the mean life-time of the structures) is important, the model is further simplified for the case $\tau = 0$ to

$$CC(\tau = 0, \Delta x, \Delta y) = \exp\left[\frac{\Delta x^2}{l_x^2} + \frac{(\Delta y - a\Delta x)^2}{l_y^2}\right] , \tag{6.2}$$

where a denotes an additional slope between the radial and the poloidal shift. The condition $\tau = 0$ slices the ellipsoid and results in a tilted ellipse in the radial and poloidal domain which is exemplarily shown in fig. 6.2-*left* for one specific reference pin. This slope cannot be explained by the elliptical model as discussed in [111], too. An extension of the elliptical model to an

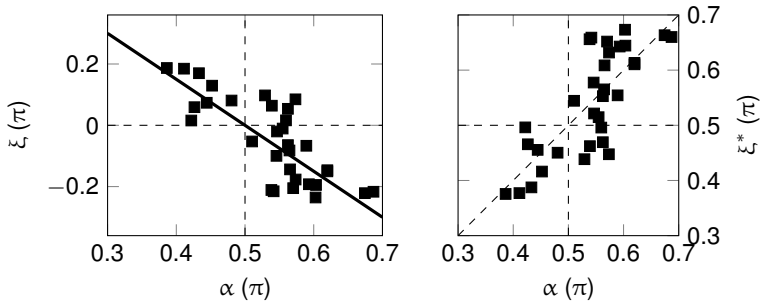

Figure 6.3: (*Left*) The tilt angle calculated from the slope of the $\tau = 0$ cut of the ellipsoidal model plotted against the cross-phase. (*Right*) The same tilt angle adapted by eq. (6.3) plotted against the cross-phase shows a correlation of $R_C = 0.77$

ellipsoidal one as well as the implementation of the shearing coordinates are necessary for future investigations. The slope (a) is calculated by regression. Its poloidal profile is shown as black diamonds in fig. 6.2 and for comparison R contributions can be seen as colored squares in the background. The slope of the turbulent structures shows a qualitatively good agreement in the regions the tilt could be calculated.

The slope can be expressed as a tilt angle by taking the arcus-tangens $\xi = \arctan(a)$. Note, this tilt angle is not necessarily equivalent to the tilt of the main ellipse described by the contours of the model. The tilt angle (ξ) is compared with the cross-phase (α) in fig. 6.3-*left*. A linear fit $f(\alpha) = (-1.5 \pm 0.3)\alpha + (2/3 \pm 0.1)\pi$ indicates a relation between the cross-phase and the tilt induced by the slope of the ellipse. The adapted tilt ξ^* calculated by the equation

$$\alpha = \xi^* = -\frac{2}{3}\xi + \frac{\pi}{2} \tag{6.3}$$

is plotted against the cross-phase (fig. 6.3-*right*) where a correlation coefficient of $R_C = 0.77$ is found.

6.2 Influence of the $E \times B$ shear on the Reynolds stress

The influence of the shear on the tilt of turbulent structures and, therefore, on the Reynolds stress is demonstrated locally on different poloidal

positions. The poloidal profile of the Reynolds stress at zero $E\times B$-shearing

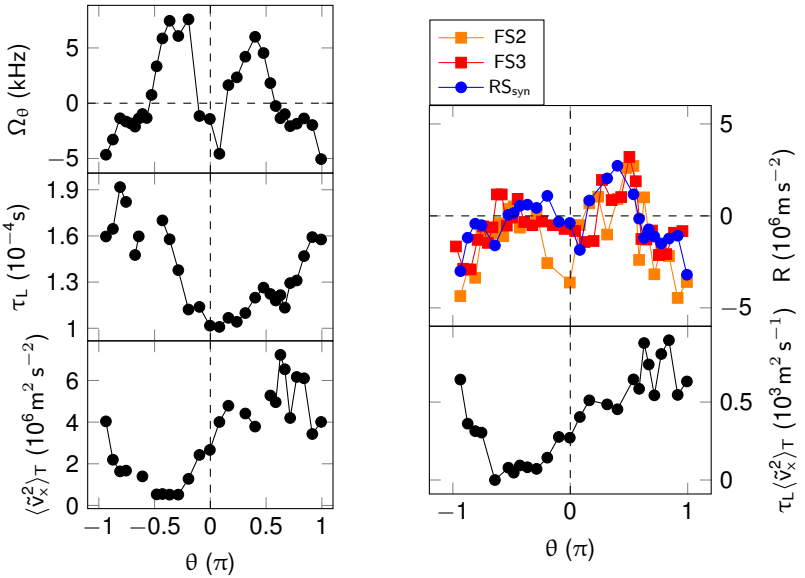

Figure 6.4: (*Left*) The poloidal profiles of the single components of the synthetic R_{syn}: The stationary shearing rate in the *top*, the average life-time (*middle*) and the power in the radial fluctuations (*bottom*). (*Right*) The poloidal profile of the shear induced Reynolds stress ($R_{\mathrm{shear}} = V_E'\tau_L\langle\tilde{v}_x^2\rangle_t$) is shown as circles and the measured Reynolds stress as squares.

rate is compared with the synthetical Reynolds stress described by eq. (2.32) ($R_{\mathrm{syn}} = V_E'\tau_L\langle\tilde{v}_x^2\rangle_t$). The single components of R_{syn} are shown in fig. 6.4-*left*. In the top, the poloidal profile of the background shearing rate is shown. Furthermore, the correlation times have to be determined in order to calculate the time span in which the turbulent structures are exposed to the shear flow, i.e. their mean lifetime ($\tau_L = \tau_g + \tau_d$). This is done by the elliptical model [109, 111] described in sec. 4.4. Whereas the growth time (τ_g) is already obtained from a cross-correlation of negative time shifts (sec. 5.3), the average decay time (τ_d) is calculated from the ones of positive time shifts. The mean life-time is shown in fig. 6.4-*middle-left*. The power of the radial velocity fluctuations ($\langle\tilde{v}_x\rangle_T^2$) is seen at the bottom of fig. 6.4-*left*.

It is not surprising that the poloidal profile of the average life-time has its minimum at $\theta \approx 0.1\pi$ since parts of the life-time can be expressed in terms of the inverse growth rate with its maximum at the same postion (sec. 5.3). In comparison, the poloidal profile of power of the radial fluctuations has a minimum at $\theta \approx -0.4$ shifted to the minimum of the average life-time by $\Delta\theta \approx -0.5\pi$. Whereas the poloidal profile of the stationary $E{\times}B$ shearing rate can be considered symmetric, the contributions of the average life-time and the power of the radial fluctuations are counter-acting each other with respect to the synthetic R_{syn}. A product of both in fig. 6.4-*right-bottom* shows the power of the radial fluctuations as the dominant part.

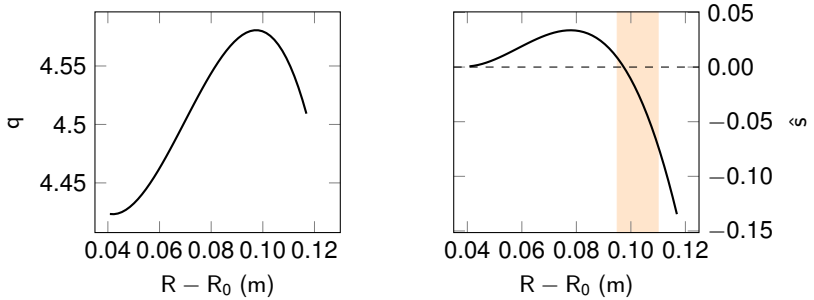

Figure 6.5: *(Left)* The radial profiles of the safety factor ($q = 1/\iota$) and the global magnetic shear ($\hat{s}$). *(Right)* The global magnetic shear calculated from the q-profile as dashed and approximated from the pressure profile as solid line.

Now a synthetic Reynolds stress is calculated from eq. (2.32). The synthetic Reynolds stress is shown in fig. 6.2-*right* as blue circles plotted over the poloidal angle. The data-set for the $\Omega \approx 0$ ($U_{\mathrm{Bias}} = 26\,\mathrm{V}$, #12334) case is taken because the average shearing rate vanishes and it is expected that other influences on the structures' tilt are revealed as for example the magnetic shear [123]. The sets of orange and red squares mark again the poloidal profile of the Reynolds stress calculated from velocity fluctuations for two different flux surfaces. The synthetic and the measured Reynolds stress show a good agreement. The maximum of the synthetic R_{syn} is located at the position of the maximum of the measured R. This results from the power in the radial fluctuations. It influences R profile stronger than the average lift time τ_L does Further, the good agreement between the synthetic and the measured R is

not necessarily expected, since it is suggested that the global magnetic shear ($\hat{s}$) also has a significant influence on R ($R = (-\Delta\theta\hat{s} + V'_E\tau_L)\langle\tilde{v}_x^2\rangle_T$) [123, 124]. Conversely, this means that the influence of the global magnetic shear is rather small even if the average stationary $E\times B$-shearing rate is zero $\Omega \approx 0$, since R is already relatively well represented by the part of the background $E\times B$ shear.

The global magnetic shear $\hat{s}$ can be calculated by the normalized gradient of the safety factor (q) as $\hat{s} = r/q\partial_r q$. Fig. 6.5 shows that the global magnetic shear is low in TJ-K compared to i.e. the shear in the edge of the tokamak Tore Supra ($\hat{s} = 1.4$) [67] and is indeed negligible for the RS study in this work.

6.3 Summary of the Reynolds stress as a tilt of turbulent structures

Turbulent structures are subject to shear stresses resulting in an effective tilt of the structures. Here, three different methods of describing the tilt of the structures are compared with each other and with the Reynolds stress which quantifies the shear stress. The Reynolds stress was calculated from velocity fluctuations obtained from potential fluctuations measured by the array (sec. 3.1.3).

- The comparison between Reynolds stress (R) and the average cross-phase (α)[60, 120, 61] shows a negative correlation as expected from $R \propto \cos(\alpha)$ and suggests that the cross-phase dominantly contributes to the Reynolds stress.

- The average cross-phase can heuristically be expressed by $\alpha = -2\beta + \pi/2$, where $\beta = \left\langle \arctan\left[\tilde{v}_r\tilde{v}_\theta^{-1}\right]\right\rangle_T$ which can be interpreted as angle of incident. The relation is confirmed by a correlation of $R_c = 0.98$

- Space-time cross-correlation functions of the potential fluctuations are modelled by the ellipsoidal model as an extension of the elliptical model by the radial coordinate. The shearing coordinates were implemented resulting in a tilted ellipse in the $\tau = 0$ slice of the ellipsoid in the radial and poloidal shift domain. The tilt of the resulting ellipse is caused by the factor $a\Delta x$ where the slope a depends on the background shear $a = V'_E\tau_L$. The Reynolds stress and the slope correlate qualitatively well. This shows on the one hand that an extension of the elliptical to

the ellipsoidal model is justified, on the other hand that an implementation of the shear coordinates is necessary. A comparison of an angle calculated as $\xi = \arctan(a)$ reveals a linear relation to the cross-phase as $\alpha = -2/3\xi + 0.5\pi$ with a correlation coefficient $R_c = 0.77$.

Tab. 6.1 gives an overview of the relations between the different angles. All

	α	β	ξ
$\alpha =$	α	$-2\beta + \frac{\pi}{2}$	$-\frac{2}{3}\xi + \frac{\pi}{2}$
$\beta =$	$-\frac{1}{2}\alpha + \frac{\pi}{4}$	β	$\frac{1}{3}\xi$
$\xi =$	$-\frac{3}{2}\alpha + \frac{3}{4}\pi$	3β	ξ

Table 6.1: Relations between the cross-phase (α), the angle of incident (β) and the angle calculated from the slope of the ellipsoidal model at $\tau = 0$ (ξ).

three methods agree well with the poloidal profile of the Reynolds stress.

Furthermore, the effect of the shear on Reynolds stress was investigated. A synthetic Reynolds stress was calculated ($R = V'_E \tau_L \langle \tilde{v}_x \rangle$) and was compared with the measured Reynolds stress poloidal profile.

- Besides the symmetric $E\times B$-shearing rate, the power in the radial fluctuations is found to contribute more to the Reynolds stress than the average life-time, resulting in a local maximum of the Reynolds stress at $\theta \approx 0.4\pi$.

- The good agreement between the synthetic and the measured Reynolds stress at even vanishing average shear ($\Omega \approx 0$) implies that the effect of the magnetic shear is negligible in TJ-K.

These results lead to the conclusion that it is indeed the background $E\times B$ shear which tilts and stresses the turbulent structures. The tilt and the Reynolds stress can be seen equivalent to describe the effect of the shear. The ellipsoidal model with implemented shearing coordinates introduces the capability of obtaining the tilt of the structures. As the model is applied in major fusion experiments as ASDEX-Upgrade on data of Doppler-reflectometry [111], radial differences in the tilt may be able to describe the Reynolds stress drive on different poloidal positions.

Chapter 7

Energy transfer into Zonal Flow

The background shear tilts the turbulent structures as found in sec. 6. It is suggested that this has impact first on the poloidally averaged Reynolds stress and second on the production term calculated from the $k-\epsilon$ model describing the energy transfer between zonal flows and other turbulent modes (sec. 2.6.3). In order to test these considerations, first, the dependency of the poloidally averaged Reynolds stress is experimentally examined as well as the dependency of the energy transfer into the zonal flow on the shearing rate (sec. 7.1). Second, the production is compared with the zonal flow power normalized on the total, spectral power in order to analyze the change of the distribution of the power. Finally, the dependence of relative zonal flow power on the background shearing rate is examined. All investigations follow the publication of [36]

7.1 The influence of the shear on the RS and the mean-flow production

The background shear is supposed to change the tilt of the turbulent structures resulting in a non-vanishing RS as previous simulations suggest [123]. The local, time-averaged RS is expected to depend linearly on the $E\times B$-shearing rate

$$R_{\mathrm{loc}}(\theta) = [\, -\Delta\theta_{\mathrm{d}}\,\hat{s} \;+\; \Omega_{\mathrm{loc}}(\theta)\tau_L(\theta)\,]\;\langle\tilde{v}_r^2\rangle_T\;, \tag{7.1}$$

where $\Delta\theta_{\mathrm{d}}$ is the poloidal distance to the ballooning peaking position, $\hat{s}$ the global magnetic shear, Ω_{loc} the local $E\times B$-shearing rate and $\tau_L = \tau_g + \tau_d$ the life-time of the turbulent structures. The global magnetic shear is negligible in TJ-K as the discussion in the previous sec. 6.2 shows. Further, results show that it can be neglected in the case of a symmetric confinement geometry [67].

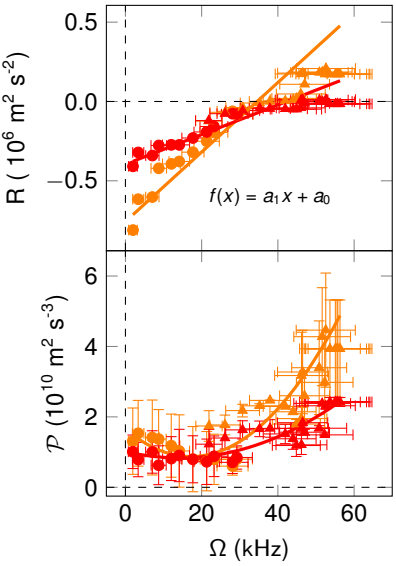

$R(\Omega)$	FS2	FS3
a_1 ($m^2\,s^{-1}$)	22 ± 1	9 ± 1
a_0 (10^5 $m^2\,s^{-2}$)	-7.6 ± 0.3	-4.0 ± 2.7

Figure 7.1: *(Top)* The poloidally and temporally averaged Reynolds stress for two different flux surfaces (orange, inner and red, outer) plotted against the shearing rate. With increasing shearing rate the Reynolds stress increases roughly linearly and has a zero-crossing at around $\Omega \approx 40\,\mathrm{kHz}$. *(Bottom)* The production term calculated according to eq. (2.59) plotted against the shearing rate. Positive values indicate that the energy is transferred from the turbulence into the mean-flow (i.e. zonal flow). For higher shearing rates the energy transfer into the mean-flow takes higher absolute values, too.

$\mathcal{P}(\Omega)$	FS2	FS3
a_2 $m^2\,s^{-1}$	26 ± 7	9 ± 2.5
a_1 (10^5 $m^2\,s^{-2}$)	-9 ± 4	-3 ± 2
a_0 (10^{10} $m^2\,s^{-3}$)	1.6 ± 0.5	1.0 ± 2.4

In the experiment TJ-K, the RS ($\langle \tilde{v}_r \tilde{v}_\theta \rangle$) is poloidally available from the array (see. 3.1.3) [59]. The RS is averaged both temporally and poloidally, as was previously applied in the case of the background shearing rate. The RS of both flux surfaces is plotted against the shearing rate in fig. 7.1-*top*). The figure shows a roughly linear dependence of the RS on the shearing rate, as theoretically expected from eq. (7.1). The fit parameters are shown as inlay and show a slightly different behavior depending on the radial position. The positive correlation between the background shearing rate and the RS confirms the concept of a negative turbulent viscosity $R \approx -\nu_T \Omega + a_0$ with the expected offset at zero shear. Since the life-time, the power in the radial velocity fluctuations and the shearing rate can vary poloidally the life-time or radial velocity fluctuations may weight the shearing rate differently and the RS is not necessarily zero if the mean shearing rate is zero ($R(\Omega = 0) \approx \langle \Omega_{\mathrm{loc}} \tau_L \tilde{v}_r^2 \rangle_T \rangle_\theta \neq 0$).

As defined in sec. 2.6.3, an energy transfer from the turbulence into the mean flow takes place, if the production term is positive. The production term as derived in eq. (2.59) is calculated from the experimental data (sec. 3.1.3)

and is plotted against the shearing rate in fig. 7.1-b). All values are positive, which implies an energy transfer from the turbulence into the poloidal mean flow, as it is expected from the inverse cascade in two-dimensional turbulent systems. The production term depends roughly quadratically on the shear but the coefficients again depend on the radial position. The quadratic behavior is expected from eq. 2.59, where the second term consists of the background RS and the background shearing rate ($R(\partial_x V)^2$). For both dependencies, the RS and the production term, no significant change is found when entering the strong shear regime.

7.2 Redistribution of power

As a consequence of the higher production at higher shear, a redistribution of the energy towards the ZF is expected. For verification, the frequency integrated k-spectrum of the potential fluctuations in fig. 7.2 shows the power distribution for selected shearing rates. Here, the wavenumber is normalized by $\rho_s = \sqrt{m_i T_e}/(eB_0)$, where T_e is obtained from the swept Langmuir probe, and the upper axis respectively shows the poloidal mode number (m). Besides

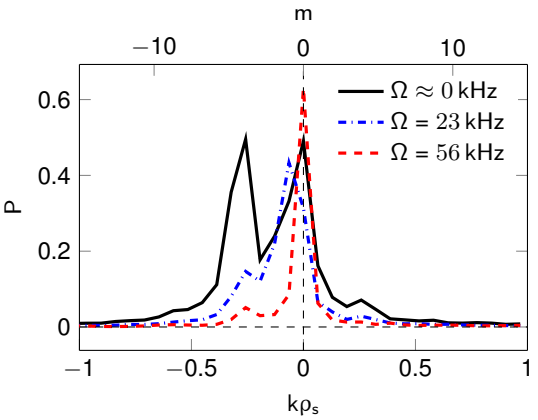

Figure 7.2: Frequency integrated wavenumber power-spectra for different shearing rates. The local maximum at $m = -4$ may be related to the rotational transform ($\iota \approx 0.25$) for TJ-Ks magnetic field. With increasing shear, the $m = 0$ mode gains more power relative to the other modes, i.e. the power is redistributed.

		FS2	FS3	
$P_{ZF,rel}(\mathcal{P})$	a_0	5.76 ± 0.06	-14.41 ± 0.37	$(10^{-12}\ s^3 m^{-2})$
	a_1	0.01 ± 0.02	-0.02 ± 0.04	
$P_{ZF,rel}(\Omega)$	a_0	$(2.7 \pm 6.1)10^{-9}$	$(2.4 \pm 5.2) \cdot 10^{-11}$	(kHz^{-a_1})
	a_1	1.7 ± 0.2	2.1 ± 0.2	
	a_2	0.048 ± 0.004	0.052 ± 0.003	

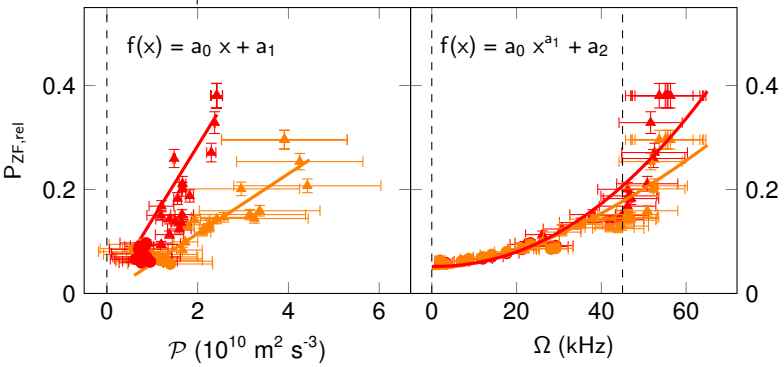

Figure 7.3: *(Left)* The linear dependency between production and relative ZF power, which is the $m = 0$ power normalized on the total power. It describes a redistribution of the power as described by the $k - \epsilon$ model. *(Right)* With increasing shearing rate the relative ZF power increases and reaches its highest level in the strong shear regime. This implies that increasing the background shear leads to an enhanced redistribution of the energy towards the ZF.

the $m = k\rho_s = 0$ mode, which is related to the ZF, an $m = -4$ mode shows up which could be related to the rotational transform ($\iota \approx 0.25$) for TJ-K's magnetic field which could stimulate the $m = -4$ mode as most unstable eigen mode [76] in the system. For the increasing shearing rate, the power in the broadband turbulence decreases. This drop is stronger than the changes in the ZF power. Therefore, this qualitatively describes a redistribution of the spectral power.

In order to quantify the redistribution, the ZF mode is filtered in the frequency-band 3 kHz-8 kHz and integrated. Further the ZF power is normalized to the power of the total kf-spectrum as done in a previous study [51]. This relative ZF power is plotted against the production term in fig. 7.3-a). The roughly linear behavior indicates that indeed an increase in the production takes place simultaneously with an increase of the relative ZF power.

This verifies the power redistribution towards the ZF.

7.3 Summary of the influence of the shearing rate on production and ZF redistribution

The influence of the background $E \times B$-shearing rate on the redistribution of energy is experimentally studied for hydrogen discharges in the stellarator experiment TJ-K under externally controlled shear, which is achieved by electrode biasing. A low shear regime from $\Omega = 0\,\mathrm{kHz} - 45\,\mathrm{kHz}$ and a strong shear regime higher than $\Omega > 45\,\mathrm{kHz}$ are identified.

Following the model, the energy transfer, i.e. the production term, between the poloidal mean flow and the turbulence can be described by the product of the Reynolds stress and the shearing rate. In two-dimensional turbulence, as the one in the stellarator TJ-K, the Reynolds stress is supposed to be positive and to depend linearly on the shearing rate resulting in a quadratic dependency of the production on the flow shear. Both dependencies are confirmed by the experimental data justifying the RS approximation in terms of a negative viscosity. The origin of the offset in the dependency of the Reynolds stress on the shearing rate might be caused by different poloidal weighting of the shearing rate by the life-time or power in the radial fluctuations resulting in non-zero Reynolds stress if the shearing rate is zero.

The redistribution of the energy is qualitatively shown by k-spectra for selected shearing rates. It already indicates a different behavior of the zonal flow component compared to the broadband turbulence, which is reduced in the strong shear regime. For a quantitative study the relative zonal flow power normalized to the total power of the kf-spectrum is analyzed with respect to the production and the shearing rate. A roughly linear dependency of the relative zonal flow power on the energy transfer indicates that indeed the redistribution of the power can be inferred from the production term. The relative zonal flow power increases roughly parabolically with the shearing rate, but shows a trend to higher slopes in the strong shear regime. The increasing shearing rate appears to entail a change in the Reynolds stress and consequently of the production term which describes an energy transfer towards the zonal flow.

The results show that indeed the background shear is able to enhance the energy transfer from the broadband turbulence to the zonal flow. Recent investigations of the I-phase in ASDEX-Upgrade do not reveal any significant

contribution of turbulence driven zonal flows to the mean flow [52, 27]. It must be stressed that the present work focusses on the energetic zonal flow drive rather than damping, which co-determines final zonal flow activity. For high-temperature plasmas as in ASDEX-Upgrade and JFT-2M [125], zonal flows could be subject to, e.g., ion-viscous damping, which is practically absent in TJ-K plasmas because of low ion temperatures [83]. Regardless of the detailed effects of zonal flow damping - which is left for future studies - the present work clearly shows that the power redistribution occurs as a more effective loss channel of turbulence energy when background shear is active.

Chapter 8

Spectral Coupling

In the picture of drift-wave turbulence, a shear is supposed to change the set of possible coupling partners for a specific mode as proposed by Gürcan [35]. Especially an appearing shear should shrink the coupling space of a specific mode. This is tested in this section. Special focus is laid on the three-wave interaction, which is identified experimentally with the help of autobicoherence (see sec. 4.3.3). As will be shown in the first part of this chapter, that the main contributions of the bicoherence follows the dispersion relation of drift waves. Thus the bicoherence is considered to be an appropriate method to analyze the drift waves' nonlinear coupling (sec. 8.1). The second part shows how the manifold shrinks in the presence of an upcoming zonal (shear) flow (sec. 8.2).

8.1 Three-wave interaction of drift-waves

The evolution of ideal drift-wave turbulence, as derived in sec. 2.7.3, is described by the nonlinear term in the Hasegawa-Mima equation [31]

$$\partial_t \hat{\phi}_{\mathbf{k}_3} + i\omega(\mathbf{k}_3)\hat{\phi}_{\mathbf{k}_3} = \frac{1}{2} \sum_{\mathbf{k}_1+\mathbf{k}_2=\mathbf{k}_3} \Lambda_{\mathbf{k}_1,\mathbf{k}_2} \hat{\phi}_{\mathbf{k}_1} \hat{\phi}_{\mathbf{k}_2} \ . \tag{8.1}$$

The dynamically power distribution in the potential is obtained by multiplying eq. (8.1) with $\hat{\phi}_{k_3}(t)$ and an additional ensemble average $\langle\cdot\rangle_E$. The term on the right-hand side results in the bispectrum

$$\partial_t \langle \hat{\phi}_{\mathbf{k}_3} \hat{\phi}^*_{\mathbf{k}_3} \rangle_E + i\omega(\mathbf{k}_3) \langle \hat{\phi}_{\mathbf{k}_3} \hat{\phi}^*_{\mathbf{k}_3} \rangle = \frac{1}{2} \sum_{\mathbf{k}_1+\mathbf{k}_2=\mathbf{k}_3} \Lambda_{\mathbf{k}_1,\mathbf{k}_2} \langle \hat{\phi}_{\mathbf{k}_1} \hat{\phi}_{\mathbf{k}_2} \hat{\phi}^*_{\mathbf{k}_3} \rangle_E \ . \tag{8.2}$$

The single participating waves of the nonlinear interactions have to follow the dispersion relation in wavenumber- and frequency space. As described in

sec. 4.3.3 the autobicoherence, as normalized version of the bispectrum, is able to detect coherent three-wave couplings. In this case it is expanded to a kf-bicoherence-spectrum

$$b^2(k_1, k_2, \omega_1, \omega_2) = \frac{\langle \hat{\phi}(k_1, \omega_1)\ \hat{\phi}(k_2, \omega_2)\hat{\phi}(k_3, \omega_3)\rangle_E}{\langle |\hat{\phi}(k_1, \omega_1)\ \hat{\phi}(k_2, \omega_2)|^2\rangle_E \langle |\hat{\phi}(k_3, \omega_3)|^2\rangle_E} \tag{8.3}$$

by Fourier transformation of the potential fluctuations in frequency space, too. The bicoherence is limited between $0 < b^2 < 1$. A value of one is interpreted as a high coherence of the coupling the coupling components having a fixed phase relation. It is important to note that the bicoherence has to be distinguished from the interaction coefficient Λ_{k_1,k_2} in eq. (8.1) which additionally evaluates the amount of transferred power and further gives information about the coupling direction, i.e about the merging of two modes into one or about splitting one mode into two. The interaction coefficient can theoretically be zero, even if the bicoherence shows a strong coupling.

The expansion to a kf-bicoherence ensures that the resonance conditions are satisfied in both, wavenumber- $(k_1 + k_2 = k_3)$ and frequency-space $(\omega_1 + \omega_2 = \omega_3)$. As mentioned in sec. 2.7.3, both conditions depend on each other because of the dispersion-relation $\omega_i(k_i)$. Besides that, an increased coupling strength in the drift-wave turbulence is expected along with the dispersion relation.

For the stellarator TJ-K, a kf-bicoherence is shown in fig. 8.1-*(left)*. Indeed, values of high bicoherence follow the dispersion relation (line) within its errors (dashed lines) which is Doppler shifted by the stationary $E\times B$-velocity [29, 126]

$$f(k_\theta) = \frac{1}{2\pi}\left[\frac{v_{\mathrm{dia}} k_\theta}{1 + k_\theta^2\rho_s^2 + k_r^2\rho_s^2} + v_{E\times B} k_\theta\right] \tag{8.4}$$

where ρ_s is the drift parameter, v_{dia} the diamagnetic velocity and $v_{E\times B}$ the background flow due to the stationary electric field. These quantities can be deduced to the background parameters n, T_e, ϕ_{pl} obtained by the swept Langmuir probe and emissive probe. The radial wavenumber is estimated from the inverse mean structure size $k_r \approx 100\,\mathrm{m}^{-1}$.

For comparison, the power kf-spectrum is shown in fig. 8.1-*(right)*. Two arrows indicate the directions determined by the $E\times B$-flow and by the electron diamagnetic velocity. The drift-wave structures are generally moving in the electron diamagnetic direction [95, 56, 51] on top of the counter-rotating

background $E\times B$-flow. In the present case (#12334,$U_{\mathrm{Bias}} = 26\,\mathrm{V}, \Omega \approx 0\,\mathrm{kHz}$), the $E\times B$-flow is much higher than the diamagnetic velocity such that the power distribution is asymmetric towards $k < 0$. Moreover, the power distribution is consistent with the dispersion relation (line).

The kf-bicoherence is shown for k_3 in fig. 8.1-*left*. Its wavenumber space is limited for only positive values between $0 < |k_3| < k_{\mathrm{Ny}}$, with k_{Ny} as the Nyquist-wavenumber, due to the domain of the coupling space defined by the bicoherence (cf. sec. 4.3.3). In consequence, the drift directions can not be distinguished in the bicoherence space contrary to the power spectrum. Nevertheless the significant contributions in the bicoherence *exclusively* follow the dispersion relation, whereas the power spectrum follows a comparatively broad distribution.

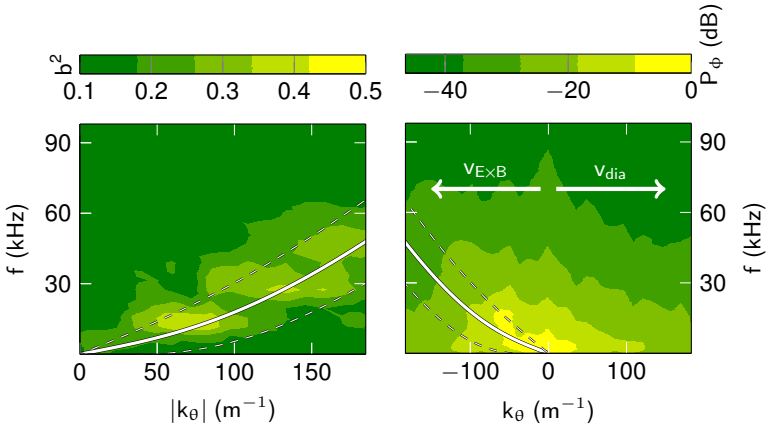

Figure 8.1: *(Left)* kf-bicoherence shows maximum values along the doppler shifted dispersion relation for $|k_3|$ calculated by eq. (8.4) from background parameters obtained from the swept Langmuir and emissive probe with dashed lines as errors. Here, the wavenumber space is purely positive. *(Right)* The usual power kf-spectrum as a comparison. Negative and positive wavenumbers refer to the propagation into$E\times B$- and electron diamagnetic drift direction, respectively.

8.2 Manifold shrinking

The three-wave interaction takes place within a frame given by the resonance conditions and the dispersion relation. This set of possible couplings for one particular wave is called the resonant manifold. From theory (sec. 2.7.3) it is expected that the manifold shrinks under the influence of a shear. This section describes the experimental test which mainly follows the publication [37]. Possible nonlinear interactions between the drift waves are determined by the resonance conditions in wavenumber- and frequency space ($\mathbf{k}_1 + \mathbf{k}_2 = \mathbf{k}_3$ and $\omega(\mathbf{k}_1) + \omega(\mathbf{k}_2) - \omega(\mathbf{k}_3) = \Delta\omega \approx 0$). Thus, for a specific mode, only a distinct coupling space is permitted, the resonant manifold. The theoretical effect of flow shear on the manifold is examined by Gürcan [35]. The implementation of a constant shear v' in x-direction, i.e. a flow in y-direction, leads to a time dependent k_x-component (cf. sec 2.5),

$$k'_{i,x} = k_{i,x} - v'\tau k_{i,y} \quad \text{with} \quad \tau = t + t_0 \ . \tag{8.5}$$

The initial time t_0 can be chosen freely. Equation (8.5) enters the dispersion relation such that the coupling space is reduced with increasing time. Therefore, small-scale turbulent structures are forced to couple with larger structures, especially with the ZF [35]. It is argued that this is the mechanism behind large-scale structure formation in quasi 2D turbulent systems [74], such as atmospheric turbulence or plasma turbulence in toroidal fusion devices. ZFs ($k_y = 0$) hold a special position as they satisfy the resonance condition (2.78) in a trivial way. These mesoscopic turbulent flows are, therefore, always part of the resonance manifold as a persisting component coupling with the drift waves. As being shear flows themselves, this leads to a self-amplification of the ZF and to a suppression of the primary instability. Physically, the mechanism is similar to the straining-out process of eddies, which explains the turbulence suppression by tilting and incorporation, rather than to a breakup, of the vortices [47, 20]. In addition, when the background shear is controlled externally, e.g. by plasma biasing, ZF drive is enhanced as the time averaged resonant manifold is effectively weakened.

An experimental proof of the change in coupling manifold turns out to be quite challenging since the dispersion relation is subject to statistical scatter. Therefore, the coupling space itself is analyzed by a bicoherence spectrum in wavenumber and frequency space. This method intrinsically represents three-wave interactions which follow the resonance condition (Eq. (2.78)) in accordance with the dispersion relation. Due to the low spatial resolution

in radial direction, only the size of the manifold in k_y is regarded and it is referred to $k_{i,y}$ as k_i, from here on. The (auto) bicoherence applied to the potential fluctuations is calculated as

$$b^2(k_1,k_2,\omega_1,\omega_2,\tau) = \frac{|\langle\hat{\phi}_j(k_1,\omega_1,\tau)\hat{\phi}_j(k_2,\omega_2,\tau)\hat{\phi}_j^*(k_3,\omega_3,\tau)\rangle|^2}{\langle|\hat{\phi}_j(k_1,\omega_1,\tau)\hat{\phi}_j(k_2,\omega_2,\tau)|^2\rangle\langle|\hat{\phi}_j(k_3,\omega_3,\tau)|^2\rangle} \tag{8.6}$$

using a wavelet coefficient $\hat{\phi}_j(\omega,\tau)$ [103], analogously to references [127]. The asterisk denotes the complex conjugate and $\langle\cdot\rangle$ the ensemble average. The triple product of the wavelet coefficients (numerator in Eq. (8.6)) is a measure of the phase coupling between the three components (k_1,ω_1), (k_2,ω_2) and (k_3,ω_3). For statistically independent modes, the sum of the individual phases average out and the bicoherence vanishes. With the normalization to the cross and auto power spectrum (denominator in Eq. (8.6)), the bicoherence is limited to the range $[0,1]$, resulting from the Cauchy-Schwarz inequality.

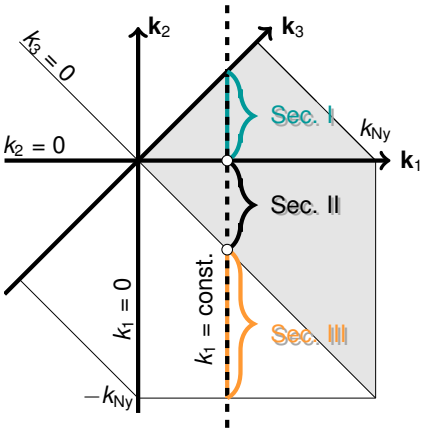

Figure 8.2: Scheme of the bicoherence spectrum in k-space where the projection of the resonance manifold on k_y can be identified (see text for further information). For a specific wavenumber $k_1 = \text{const.}$ the manifold (dashed line) is suspected to shrink in section I (positive wavenumbers) and section III (negative wavenumbers).

The resultant bicoherence spectrum spans in a four-dimensional coupling space $(k_1,k_2,\omega_1,\omega_2)$. The extent of the manifold is in k-space, the spectrum

is averaged over all frequencies the bicoherence being above the significance level, i.e. greater than $1/\sqrt{N}$ [105, 106] which leads to to the reduced bicoherence spectrum $b^2(k_1, k_2, \tau)$. In Fig. 8.2 a common representation of such a spectrum for a single time point is shown schematically. For discrete time traces the domain of definition is restricted to the outlined part. The wavenumbers k_1, k_2, and $k_3 = k_1 + k_2$ are limited to wavenumbers below the Nyquist wavenumber $\pm k_{\mathrm{Ny}}$. The diagonal and counter diagonal are distinguished formally by $k_1 - k_2 = 0$ and $k_1 + k_2 = 0$, respectively. Because of the symmetry to these axes, i.e. $b^2(k_1, k_2) = b^2(k_2, k_1) = b^2(-k_1, -k_2)$ [104], only one quarter of the plane contains independent information (shaded area in Fig. 8.2). For an arbitrarily chosen mode k_1 all corresponding interactions are located on the vertical line $k_1 = \text{const.}$ (dashed line). This is the coupling manifold for the respective mode k_1 in a projection onto the k_y-axis (cf. Fig. 2.10). The points $k_2 = 0$ and $k_3 = 0$ (white dots) mark the interaction with the ZF. Hence, the sections introduced in sec. 2.7.3 can be identified in the bicoherence spectrum. The segment $k_2 > 0$ refers to section I, $0 \geq k_2 \geq -k_1$ to section II, and $k_2 < -k_1$ to section III. Only section I (positive wavenumbers) and III (negative wavenumbers) are of interest for the analysis of the shrinking effect, because only here a statement about the behavior of the manifold can be made. For each section an effective wavenumber k_{eff} is calculated as a measure for the width of the coupling space,

$$k_{\mathrm{eff}} = \sum_{\mathrm{k_2}} w(k_2) \cdot k_2 \quad \text{with} \quad w = \frac{b(k_2)}{\sum_{\mathrm{k_2}} b(k_2)} \quad . \tag{8.7}$$

The weighting factor w accounts for the individual coupling strength each mode exhibits. High and low absolute values of k_{eff} indicate a broad and narrow coupling space, respectively.

To study the temporal evolution of the flow shear a conditional averaging technique is used to create the ensemble average in the calculation of the bicoherence (Eq. (8.7)). The ZF, regarded as poloidal shear flow, is linked to a coherent potential fluctuation on the complete flux surface ($k_\theta = 0$) the experiment directly gives access to. Hence, the zonal potential is used as a trigger signal with the condition $+2\sigma$, triggering on the signal maximum as previously done in studies on related particle [54] and momentum [59] transport. With subwindows of 256 μs, the ensemble average is built from more than 1000 realizations to reflect the averaged dynamics around the ZF event. The temporal evolution of the zonal potential $\langle\phi\rangle_{\mathrm{FS}}$ is shown on the

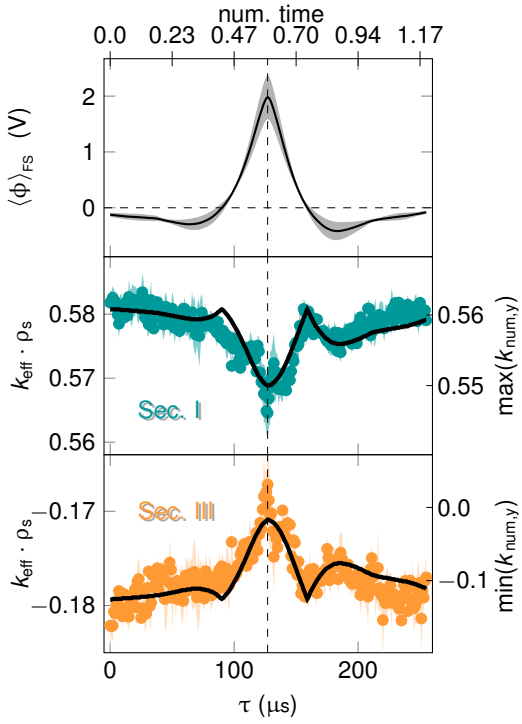

Figure 8.3: Measurement of the effective extent of the resonant manifold during ZF occurrence. *Top:* Conditionally averaged ZF potential with uncertainty (light grey). Its evolution can be regarded equivalent to the radial shear. *Below:* Time evolution of the effective wavenumber k_{eff} in section I (*middle*) and section III (*bottom*) shown as filled dots and uncertainty. Both time traces exhibit a drop of the effective wavenumber when the shear increases. The results are compared to numerical calculations (black solid lines).

top of Fig. 8.3. For the quantification of the size of the coupling manifold, the effective wavenumber is calculated for each time point τ, according to Eq. (8.7). The evolution of $k_{\mathrm{eff}}(\tau)$ for $k_1\rho_s = 0.48$, as an example, is shown in Fig. 8.3 in the two lower plots for both of the meaningful sections for an unbiased case (#10968). When the ZF advances, and thus the shear increases, the effective wavenumber in section I decreases. Vice versa, the effective wavenumber in section III increases, thus the manifold shrinks. The minimum extent is reached when the zonal potential is maximal ($\tau \approx 128\,\mu$s). A possible shift between both is small and hard to identify. This is due to the fact that the overall time duration of the ZF is short and the connected shear is relatively weak, with the same fluctuation amplitude as the ambient turbulence. At falling ZF amplitude the manifold increases again to its

original size. The solid lines in the plots represent the shrinking that would be expected from the manifold shrinking model (Eq. (8.5)), using the time dependent experimental shear as estimated from the zonal potential in Fig. 8.3 (top). The initial wavenumber for the calculation is estimated to $\mathbf{k}\rho_s \approx (0.40, 0.48)$. Both time traces taken together reveal the drop in the size of the manifold, following the dynamics of the ZF. The temporal behavior of the experimentally found effective wavenumbers agree qualitatively well with the model calculations.

8.3 Summary of spectral analyses

Nonlinear, three-wave interaction of drift waves is restricted by the resonance conditions in kf-space coupled by the dispersion relation. A methodological way of detecting the three-wave interaction is the kf-bicoherence. It could be shown that indeed maximum amplitudes of perturbation follow the Doppler shifted drift-wave dispersion relation. In contrast to the usual power kf-spectrum the kf-bicoherence follows more strictly the dispersion relation. This indicates that the bicoherence spectrum is dominated by interactions of drift-waves.

A reduction of the coupling manifold by shear flows has experimentally been observed for the first time. In wave turbulence, wave coupling takes place among modes of a resonant manifold in consequence of the waves' dispersion relation. According to Gürcan [35], this manifold in drift-wave turbulence is predicted to shrink under flow shear. A combined conditional wavelet-based bispectral analysis method in wavenumber and frequency space, applied to multiprobe measurements of the plasma potential in the stellarator experiment TJ-K, has been used to demonstrate that the resonant manifold indeed shrinks in correlation with occurring ZF activity. Physically, this corresponds to the straining-out process of eddies, in which the dynamics evolves in favour of large-scale structures. As a persisting contribution within the shrinking manifold, ZFs gain relative importance in the turbulence's three-wave interactions which may be reflected in enhanced efficiency in turbulence-flow energy transfer. Moreover, the mechanism is not limited to time-varying flow shear but also applies to background shear flows as well, which demonstrates the important role equilibrium shear flows may play in the coupling process between small-scale turbulence and large-scale structures – particularly in the turbulence suppression and in the transport barrier formation scenario in magnetically confined fusion plasmas.

Chapter 9

Conclusion

For the understanding of the physical processes in future nuclear fusion power plants, investigations of the interaction between plasma turbulence and shear flows are indispensable, since shear flows can lead to the reduction of turbulent transport and thus to an increase in the efficiency of the power plants. Based on this motivation, the influence of stationary shear flows as well as time-dependent zonal flows on turbulence was investigated at the stellarator experiment TJ-K. Reynolds' concepts of neutral fluids can be transferred to plasma turbulence.

Because of the low-temperature plasmas in the stellarator TJ-K, invasive diagnostics such as Langmuir probes can be used. Fluctuation measurements with a 128-probe array were related to $E \times B$ flow shear as deduced from potential measurements with an emissive probe. In addition, an electrode was placed in the confinement area of the magnetized plasma and the voltage between the electrode and the vessel was gradually increased. As a result of ambipolar return currents, a new plasma equilibrium was formed. Therefore, in a first analysis the data-set was filtered in a way that only biasing phases with a convex pressure profile and a constant density gradient were taken. Concerning the zonal flow amplification, the biasing phases are further selected where the collisionality was constant.

Poloidal variations of the flow shear in course of the magnetic field inhomogeneity were taken into account at comparisons with local tilts of turbulent structure. For shear scaling studies the shearing rate was externally controlled by plasma biasing. Low and strong shear regimes were distinguished by comparing flow shearing rates with estimates for turbulence growth rates. To this end, an elliptical correlation model was employed for the calculation of the inverse structure lifetimes, which indeed turned out to be comparable with maximum linear drift-waves growth rates. The poloidally averaged shearing rates (Ω) and growth rates (γ) were subsequently compared. For low shearing rates the $\gamma \propto \Omega^{2/3}$ dependence according to the Biglari-Diamond-Terry theorem was confirmed [77]. Furthermore, the weak shear regime up to

a shearing rate of $\Omega \approx 45\,\mathrm{kHz}$ and for higher shearing rates the strong shear regime could be identified.

On the basis of this shearing rate classification the influence of the background shear on the turbulence was examined. In the picture of the vortices in neutral fluids, turbulent eddy structures in the plasma motion are exposed to shear stresses which lead to their tilting. Velocity components for the Reynolds stress were calculated as $E \times B$ drifts from fluctuations in the electrostatic potential, which in a plasma takes over the role of the stream function as in neutral fluids. Poloidal profiles of the structure tilt and Reynolds stress were obtained from potential data measured with a poloidal Reynolds stress array. The tilt of the vortex structures can be determined in three different ways; firstly, the cross-phase between radial and poloidal velocities, secondly, the angle of incident of the two velocity components, and thirdly, the actual tilt of the structures represented by the ellipsoidal shape of the cross-correlations in two-dimensional space and time coordinates. It was found that the Reynolds stress is represented by the averaged cross phase rather than by the cross amplitude. Furthermore, heuristically a relationship between cross-phase and angle of incident was derived and confirmed. Furthermore, a relationship between cross-phase and the tilt of the ellipsoid was experimentally determined, so that all three tilt angles can be converted into each other.

The measured Reynolds stress turns out to be well represented by amplitude estimates relating the Reynolds stress to shearing rate, structures lifetimes and power in radial velocity fluctuations [123]. Moreover, the Reynolds stress was found to scales linearly with the shearing rate. These analyses confirmed the first hypothesis:

- The tilt of turbulent structures can be quantified by the Reynolds stress. The background shear tilts turbulent vortex structures, which results in a linear dependency between shearing rate and Reynolds stress.

In the next step, the influence of the background shear flow on the formation of turbulence-generated zonal flows was analyzed. The Reynolds stress depends linearly on the shearing rate. In consequence, the energy transfer between zonal flow and turbulence, which is the production term in the $k - \epsilon$ model and composed of the product of Reynolds stress and shearing rate, a quadratic dependence between shearing rate and energy transfer was expected [30] and, in the present work, experimentally confirmed. Positive values of energy transfer indicated a redistribution of energy in favor of zonal flow. The zonal power normalized to the total spectral power indeed showed

that the relative power increases with an increasing shearing rate. In contrast to the behavior of the Reynolds stress and the energy transfer, the relative power experiences a thrust in the range of the strong shear regime. These observations confirm the second hypothesis:

- The linear dependency between Reynolds stress and shearing rate results in a quadratic dependency between the energy-transfer, i.e. the production term, and the shearing rate.

In the picture of turbulence as drift waves, the behavior of the fluctuations under the influence of a time-dependent shear flow was analyzed in the Fourier space. The special focus was on the nonlinear three-wave interactions of the individual Fourier modes with each other. With the help of a $k-f$-bicoherence, it was experimentally shown that the contributions with high coherence follow the drift-wave dispersion relation, i.e. the theoretically predicted relationship between wavenumber and frequency. Resonance conditions in the wavenumber and frequency space limits the set of coupling modes, the so-called resonant manifold. By implementing the shearing coordinates, it was shown that the resonant manifold contracts under shear flow [35]. In this work, time-dependent $k-f$-bicoherence analyses were carried out using wavelet coefficients. The analyses were conditionally triggered to naturally occurring zonal shear flows in the system. It was shown experimentally that the effective wavenumber space contracts in the presence of the shear flow and expands again with decreasing shear. This confirmed the third hypothesis:

- Under the constraints of the resonance conditions in wavenumber frequency space and the dispersion relation, the zonal flow as time-dependent shear initially reduces the set of possible couplings and leads to a contraction of the resonant manifold.

The results in this work show that $E\times B$ background shear flows can serve as trigger for turbulence driven zonal flows via an initially tilting vortices as to initiate their Reynolds stress drive and that shear flows can restrict the coupling space in favour of large scale structures like for example zonal flows.

A subsequent investigation would be e.g. the dependence of the turbulent particle transport on the shearing rate, since the transport would also have to decrease due to the redistribution of the spectral power to the zonal flow. In order to simplify investigations on the stationary $E\times B$ background shear, it might also be useful to coat the probe tip of the emissive probe with lanthanum hexaboride. However, preliminary experiments on the robustness of this coating would be necessary.

On a microscopic level, the effect of flow shear could be interpreted as an opener of a loss channel for turbulent energy, in turn being transferred more efficiently to zonal flows. However, in hot fusion plasmas strong gyro viscous flow damping may prevent the energy from being reasonably stored in zonal flows, but such that L-H-transitions may occur without detectable zonal flow contributions to the poloidal mean flow. Additional quantitative analyses are motivated for future work, which should particularly involve effects leading to zonal flow damping, e.g. geodesic transfer or collisional friction. As zonal flows tap energy from transport associated turbulent scales , shear scaling analyses of turbulent transport components are suggested as another continued work.

Bibliography

[1] International Energy Agency et al. *Word Energy Outlook 2018*. Tech. rep. 2018. URL: https://www.iea.org/reports/world-energy-outlook-2018 (27/08/2020).

[2] European commission (EU). *A Clean Planet for all. A European strategic long-term vision for a prosperous, modern, competitive and climate neutral economy*. Tech. rep. COM(2018) 773 final. 2018. URL: https://eur-lex.europa.eu/legal-content/EN/TXT/PDF/?uri=CELEX:52018DC0773 (27/08/2020).

[3] O'Meara. *China's plan to cut coal and boost green growth*. In: Nature **584**.7822 (2020), S1–S3. DOI: 10.1038/d41586-020-02464-5.

[4] Bundesministerium für Wirtschaft und Energie (BMWi). *Wachstum, Strukturwandel und Beschäftigung - Abschlussbericht*. Tech. rep. 2019. URL: https://www.bmwi.de/Redaktion/DE/Downloads/A/abschlussbericht-kommission-wachstum-strukturwandel-und-beschaeftigung.pdf (27/08/2020).

[5] Grünwald et al. *Regenerative Energieträger zur Sicherung der Grundlast in der Stromversorgung. Endbericht zum Monitoring*. Tech. rep. Arbeitsbericht Nr 147. Büro für Technikfolgen-Abschätzung beim Deutschen Bundestag, 2012. URL: https://www.tab-beim-bundestag.de/de/pdf/publikationen/berichte/TAB-Arbeitsbericht-ab147.pdf (08/10/2020).

[6] van Zalk et al. *The spatial extent of renewable and non-renewable power generation: A review and meta-analysis of power densities and their application in the U.S.* In: Energy Policy **123** (2018), pp. 83–91. DOI: 10.1016/j.enpol.2018.08.023.

[7] Hamacher. *The Possible Role of Nuclear Fusion in the 21st Century*. In: *Plasma Physics*. Ed. by Dinklage et al. Vol. 670. Berlin/Heidelberg: Springer-Verlag, 2005, pp. 461–482. DOI: 10.1007/11360360_18.

[8] Lawson. *Some Criteria for a Power Producing Thermonuclear Reactor*. In: Proceedings of the Physical Society. Section B **70**.1 (1957), pp. 6–10. DOI: 10.1088/0370-1301/70/1/303.

[9] Bosch. *Nuclear Fusion*. In: *Plasma Physics*. Ed. by Dinklage et al. Vol. 670. Berlin/Heidelberg: Springer-Verlag, 2005, pp. 445–460. DOI: 10.1007/11360360_17.

[10] Dinklage et al. *Magnetic configuration effects on the Wendelstein 7-X stellarator*. In: Nature Physics **14**.8 (2018), pp. 855–860. DOI: 10.1038/s41567-018-0141-9.

[11] Stroth. *Transport in Toroidal Plasmas*. In: *Plasma Physics*. Ed. by Dinklage et al. Vol. 670. Berlin/Heidelberg: Springer-Verlag, 2005, pp. 213–267. DOI: 10.1007/11360360_9.

[12] Wagner et al. *Development of an Edge Transport Barrier at the H-Mode Transition of ASDEX*. In: Physical Review Letters **53**.15 (1984), pp. 1453–1456. DOI: 10.1103/PhysRevLett.53.1453.

[13] ASDEX Team. *The H-Mode of ASDEX*. In: Nuclear Fusion **29**.11 (1989), pp. 1959–2040. DOI: 10.1088/0029-5515/29/11/010.

[14] Wagner. *The history of research into improved confinementregimes*. In: The European Physical Journal H **43**.4-5 (2018), pp. 523–549. DOI: 10.1140/epjh/e2016-70064-9.

[15] Wagner et al. *H-mode of W7-AS stellarator*. In: Plasma Physics and Controlled Fusion **36**.7A (1994), A61–A74. DOI: 10.1088/0741-3335/36/7a/006.

[16] Morita et al. *H-mode-like transition and ELM-like bursts in LHD with thick ergodic layer*. In: Nuclear Fusion **47**.8 (2007), pp. 1033–1044. DOI: 10.1088/0029-5515/47/8/038.

[17] Pedrosa et al. *Evidence of long-distance correlation of fluctuations during edge transitions to improved-confinement regimes in the TJ-II stellarator*. In: Physical Review Letters **100**.21 (2008), p. 215003. DOI: 10.1103/PhysRevLett.100.215003.

[18] Estrada et al. *Sheared flows and transition to improved confinement regime in the TJ-II stellarator*. In: Plasma Physics and Controlled Fusion **51**.12 (2009), p. 124015. DOI: 10.1088/0741-3335/51/12/124015.

[19] Conway et al. *Mean and Oscillating Plasma Flows and Turbulence Interactions across the L - H Confinement Transition*. In: Physical Review Letters **106**.6 (2011), p. 065001. DOI: 10.1103/PhysRevLett.106.065001.

[20] Xu et al. *Generation of a Sheared Plasma Rotation by Emission, Propagation, and Absorption of Drift Wave Packets*. In: Physical Review Letters **107**.5 (2011), p. 055003. DOI: 10.1103/PhysRevLett.107.055003.

[21] Manz et al. *Zonal flow triggers the L-H transition in the Experimental Advanced Superconducting Tokamak*. In: Physics of Plasmas **19**.7 (2012), p. 072311. DOI: 10.1063/1.4737612.

[22] L. Schmitz et al. *Role of Zonal Flow Predator-Prey Oscillations in Triggering the Transition to H-Mode Confinement*. In: Physical Review Letters **108**.15 (2012), p. 155002. DOI: 10.1103/PhysRevLett.108.155002.

[23] M. Xu et al. *Frequency-Resolved Nonlinear Turbulent Energy Transfer into Zonal Flows in Strongly Heated L-Mode Plasmas in the HL-2A Tokamak*. In: Physical Review Letters **108**.24 (2012), p. 245001. DOI: 10.1103/PhysRevLett.108.245001.

[24] Tynan et al. *Turbulent-driven low-frequency sheared* E B *flows as the trigger for the H-mode transition*. In: Nuclear Fusion **53**.7 (2013), p. 073053. DOI: 10.1088/0029-5515/53/7/073053.

[25] Yan et al. *Observation of the L - H Confinement Bifurcation Triggered by a Turbulence-Driven Shear Flow in a Tokamak Plasma*. In: Physical Review Letters **112**.12 (2014), p. 125002. DOI: 10.1103/PhysRevLett.112.125002.

[26] Cziegler et al. *Nonlinear transfer in heated L-modes approaching the L–H transition threshold in Alcator C-Mod*. In: Nuclear Fusion **55**.8 (2015), p. 083007. DOI: 10.1088/0029-5515/55/8/083007.

[27] Cavedon et al. *Interplay between turbulence, neoclassical and zonal flows during the transition from low to high confinement mode at ASDEX Upgrade*. In: Nuclear Fusion **57**.1 (2017), p. 014002. DOI: 10.1088/0029-5515/57/1/014002.

[28] Krause et al. *The Torsatron TJ-K, an experiment for the investigation of turbulence in a toroidal low-temperature plasma*. In: Review of Scientific Instruments **73**.10 (2002), pp. 3474–3481. DOI: 10.1063/1.1502012.

[29] Stroth et al. *Study of edge turbulence in dimensionally similar laboratory plasmas*. In: Physics of Plasmas **11**.5 (2004), pp. 2558–2564. DOI: 10.1063/1.1688789.

[30] Pope. *Turbulent flows*. Cambridge ; New York: Cambridge University Press, 2000.

[31] Hasegawa et al. *Pseudo-three-dimensional turbulence in magnetized nonuniform plasma*. In: Physics of Fluids **21**.1 (1978), p. 87. DOI: 10.1063/1.862083.

[32] Hasegawa et al. *Nonlinear behavior and turbulence spectra of drift waves and Rossby waves*. In: Physics of Fluids **22**.11 (1979), p. 2122. DOI: 10.1063/1.862504.

[33] Hasegawa et al. *Plasma Edge Turbulence*. In: Physical Review Letters **50**.9 (1983), pp. 682–686. DOI: 10.1103/PhysRevLett.50.682.

[34] Horton. *Turbulent transport in magnetized plasmas*. Singapore ; Hackensack, N.J: World Scientific, 2012. URL: https://doi.org/10.1142/8362 (08/10/2020).

[35] Gürcan. *Effect of Sheared Flow on the Growth Rate and Turbulence Decorrelation*. In: Physical Review Letters **109**.15 (2012), p. 155006. DOI: 10.1103/PhysRevLett.109.155006.

[36] Ullmann et al. *Turbulent energy transfer into zonal flows from the weak to the strong flow shear regime in the stellarator TJ-K*. In: Physics of Plasmas **(submitted)** (2021).

[37] Ullmann et al. *Experimental observation of resonance manifold shrinking under zonal flow shear*. In: Physical Review E **102**.6 (2020), p. 063201. DOI: 10.1103/PhysRevE.102.063201.

[38] D'haeseleer et al. *Flux Coordinates and Magnetic Field Structure*. Berlin, Heidelberg: Springer Berlin Heidelberg, 1991. DOI: 10.1007/978-3-642-75595-8.

[39] Francis F. Chen. *Introduction to Plasma Physics and Controlled Fusion*. Cham: Springer International Publishing, 2016. DOI: 10.1007/978-3-319-22309-4.

[40] Piel. *Plasma Physics*. Graduate Texts in Physics. Cham: Springer International Publishing, 2017. DOI: 10.1007/978-3-319-63427-2.

[41] Stroth. *Plasmaphysik*. Berlin, Heidelberg: Springer Berlin Heidelberg, 2018. DOI: 10.1007/978-3-662-55236-0.

[42] Frisch. *Turbulence: The Legacy of A.N. Kolmogorov*. First. Cambridge University Press, 1995. DOI: 10.1017/CBO9781139170666.

[43] Kolmogorov. *The local structure of turbulence in incompressible viscous fluid for very large Reynolds numbers*. In: Proceedings of the Royal Society of London. Series A: Mathematical and Physical Sciences **434**.1890 (1991), pp. 9–13. DOI: 10.1098/rspa.1991.0075.

[44] Kraichnan. *Inertial Ranges in Two-Dimensional Turbulence*. In: Physics of Fluids **10**.7 (1967), p. 1417. DOI: 10.1063/1.1762301.

[45] Manz et al. *Experimental estimation of the dual cascade in two-dimensional drift-wave turbulence*. In: Plasma Physics and Controlled Fusion **51**.3 (2009), p. 035008. DOI: 10.1088/0741-3335/51/3/035008.

[46] Ramisch et al. *Non-linear dynamics and plasma flows in a basic toroidal plasma experiment*. In: Plasma Physics and Controlled Fusion **52**.12 (2010), p. 124015. DOI: 10.1088/0741-3335/52/12/124015.

[47] Manz et al. *Physical Mechanism behind Zonal-Flow Generation in Drift-Wave Turbulence*. In: Physical Review Letters **103**.16 (2009), p. 165004. DOI: 10.1103/PhysRevLett.103.165004.

[48] Diamond et al. *Zonal flows in plasma—a review*. In: Plasma Physics and Controlled Fusion **47**.5 (2005), R35–R161. DOI: 10.1088/0741-3335/47/5/R01.

[49] Gürcan et al. *Zonal flows and pattern formation*. In: Journal of Physics A: Mathematical and Theoretical **48**.29 (2015), p. 293001. DOI: 10.1088/1751-8113/48/29/293001.

[50] Tynan et al. *Observation of turbulent-driven shear flow in a cylindrical laboratory plasma device*. In: Plasma Physics and Controlled Fusion **48**.4 (2006), S51–S73. DOI: 10.1088/0741-3335/48/4/S05.

[51] Schmid et al. *Collisional Scaling of the Energy Transfer in Drift-Wave Zonal Flow Turbulence*. In: Physical Review Letters **118**.5 (2017), p. 55001. DOI: 10.1103/PhysRevLett.118.055001.

[52] Birkenmeier et al. *Magnetic structure and frequency scaling of limit-cycle oscillations close to L- to H-mode transitions*. In: Nuclear Fusion **56**.8 (2016), p. 086009. DOI: 10.1088/0029-5515/56/8/086009.

[53] Volterra. *Fluctuations in the Abundance of a Species considered Mathematically*. In: Nature **118**.2972 (1926), pp. 558–560. DOI: 10.1038/118558a0.

[54] Birkenmeier et al. *Experimental Evidence of Turbulent Transport Regulation by Zonal Flows*. In: Physical Review Letters **110**.14 (2013), p. 145004. DOI: 10.1103/PhysRevLett.110.145004.

[55] Scott. *Energetics of the interaction between electromagnetic ExB turbulence and zonal flows*. In: New Journal of Physics **7** (2005), pp. 92–92. DOI: 10.1088/1367-2630/7/1/092.

[56] Birkenmeier. *Experimentelle Untersuchungen zur Struktur und Dynamik von Driftwellenturbulenz in Stellaratorgeometrie*. 2012. DOI: 10.18419/opus-1994.

[57] Garland. *Investigation into the infuence of magnetic field structure on the dynamical and spatial properties of plasma edge turbulence in the stellarator TJ-K*. PhD Thesis. Universität Stuttgart, 2019. URL: http://elib.uni-stuttgart.de/handle/11682/10565 (31/08/2020).

[58] Schmid. *Experimental study of the zonal-flow dynamics in the magnetised plasmas of the stellarator experiment TJ-K*. PhD thesis. Universität Stuttgart, 2019.

[59] Schmid et al. *Spatio-temporal structure of turbulent Reynolds stress zonal flow drive in 3D magnetic configuration*. In: New Journal of Physics **19**.5 (2017), p. 055003. DOI: 10.1088/1367-2630/aa67af.

[60] Carreras et al. *Fluctuation-induced flux at the plasma edge in toroidal devices*. In: Physics of Plasmas **3**.7 (1996), pp. 2664–2672. DOI: 10.1063/1.871523.

[61] Diamond et al. *Theory of mean poloidal flow generation by turbulence*. In: Physics of Fluids B: Plasma Physics **3**.7 (1991), pp. 1626–1633. DOI: 10.1063/1.859681.

[62] You et al. *A dynamic global-coefficient subgrid-scale eddy-viscosity model for large-eddy simulation in complex geometries*. In: Physics of Fluids **19**.6 (2007), p. 065110. DOI: 10.1063/1.2739419.

[63] Kraichnan. *Eddy Viscosity in Two and Three Dimensions*. In: Journal of the Atmospheric Sciences **33**.8 (1976), pp. 1521–1536. DOI: 10.1175/1520-0469(1976)033<1521:EVITAT>2.0.CO;2.

[64] Gama et al. *Negative Isotropic Eddy Viscosity: A Common Phenomenon in two Dimensions*. In: *Navier—Stokes Equations and Related Nonlinear Problems*. Ed. by A. Sequeira. Boston, MA: Springer US, 1995, pp. 351–355. DOI: 10.1007/978-1-4899-1415-6_28.

[65] Cao. *Solution of Exercise 5.20*. In: *Turbulent flows*. Pope, 2003. URL: https://pope.mae.cornell.edu/TurbulentFlows/solutions/solutions/chapter5/5.20.pdf (09/04/2020).

[66] Schmitz. *The role of turbulence–flow interactions in L- to H-mode transition dynamics: recent progress*. In: Nuclear Fusion **57**.2 (2017), p. 025003. DOI: 10.1088/1741-4326/57/2/025003.

[67] Manz et al. *Magnetic configuration effects on the Reynolds stress in the plasma edge*. In: Physics of Plasmas **25**.7 (2018), p. 072508. DOI: 10.1063/1.5037511.

[68] Adrian et al. *Analysis and interpretation of instantaneous turbulent velocity fields*. In: Experiments in Fluids **29**.3 (2000), pp. 275–290. DOI: 10.1007/s003489900087.

[69] Chen. *Resistive Overstabilities and Anomalous "Diffusion"*. In: Physics of Fluids **8**.5 (1965), p. 912. DOI: 10.1063/1.1761335.

[70] Pécseli. *Waves and Oscillations in Plasmas*. Second. Boca Raton: CRC Press, 2020. DOI: 10.1201/9780429489976.

[71] Krommes. *Fundamental statistical descriptions of plasma turbulence in magnetic fields*. In: Physics Reports **360**.1-4 (2002), pp. 1–352. DOI: 10.1016/S0370-1573(01)00066-7.

[72] Horton et al. *Quasi-two-dimensional dynamics of plasmas and fluids*. In: Chaos: An Interdisciplinary Journal of Nonlinear Science **4**.2 (1994), pp. 227–251. DOI: 10.1063/1.166049.

[73] Goldreich et al. *II. Spiral Arms as Sheared Gravitational Instabilities*. In: Monthly Notices of the Royal Astronomical Society **130**.2 (1965), pp. 125–158. DOI: 10.1093/mnras/130.2.125.

[74] Balk et al. *Nonlocal turbulence of drift waves*. In: Journal of Experimental and Theoretical Physics **71**.2 (1990), p. 446. DOI: http://jetp.ac.ru/cgi-bin/e/index/e/71/2/p249?a=list.

[75] Burrell. *Effects of EB velocity shear and magnetic shear on turbulence and transport in magnetic confinement devices*. In: Physics of Plasmas **4**.5 (1997), pp. 1499–1518. DOI: 10.1063/1.872367.

[76] Nasim et al. *Geometrical effects on drift wave stability in low shear stellarator plasmas*. In: Plasma Physics and Controlled Fusion **46**.1 (2004), pp. 193–209. DOI: 10.1088/0741-3335/46/1/012.

[77] Biglari et al. *Influence of sheared poloidal rotation on edge turbulence*. In: Physics of Fluids B: Plasma Physics **2**.1 (1990), pp. 1–4. DOI: 10.1063/1.859529.

[78] CIEMAT. *History of TJ-IU torsatron*. 2018. URL: http://www.fusion.ciemat.es/tj-ii-2/tj-ii-previous-history/ (11/09/2020).

[79] CIEMAT. *TJ-II*. 2009. URL: http://fusionwiki.ciemat.es/wiki/TJ-II (09/11/2020).

[80] Enge. *Untersuchung der Ionendynamik in Laborplasmen : am Beispiel von Flips und TJ-K*. PhD Thesis. Universität Stuttgart, 2010. URL: http://elib.uni-stuttgart.de/handle/11682/1912 (07/09/2020).

[81] Wörl. *Untersuchung von Plasmaströmungen in toroidaler Geometrie mittels laserinduzierter Fluoreszenz*. Diploma Thesis. Universität Stuttgart, 2012.

[82] Köhn et al. *Generation and heating of toroidally confined overdense plasmas with 2.45 GHz microwaves*. In: Plasma Physics and Controlled Fusion **52**.3 (2010), p. 035003. DOI: 10.1088/0741-3335/52/3/035003.

[83] Enge et al. *Observation of Anomalous Ion Heating by Broadband Drift-Wave Turbulence*. In: Physical Review Letters **105**.17 (2010), p. 175004. DOI: 10.1103/PhysRevLett.105.175004.

[84] Mahdizadeh et al. *Comparison of Langmuir and emissive probes as diagnostics for turbulence studies in the low-temperature plasma of the torsatron TJ-K*. In: Plasma Physics and Controlled Fusion **47**.4 (2005), pp. 569–579. DOI: 10.1088/0741-3335/47/4/001.

[85] Sichardt. *Electron cyclotron emission investigations at the stellarator TJ-K*. PhD Thesis. Universität Stuttgart, 2020. URL: http://elib.uni-stuttgart.de/handle/11682/10902 (28/07/2020).

[86] Fuchert et al. *The influence of plasma edge dynamics on blob properties in the stellarator TJ-K*. In: Plasma Physics and Controlled Fusion **55**.12 (2013), p. 125002. DOI: 10.1088/0741-3335/55/12/125002.

[87] Garland et al. *The structure and poloidal dynamics of blob filaments in TJ-K*. In: Plasma Physics and Controlled Fusion **58**.4 (2016), p. 044012. DOI: 10.1088/0741-3335/58/4/044012.

[88] Rahbarnia et al. *Experimental study of the electromagnetic component of drift-wave turbulence*. In: Plasma Physics and Controlled Fusion **50**.8 (2008), p. 085008. DOI: 10.1088/0741-3335/50/8/085008.

[89] Mahdizadeh et al. *Investigation of the parallel dynamics of drift-wave turbulence in toroidal plasmas*. In: Plasma Physics and Controlled Fusion **49**.7 (2007), pp. 1005–1017. DOI: 10.1088/0741-3335/49/7/005.

[90] Ramisch et al. *Investigation of the perpendicular dynamics of drift-wave turbulence in a toroidal plasma with multi-probe arrays*. In: Plasma Sources Science and Technology **17**.2 (2008), p. 024007. DOI: 10.1088/0963-0252/17/2/024007.

[91] Hutchinson. *Principles of Plasma Diagnostics*. Second. Cambridge University Press, 2002. DOI: 10.1017/CBO9780511613630.

[92] Köhn. *Investigation of microwave heating scenarios in the magnetically confined low-temperature plasma of the stellarator TJ-K*. PhD Thesis. Universität Stuttgart, 2010. URL: http://elib.uni-stuttgart.de/handle/11682/1906 (24/06/2020).

[93] Sheehan et al. *Emissive probes*. In: Plasma Sources Science and Technology **20**.6 (2011), p. 063001. DOI: 10.1088/0963-0252/20/6/063001.

[94] Manz. *Strukturentstehung in Driftwellenturbulenz toroidaler Plasmen*. PhD Thesis. Universität Stuttgart, 2010. DOI: 10.18419/opus-1854.

[95] Ramisch et al. *Observation of large-scale coherent structures under strong* E B *shear in the torsatron TJ-K*. In: Plasma Physics and Controlled Fusion **49**.6 (2007), pp. 777–789. DOI: 10.1088/0741-3335/49/6/006.

[96] Weynant et al. *H-mode behavior induced by edge polarization in TEXTOR*. In: 17th EPS Conference on Controlled Fusion and Plasma Heating **14**.B (1990), p. 287.

[97] Ullmann. *Untersuchung zur Abhängigkeit zonaler Strömungen von Hintergrundplasmaströmungen*. Examensarbeit. Universität Stuttgart, 2015.

[98] Stöber. *Aufbau eines Mikrowellen-Interferometers für das Torsatron TJ-K*. Diploma Thesis. Christian-Albrechts-Universität Kiel, 2001.

[99] Teliban et al. *Improved conditional averaging technique for plasma fluctuation diagnostics*. In: Plasma Physics and Controlled Fusion **49**.4 (2007), pp. 485–497. DOI: 10.1088/0741-3335/49/4/011.

[100] Happel. *Influence of limiters on plasma equilibrium and dynamics in the torsatron TJ-K*. Diploma Thesis. Christian-Albrechts-Universität Kiel, 2005.

[101] Hinich et al. *The application of the discrete Fourier transform in the estimation of power spectra, coherence, and bispectra of geophysical data*. In: Reviews of Geophysics **6**.3 (1968), p. 347. DOI: 10.1029/RG006i003p00347.

[102] Gavin. *Random Processes, Correlation,Power Spectral Density, Threshold Exceedance*. 2019. URL: http://people.duke.edu/~hpgavin/cee541/RandomVibration.pdf (08/10/2020).

[103] Torrence et al. *A Practical Guide to Wavelet Analysis*. In: Bulletin of the American Meteorological Society **79**.1 (1998), pp. 61–78. DOI: 10.1175/1520-0477(1998)079<0061:APGTWA>2.0.CO;2.

[104] Kim et al. *Digital Bispectral Analysis and Its Applications to Nonlinear Wave Interactions*. In: IEEE Transactions on Plasma Science **7**.2 (1979), pp. 120–131. DOI: 10.1109/TPS.1979.4317207.

[105] Haubrich. *Earth noise, 5 to 500 millicycles per second: 1. Spectral stationarity, normality, and nonlinearity*. In: Journal of Geophysical Research **70**.6 (1965), pp. 1415–1427. DOI: 10.1029/JZ070i006p01415.

[106] Ge. *Significance testing for wavelet bicoherence and its application in analyzing nonlinearity in turbulent shear flows*. In: Physical Review E **81**.5 (2010), p. 56311. DOI: 10.1103/PhysRevE.81.056311.

[107] Taylor. *The Spectrum of Turbulence*. In: Proceedings of the Royal Society A: Mathematical, Physical and Engineering Sciences **164**.919 (1938), pp. 476–490. DOI: 10.1098/rspa.1938.0032.

[108] Briggs et al. *The Analysis of Observations on Spaced Receivers of the Fading of Radio Signals*. In: Proceedings of the Physical Society. Section B **63**.2 (1950), pp. 106–121. DOI: 10.1088/0370-1301/63/2/305.

[109] Zhao et al. *Space-time correlations of fluctuating velocities in turbulent shear flows*. In: Physical Review E **79**.4 (2009). DOI: 10.1103/PhysRevE.79.046316.

[110] Prisiazhniuk et al. *Magnetic field pitch angle and perpendicular velocity measurements from multi-point time-delay estimation of poloidal correlation reflectometry*. In: Plasma Physics and Controlled Fusion **59**.2 (2017), p. 025013. DOI: 10.1088/1361-6587/59/2/025013.

[111] Pinzón et al. *Measurement of the tilt angle of turbulent structures in magnetically confined plasmas using Doppler reflectometry*. In: Plasma Physics and Controlled Fusion **61**.10 (2019), p. 105009. DOI: 10.1088/1361-6587/ab394d.

[112] Birkenmeier. *Experiments and Modeling of Transport Processes in Toroidal Plasmas*. Diploma Thesis. Stuttgart: Universität Stuttgart, 2008.

[113] Lechte et al. *Plasma parameter limits of magnetically confined low temperature plasmas from a combined particle and power balance*. In: Physics of Plasmas **9**.6 (2002), pp. 2839–2846. DOI: 10.1063/1.1467928.

[114] Garland et al. *The influence of magnetic field curvature on intermittency in drift-wave turbulence in the stellarator TJ-K*. In: Physics of Plasmas **27**.5 (2020), p. 052304. DOI: 10.1063/5.0004963.

[115] Dewhurst et al. *The effects of nonuniform magnetic field strength on density flux and test particle transport in drift wave turbulence*. In: Physics of Plasmas **16**.7 (2009), p. 072306. DOI: 10.1063/1.3177382.

[116] Wakatani et al. *A collisional drift wave description of plasma edge turbulence*. In: Physics of Fluids **27**.3 (1984), p. 611. DOI: 10.1063/1.864660.

[117] Ramisch. *Linear Growth rate calculation with the MCC code*. 2011.

[118] Nijenhuis et al. *Non-Newtonian Flows*. In: *Springer Handbook of Experimental Fluid Mechanics*. Ed. by Cameron Tropea et al. Berlin, Heidelberg: Springer Berlin Heidelberg, 2007, pp. 619–743. DOI: 10.1007/978-3-540-30299-5_9.

[119] Birkenmeier et al. *Experimental Investigation of the Magnetic Configuration Dependence of Turbulent Transport*. In: Physical Review Letters **107**.2 (2011), p. 025001. DOI: 10.1103/PhysRevLett.107.025001.

[120] Ramisch. *Scaling and manipulation of turbulent structures in the torsatron TJ-K*. PhD thesis. Universität Kiel, 2005. URL: https://macau.uni-kiel.de/receive/diss_mods_00001393 (09/02/2020).

[121] Manin et al. *Nonlinear interaction of small-scale Rossby waves with an intense large-scale zonal flow*. In: Physics of Fluids **6**.3 (1994), pp. 1158–1167. DOI: 10.1063/1.868286.

[122] Tropea et al., eds. *Springer handbook of experimental fluid mechanics*. Berlin: Springer, 2007. URL: https://doi.org/10.1007/978-3-540-30299-5.

[123] Fedorczak et al. *Shear-induced Reynolds stress at the edge of L-mode tokamak plasmas*. In: Nuclear Fusion **52**.10 (2012), p. 103013. DOI: 10.1088/0029-5515/52/10/103013.

[124] Fedorczak et al. *Dynamics of tilted eddies in a transversal flow at the edge of tokamak plasmas and the consequences for L–H transition*. In: Plasma Physics and Controlled Fusion **55**.12 (2013), p. 124024. DOI: 10.1088/0741-3335/55/12/124024.

[125] Kobayashi et al. *Spatiotemporal Structures of Edge Limit-Cycle Oscillation before L-to-H Transition in the JFT-2M Tokamak*. In: Physical Review Letters **111**.3 (2013), p. 035002. DOI: 10.1103/PhysRevLett.111.035002.

[126] Yu et al. *Comparison of the density fluctuation spectrum and amplitude in TEXT with expectations for electron drift waves*. In: Physics of Fluids B: Plasma Physics **4**.2 (1992), pp. 381–385. DOI: 10.1063/1.860287.

[127] van Milligen et al. *Wavelet bicoherence: A new turbulence analysis tool*. In: Physics of Plasmas **2**.8 (1995), pp. 3017–3032. DOI: 10.1063/1.871199.

Danksagung

Ohne die Mithilfe verschiedenster Personen wäre diese Arbeit nicht möglich gewesen. Zunächst ist Herr Prof. Dr. Günter Tovar zu nennen, der dankenswerter Weise die Aufsicht und Führung der Arbeit übernommen hat. Zweitens will ich Dr. Mirko Ramisch danken, unter dessen fachlicher Führung als Leiter der Gruppe Plasmadynamik und Diagnostik, und aufgrund seiner fachlichen Expertise diese Arbeit fruchten konnte. Im gleichen Atemzug sollen Prof. Dr. Peter Manz und Dr. Bernhard Schmid genannt werden die mir genauso geholfen bzw. mich unterwiesen haben, wobei mir Bernhard auch der Durchführung und Entwicklung der Experimente geholfen hat. Bei der Durchführung haben mich zudem Dr. Gabriel Sichardt, Dr. Alf Köhn, Dr. Eberhard Holzhauer sowie der wissbegierige Masterstudent Raphaél Carmona unterstützt. Ohne die freundliche und unkomplizierte Hilfe von Gabriel sowie seiner Expertise in Linux-basierten Systemen wäre ich sicherlich bei einigen digitalen Problemen ratloser gewesen. Als enthusiastischer Wissenschaftler hat Alf mich immer wieder motiviert und hat mir nicht nur bei Konferenzen zur Seite gestanden. Im Labor durfte ich von Eberhards Wissen und seinen Elektronikkenntnissen sehr profitieren. Desweiteren bin ich dem Ingenieur der Arbeitsgruppe, Bernhard Roth, sehr dankbar, ohne den ein Betrieb bzw. Umbau des Experiments nicht hätte stattfinden könnten. Die Auswertung der Daten wäre ohne Serveradministration von Dr. Burkhard Plaum genauso wenig möglich gewesen.

Ebenfalls grundlegend für die Arbeit im Labor war die gute Zusammenarbeit mit der Elektronik-Werkstatt und der Mechanik-Werkstatt, für die ich mich recht herzlich stellvertretend bei den jeweiligen Leitern Herrn Röhlinger bzw. Herrn Rempel bedanken möchte.

Schließlich möchste ich mich bei der Verwaltung des IGVPs, namentlich bei Frau Ingeborg Wagner, Dr. Matthias Walker und Frau Ruth Edelmann-Amrhein, bedanken, durch deren Einsatz ein geordneter Ablauf der Promotion gesichert wurde.

Eidesstattliche Erklärung

Hiermit erkläre ich, dass ich die beigefügte Dissertation selbstständig verfasst und keine anderen als die angegebenen Hilfsmittel genutzt habe. Alle wörtlich oder inhaltlich übernommenen Stellen habe ich als solche gekennzeichnet.

Ich versichere außerdem, dass ich die beigefügte Dissertation nur in diesem und keinem anderen Promotionsverfahren eingereicht habe und dass diesem Promotionsverfahren keine endguültig gescheiterten Promotionsverfahren vorausgegangen sind.

_____ _____

Ort, Datum Unterschrift